DIPLOMARBEIT

Energy Deposition Studies for the Experimental Insertions of FCC-hh

zur Erlangung des akademischen Grades

Diplom-Ingenieur/in

im Rahmen des Studiums

Technische Physik

ausgeführt am Atominstitut
der Fakultät für Physik
der Technischen Universität Wien

unter der Anleitung von
Privatdoz. Dipl.-Ing. Dr.techn **Michael Benedikt**
Dr. **Francesco Cerutti**
Dr. **Maria Ilaria Besana**

durch
Barbara Humann
Matrikelnummer 01325686
Hamerlinggasse 7
2340 Mödling

_____   _____
Unterschrift Verfasser/in   Unterschrift Betreuer/in

Genf, Dezember 2019

Abstract

In order to explore new possibilities for particle physics for the post-LHC era, the Future Circular Collider (FCC) study was launched in 2014 to assess its feasibility. Different machines are considered, including a hadron collider machine, FCC-hh. Similar to LHC, this would be a circular collider with a significantly larger circumference of 100 km and colliding protons at a centre of mass energy of 100 TeV. Proton collisions at such high energies lead to a large amount of collision debris in the experimental insertion regions (EIR) of the accelerator. The collision debris impacts the elements of the accelerator causing long term damages, like deterioration of organic materials and superconductors, as well as instantaneous effects, like quenching of the superconducting magnets.

This thesis studies the impact of the collision debris in the high-luminosity EIR of FCC-hh. For this purpose Monte Carlo simulations have been performed with the FLUKA code. Quantities like linear power distribution, peak power density, integrated dose and displacements per atom are studied for the elements of the EIR for both, horizontal and vertical crossing schemes. Mitigation strategies are developed for decreasing the impact on the magnets. With those mitigation strategies, both the absorbed power and the peak power density, are below the critical values for all the magnets. The displacements per atom benefited as well from the mitigation strategies, but still require further analysis. The cryogenic system could evacuate the deposited power on the cold masses and the magnets are protected against the risk of quenching. The peak power density remains below $8\,\mathrm{mW/cm^3}$, which is reassuring. As for the integrated dose on the insulator, the situation improved significantly but there are still few magnets where the design limit of 30 MGy is exceeded. This rather conservative limit is expected to rise up to 100 MGy with the use of more resistant materials. In this case, the accumulated dose would be acceptable for all the magnets of the EIR, with one exception. Further mitigation measures should be conceived for this magnet.

Kurzfassung

Um neue Möglichkeiten in der Teilchenphysik für die Post-LHC Ära zu erkunden, wurde 2014 die Future Circular Collider (FCC) Studie gestartet. Unterschiedliche Maschinen werden evaluiert, unter anderem ein Proton-Proton Speicherring. Gleich wie beim LHC, handelt es sich hierbei um einen Kreisbeschleuniger, allerdings mit einem signifikant längerem Umfang von 100 km und einer Schwerpunktsenergie von 100 TeV. Protonenkollisionen bei solch hohen Energien führen zu einer großen Mengen Kollisionsdebris in den "experimental insertion regions" (EIR) des Beschleunigers. Dieser Debris beeinflusst die Elemente im Beschleuniger durch Langzeitschäden, wie Abnutzung von organischen Materialien und Supraleitern, aber auch sofortige Effekte, wie dem Zusammenbruch der Supraleitung in Magneten.

Diese Arbeit setzt sich mit dem Einfluss von Kollisionsdebris in den EIR mit hoher Luminosität in FCC-hh auseinander. Für diesen Zweck wurden Monte Carlo Simulationen mit dem Fluka Code durchgeführt. Größen wie lineare Leistungsverteilung, maximale Leistungsdichte, integrierte Dosis und DPA (Displacements per Atom) wurden für beide Kreuzungswinkeloptionen, horizontal und vertikal, untersucht. Optimierungsmaßnahmen um den Einfluss auf die Magnete zu verringern wurden entwickelt. Durch diese Maßnahmen, sind sowohl die absorbierte Leistung als auch die maximale Leistungsdichte unter den kritischen Werten. Die DPA profitiert ebenfalls von der Optimierung, allerdings sind weitere Untersuchungen notwendig. Das Kryogeniksystem ist fähig die Leistung von den supraleitenden Magneten abzutransportieren und diese sind vor Zusammenbruch der Supraleitung gesichert. Die maximale Leistungsdichte bleibt deutlich unter dem Grenzwert von $8\,\mathrm{mW/cm^3}$. Die Situation für die integrierte Dosis auf den Insulatoren hat sich signifikant verbessert, allerdings überschreiten noch immer einige Magnete das Designlimit von 30 MGy. Dieses Limit wurde sehr konservativ gewählt und durch die Verwendung von widerstandsfähigeren Materialien sollte das Designlimit auf 100 MGy anwachsen. In diesem Fall wäre die integrierte Dosis für alle Magnete in der EIR akzeptabel, mit einer Ausnahme. Für diesen Magneten sollten weitere Optimierungsmaßnahmen angedacht werden.

Acknowledgements

At first I want to thank Michael Benedikt, who gave me the possibility to do an internship for a project work at CERN. With my vague request to do some simulations, even though I did not have much experience, he managed to place me in a section where I was very comfortable. Therefore I am really happy that I could stay there for my master thesis as well.

The work in the EN-STI-BMI section would not have been so educational and satisfying without our section leader Francesco Cerutti. No matter what the problem was, either on the technical side or the administrative as well, he would always try to find a solution. Furthermore, I am grateful for getting the opportunity of giving a talk at the FCC Week 2019, which was probably one of the highlights in my time as a technical student.

I could not have been luckier than having Ilaria Besana as my supervisor. The support I have received from her throughout the last year was amazing. From spending hours to sort out problems with certain simulations where there was no documentation to all the support I have received for the thesis, you gave me great guidance.

Furthermore, I want to thank my colleague James Hunt for the help and advises for the thesis. A big hug goes to my dear friend Elli, who spent hours explaining accelerator physics to me and provided me with food when I was too stressed to cook.

Finally, I want to thank my family, who has always supported me, no matter what my plan was. Thanks to my parents, Claudia and Paul, who gave me the confidence to achieve what I have wanted from a young age on. Also thanks a lot to my siblings, Kathrin and Benedikt, who always accepted me as who I am.

Last but not least, thanks to my boyfriend Michi, who was never complaining about me being far away and is truly happy for me. That means a lot to me.

Thank you!

Contents

Contents

Chapter 1

Introduction

1.1 Future Circular Collider Study

The accelerator complex at CERN with all its different accelerators has provided science with numerous discoveries. Many achievements regarding particle physics were accomplished at CERN, from finding the W/Z bosons in the 1980s [1] to discovering the Higgs-Boson at a mass of 125 GeV at CMS [2] and ATLAS [3] experiments at the Large Hadron Collider (LHC). With all these discoveries, the Standard Model has continuously predicted the outcomes.

After finding the Higgs-Boson at LHC, it is important to study its properties in detail. In addition to this, in particle physics there are still many open questions. Starting from the fact that only a small fraction of the universe consists of ordinary matter and dark matter is intrinsically not included in the Standard Model, to the asymmetries between matter and anti-matter [4].

The Future Circular Collider (FCC) study [5] was launched in 2014 with the goal of measuring the Higgs and top quark properties in detail and to extend the search for new physics in the TeV region. The FCC study is an international collaboration between 136 institutes from 34 different countries. In this innovative project research for new fundamental physics is done and new technologies are developed.

The FCC machines are planned to be circular colliders with a circumference of nearly 100 km. This ring would be located next to the current LHC in the basin between the Jura and the Alps (Fig. 1.1.1).

Similarly to the history of LHC, where the Large Electron-Positron Collider (LEP) was installed first in the tunnel, the idea is to install an electron machine, FCC-ee, first and then move to a hadron machine, FCC-hh, after several years of operation [6]. In this thesis the straight insertion regions of FCC-hh are studied, therefore a more detailed look into FCC-hh is given.

1.1.1 FCC-hh

In FCC-hh protons are collided at a nucleon-nucleon centre-of-mass energy of 100 TeV. Similarly to LHC, runs should be performed with heavy ions as well, at a centre-of-mass energy of 39 TeV for Pb-Pb collisions and 63 TeV for Pb-p collisions [7]. This accelerator would use the already existing accelerator structure offered at CERN as pre-accelerators. More specifically, two options are studied to either use an upgraded superconducting SPS or LHC as the final
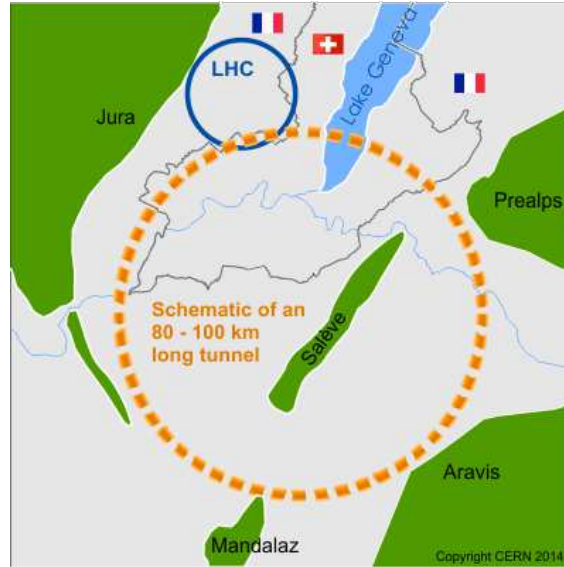
Figure 1.1.1: FCC Layout. (Copyright by CERN 2014)

accelerator before the particles are then injected into the FCC machine. For achieving such high energies it is necessary to increase the magnetic field of the dipoles to 16 T. Furthermore, the ultimate peak luminosity should be increased by a factor of 30 compared to LHC and a factor of 6 compared to HL-LHC [6].

The layout of the machine is comparable with the one of LHC with two main interaction points where the two beams will collide at the maximum instantaneous luminosity (PA, PG) and two lower luminosity interaction regions (PB and PL) (Fig. 1.1.2). The high-luminosity interaction points are located in the middle of 1.4 km long straight sections. Those straight sections are the subject of this thesis.

Figure 1.1.2: FCC-hh Layout. [8]

The significant gain of centre-of-mass energy compared to LHC would greatly increase the reach for new physics. For instance the mass reach would raise by a factor of 5. Similarly, about 10 times more data could be acquired, leading to higher statistics [9]. The production

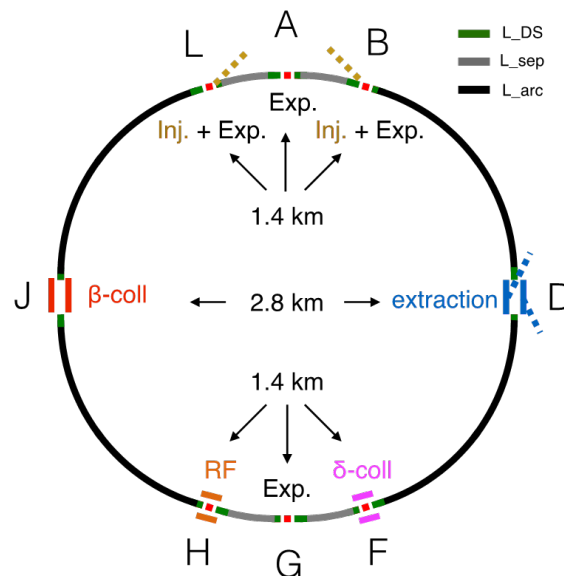|	Unit	LHC	HL-LHC	FCC-hh (nominal)
Centre of mass energy	TeV		14	100
Circumference	km		26.7	97.75
Dipole field	T		8.33	16
Straight sections	m		8x528 m	6x1400 m + 2x2800 m
Number of IPs	-		2+2	2+2
Injection energy	TeV		0.45	3.3
Peak luminosity	$10^{34} \text{cm}^{-2} \text{s}^{-1}$	1.0	5.0	30.0
Inelastic σ_{pp}	mbarn		85	108
L*	m		23	40
Number of bunches	-		2808	10400
Bunch spacing	ns		25	25
Nominal tran. nor. emittance	μm	3.75	2.5	2.2
Beam current	A	0.584	1.12	0.5
IP beta function	m	0.55	0.15	0.3
Full crossing angle	μrad	285	590	200
Stored energy per beam	GJ	0.392	0.694	8.3
Dipole coil aperture	mm		56	50

Table 1.1.1: Machine Parameters [6]: LHC, HL-LHC, FCC-hh. L*: The distance between the IP and the first quadrupole, σ_{pp}: cross-section of a proton-proton collision, Nominal tran. nor. emittance: nominal transversal normalised emittance. The concepts of these quantities are explained in the next chapter.

rates of events that are in the reach of LHC energy are increased by large factors and therefore would enable to reduce the statistical error for many measurements [4].

1.1.2 Other Machines

As mentioned above, three different machines should go in operation in the FCC tunnel. Before starting the operation with FCC-hh, FCC-ee should be installed. In case of a lepton collider, the centre-of-mass energy is mainly limited by synchrotron radiation. Depending on the performed measurements, different beam energies are used, from 45.6 GeV in case of Z boson studies up to 182.5 GeV in case of $t\bar{t}$ measurements. This energy is much lower than in FCC-hh but the collisions are cleaner, since elementary particles are collided and not hadrons, which leads to point-like collisions [10].

With the luminosity achieved in FCC-ee, an increased precision can be reached. This would offer the possibility to measure the properties of the electroweak bosons, W and Z, with an accuracy of the order of one per mille and to understand those on a more profound level. At higher energies, very accurate measurements of Higgs boson and top quark properties could be performed [4].

Additionally, the idea of a lepton-hadron collider machine, FCC-eh, exists. As the name says, in this machine an electron beam at 60 GeV is collided with a proton beam at 50 TeV. This machine would operate as a huge microscope, offering views into the proton substructure. Furthermore it would be possible to understand whether quarks are elementary particles.

Similarly as with FCC-hh, Higgs mechanisms like Higgs self-coupling could be measured. Apart from this, neutrino oscillations and scenarios regarding dark matter can be subject of the experiments of FCC-eh [4].

1.2 Energy Deposition Studies

In this thesis, the energy deposition of collision debris in the high luminosity experiments on the insertion regions of FCC-hh is studied. Energy deposition studies are essential for developing this new high energy hadron accelerator because unprecedented radiation levels are expected at FCC-hh. As discussed in the next chapter, radiation can have a dramatic effect, including accidents, failures and permanent damages. With the help of different simulation tools, several protection scenarios can be tested and developed. These measures protect the machines from possible failures, either in the short-term or over the whole run-time of the FCC-hh machine.

These studies therefore play a key role in the design of the machine in the earliest stages. The goal is to design adequate protection strategies to keep the machine safe.

Chapter 2 presents the key concepts and principles that are essential for understanding the results of the simulations described in this thesis. An overview of accelerator physics with emphasis on the relevant quantities is given. This is followed by a section about beam material interaction, in which the sources and effects of radiation and the underlying physics are discussed. Furthermore, an introduction to Monte Carlo simulations is given. Finally, the used simulation tools will be presented as well as the simulation settings.

In Chapter 3 the geometry and the elements implemented in the simulation are explained.

Chapter 4 focuses on the energy deposition studies for the quadrupole triplet. Furthermore the types of particles responsible for energy deposition in this part of the accelerator are discussed and mitigation strategies are presented. This is followed by the energy deposition studies for the matching section in Chapter 5. Additionally, a special type of simulation, the two-step simulation, is discussed.

Finally, the conclusion of this project is presented in Chapter 6.

Chapter 2

Key Concepts and Principles

In this chapter the key concepts and principles for the simulations are briefly explained. First, there will be a brief introduction to accelerator physics, explaining the properties that are crucial for the simulations. In the first section the basic concepts of accelerator physics are discussed. Afterwards a section about beam material interactions follows, describing the problems that occur if a high energy beam interacts with the elements of the machine. Finally, a section is dedicated to Monte Carlo simulations in general. The used simulation tools also will be discussed.

2.1 Accelerator Physics

The aim of this section is to give a short introduction to accelerator physics. First, the co-ordinate system that is used is described.

This is followed by a section about transverse beam dynamics that explains how the beam moves in a circular accelerator or storage ring. Furthermore, the tasks of different types of magnets that can be found in the accelerator are discussed. This is a crucial ingredient to understanding the challenges that are faced later in the thesis.

Finally, quantities like emittance, beta function and luminosity will be discussed. The emittance and the beta function describe the behaviour of the beam and determine the settings of several elements in the machine. Luminosity is one of the quantities determining the performance of the accelerator.

The theoretical explanations in this chapter are based on diverse references covering the field of accelerator physics ([11], [12]).

2.1.1 Co-ordinate System

For circular accelerators the so-called Frenet-Serret co-ordinate system [12] is used which is shown in Fig. 2.1.1.

Depending on the reference system, either s or z is used as the longitudinal co-ordinate. If the machine itself is investigated and the reference system is at rest, s is used. In this case $s = 0$ is given at a certain point in the accelerator, for example at injection or in this project at an interaction point. From this point s increases along the ring following the reference

particle and it is usually given in metres. While s describes the path of the reference particle, z describes the longitudinal offset of the particles, compared to the reference particle.
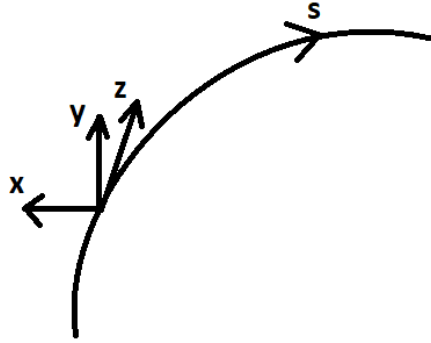

Figure 2.1.1: Frenet-Serret co-ordinate system, used for accelerator physics.

The optimal particle moves around the accelerator in loops, closing the orbit after each loop at $x = 0$ and $y = 0$. The displacement of the beam with respect to the trajectory in the horizontal plane is x and the position in the vertical plane is y. Moving towards the centre of the accelerator in the horizontal plane, x decreases.

2.1.2 Transverse Beam Dynamics

If a charged particle, for example a proton or electron, moves in a field free region, it will move along a straight line. If a charged particle moves through a magnetic or electric field instead, it will be bent by the so-called Lorentz force $\vec{F}_L$:

$$\vec{F}_L = q \cdot (\vec{E} + \vec{v} \times \vec{B}), \tag{2.1.1}$$

with q being the charge, $\vec{E}$ the electrical field, $\vec{v}$ the velocity of the particle and $\vec{B}$ the magnetic field. Since in high energy hadron colliders only magnetic fields are normally used for bending and focusing, the electric field is usually dropped in Eq. 2.1.1. In circular accelerators the bending of the beam is achieved with dipole magnets.

To keep a beam particle on a circular trajectory, the centrifugal force $F_{Centr} = \frac{mv^2}{\rho}$ is equal to the Lorentz force $F_L = qvB$.

$$\frac{mv^2}{\rho} = qvB$$
$$\frac{p}{q} = \rho B \tag{2.1.2}$$

The ratio between the total momentum and the particle charge is called beam rigidity and it is measured in Tm. It quantifies how difficult it is to bend a beam. A beam with higher energy is harder to bend than a beam with lower energy, meaning that stronger magnets are required for the same bending angle but higher energy. Equation 2.1.2 can be approximated using

$$\frac{1}{\rho[m]} \approx 0.3 \frac{B[T]}{p[GeV/c]} \tag{2.1.3}$$

For FCC-hh, which aims to have a centre-of-mass energy of 50 TeV, dipole magnets with a magnetic field of 16 T are required, nearly double the magnetic field in the LHC dipoles of 8.33 T [6].
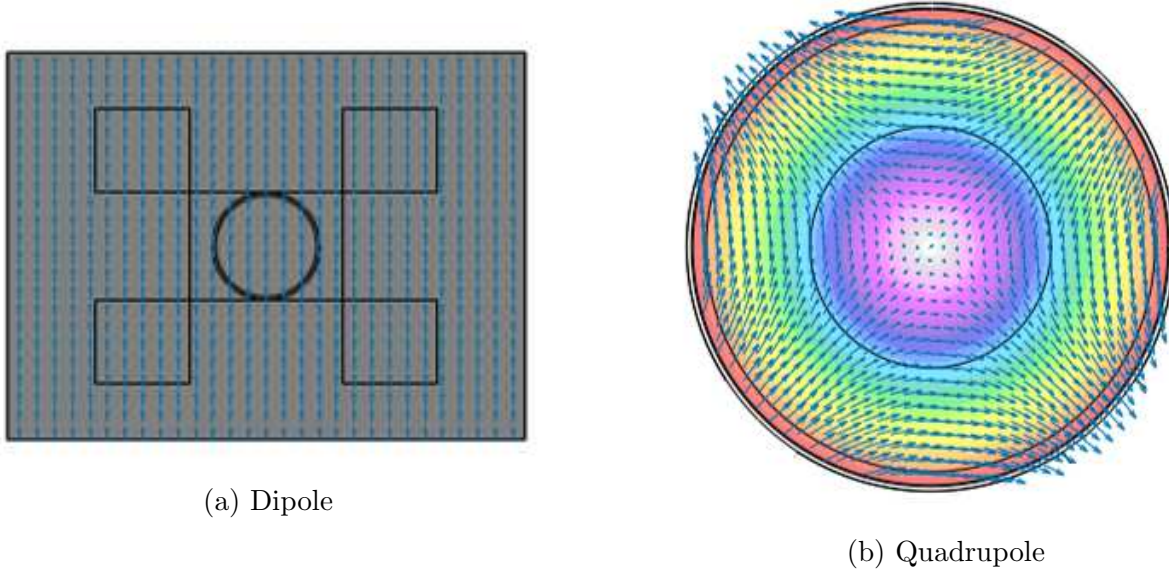
(a) Dipole

(b) Quadrupole

Figure 2.1.2: Magnetic field in a dipole and a quadrupole.

While dipoles are necessary for bending the beam, quadruple magnets are used for keeping the particles on the right position in the xy-plane. Compared to dipoles that have a magnetic field in one direction, quadrupoles have a magnetic field in the horizontal and vertical plane (Fig. 2.1.2). The magnetic fields in the horizontal and vertical plane are described as $B_x = -gy$ and $B_y = -gx$ with g being the gradient. The gradient is the characteristic parameter for quadrupole magnets, defining how strong this magnet focuses the beam. The normalised gradient is given as $k = \frac{g}{p/e}$ and it is measured in m^{-2}.

The force that a particle experiences in a quadrupole is $F_x(x) = -qvB_y(x)$ in the horizontal plane and in the vertical plane $F_y(y) = qvB_x(y)$, respectively. If a particle is located in the centre of the quadrupole, it will not experience any force because it is already at the perfect position. If the particle has an offset, it will be pushed into a different direction with a strength that is proportional to the displacement. If a quadrupole is focusing in the horizontal plane, then it is defocusing in the vertical plane and vice versa. So usually quadrupoles with alternating fields are placed after each other.

In general, a magnetic field can be expanded as Taylor series:

$$B_y(x) = B_{y0} + \frac{\partial B_y}{\partial x}\bigg|_{x=0} x + \frac{1}{2}\frac{\partial^2 B_y}{\partial x^2}\bigg|_{x=0} x^2 + \frac{1}{3!}\frac{\partial^3 B_y}{\partial x^3}\bigg|_{x=0} x^3 + ... \tag{2.1.4}$$

The first term equals the magnetic field of a dipole, the second term describes the magnetic field of a quadrupole, the third one the sextupole field and so on. In the accelerator itself,

higher order magnets, like sextupoles and octupoles can be found as well to correct the beam optics. Since they are not used in the project, they are not further discussed here.

If a linear approximation is made and it is normalised by the rigidity, the magnetic field can be expressed as:

$$\frac{B(x)}{p/e} \approx \frac{1}{\rho} + kx \tag{2.1.5}$$

with k being the normalised gradient and $\frac{p}{q} = \rho B$. This equation needs to be solved to describe the particle trajectory. Since this is not the subject of the thesis, it will not be further discussed.

2.1.3 Emittance and Beta Function

The emittance ε represents the spread of a beam of charged particles in momentum and position and is an intrinsic property of the beam.

The locations of a particle in phase space (position x, momentum x') turn after turn form an ellipse (Fig. 2.1.3). In a storage ring, where the beam is not accelerated, the area $A = \pi \cdot \varepsilon$ of this ellipse stays constant, according to Liouville's theorem [13]. It follows that the emittance ε is constant as well.
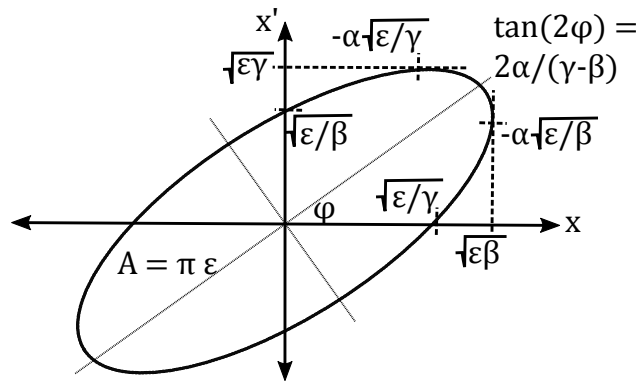
Figure 2.1.3: Ellipse in phase space created by the particles of the beam, with ε being the emittance, β being the beta function, ϕ the phase shift, and α and γ being two TWISS parameters that are not discussed here. [14]

If the beam is accelerated, the emittance is not constant but is shrinking as the energy increases. Therefore a normalised emittance is introduced that compensates for the change in energy:

$$\varepsilon_n = \gamma_r \beta_r \varepsilon \tag{2.1.6}$$

with γ_r being the Lorentz factor and $\beta_r = \frac{v}{c}$. In this thesis always the normalised emittance is used.

Here a Gaussian beam is assumed, where transverse positions and momenta of the particles may be well approximated by Gaussian distributions. For example, the distribution for the particle position in the horizontal plane can be described as

$$\rho(x) = \frac{N}{\sqrt{2\pi}\sigma_x} \cdot e^{-\frac{x^2}{2\sigma_x^2}}, \tag{2.1.7}$$

with the standard deviation written as

$$\begin{aligned} \sigma_x &= \sqrt{\varepsilon\beta_x} \\ \sigma_y &= \sqrt{\varepsilon\beta_y}. \end{aligned} \tag{2.1.8}$$

In Eq. 2.1.8 the so called beta function is introduced, with β_x and β_y the beta function in x and in y. The relation between emittance, beta function and beam root mean square (RMS) is essential to this project, and is used later on for calculating certain settings for elements in the beam line. The β function depends on the elements in the lattice and is given in meters. It varies along the ring, follows the periodicity of the ring and differs for the horizontal x and vertical y component.

Using the distribution of the particles in the beam, meaning the transverse phase space co-ordinates, the RMS emittance ε can be defined as

$$\varepsilon = \sqrt{\langle x^2\rangle\langle x'^2\rangle - \langle xx'\rangle^2} \tag{2.1.9}$$

with $\langle ...\rangle$ being the weighted averages and the second momentum of the quantities within.[15].

2.1.4 Luminosity

An important quantity to characterise the performance of an accelerator is the luminosity. It is proportional to the number of beam-beam collisions at an interaction point. The number of events, N_{Events}, per unit time is the product of the luminosity L in $\text{cm}^{-2}\text{s}^{-1}$ and the cross section σ in cm^2:

$$\frac{N_{Events}}{\Delta t} = L \cdot \sigma \tag{2.1.10}$$

Having high luminosity translates into a higher collision rate, so increasing this quantity is an objective for FCC. Compared to LHC, the luminosity in FCC-hh should be increased by a factor of 30 [6].

While a higher luminosity has a positive impact on the amount of data that is collected, it implies increased particle losses in the accelerator structure as well. For FCC-hh the aim is to reach an ultimate peak luminosity in the high luminosity experiments of $30 \cdot 10^{34}\ \text{cm}^{-2}\text{s}^{-1}$ [6].

The luminosity itself can be expressed as:

$$L = \frac{N^2 \cdot f_{rev} \cdot n_b}{4\pi\sigma_x\sigma_y} \qquad (2.1.11)$$

with N as the number of particles per bunch, n_b the number of bunches per beam, f_{rev} the revolution frequency and σ_x and σ_y respectively the rms beam size at the interaction point [16].

In terms of performance of an accelerator, the integrated luminosity is a crucial quantity since it is proportional to the number of events in the detector over a time span:

$$N_{integrated} = \sigma \cdot \int L(t) \cdot dt \qquad (2.1.12)$$

The ultimate integrated luminosity for FCC-hh will be $30\,\text{ab}^{-1}$ [6].

For the simulations later on it depends on whether operational damage or long time defects are studied, if either the instantaneous luminosity in $\text{cm}^{-2}\text{s}^{-1}$ or the integrated luminosity in cm^{-2} is used for the normalisation of the simulation results.

2.2 Beam Material Interaction

This section is split into three parts. First, several sources of radiation in accelerator structures are discussed. Second, the effects of the radiation on the accelerator equipment are explained. Special focus is put on the problems that are investigated in the simulations. Finally, it will be discussed what happens if particles move through matter and interact with the material. With this knowledge the simulations later on should be understandable from a physical point of view.

The material in this section is mainly based on [17], [18] and [19], where more detailed information can be foudn as well.

2.2.1 Sources of Radiation in Accelerators

Even though most of the time the beam should move through the accelerator without interacting with material, in some cases this is intended. Different beam-intercepting devices exist for various purposes like:

- Beam disposal on dumps or beam stoppers

- Machine protection and beam manipulation

- Beam extraction

- Particle production in targets

- Beam diagnostic devices.

Beam disposal either happens deliberately in the dumps or in case of emergencies at beam stoppers, that are inserted into the beam path. They are made of absorber material and have different dimensions, depending on the operational parameters, like beam intensity, brightness and dumping frequency. The dumps are the most irradiated places in the accelerator and therefore require heavy shielding to protect people and machine.

Machine protection are elements like collimators and absorbers. They are placed close to the beam and absorb particles to protect downstream sensitive areas, like superconducting[1] magnets. In the insertion region, several absorber elements are installed to catch high energetic secondaries. Secondaries are particles that are not contained within the beam but they are, for example, decay products. Furthermore, machine protection devices are used to protect the machine in case of malfunction, such as a miskicked beam because of a magnet error, and reduce background noise.

For shaping the beam, beam extraction targets like foils are used. If only a special kind of particles should be selected, for example particles with a certain polarisation, crystals can be used as well for beam extraction. In some cases the beam impacts devices purposely to create new particles for experiments, like in the Antiproton Decelerator to produce antimatter [20].

Beam diagnostic devices like wire scanners and SEM grids intercept with the beam and produce secondaries as well but they are considered to be non-invasive. Those devices are used to control and optimise the beam shape [15].

Even if the beam itself does not impact targets or the machine, secondaries can be produced in different processes like:

- Luminosity production
- Beam-gas collisions
- Dust and macro-particles
- Synchrotron radiation.

Luminosity production is the process that is responsible for the secondaries in this project. In this case secondaries are produced in the interaction points in collisions. These high energetic particles are scattered by a small angle and escape the detector cavern. They move into the machine in the insertion region and interact with the nearby accelerator equipment [21]. Since those secondaries have high energies, they also have a high impact on the machine. Therefore this so-called collision debris has to be carefully studied. In the beam pipe the beam moves through vacuum. This vacuum is not perfect and so some residual gas molecules still can be found in the vacuum chamber. If the beam interacts with those residual particles, secondaries are produced as well [22]. The same effect happens with dust that is in the machine [23]. This can lead to beam absorption and magnet quenches. In case of circular electron machines, synchrotron radiation is a source for secondaries as well, similar to Bremsstrahlung.

2.2.2 Radiation Damage

Losses of the beam and secondaries impacting the material have consequences for equipment and personnel. Different phenomena can be observed. Nuclear interactions can cause

---

[1]In the following, for superconducting magnets 'cold magnets' is used and for normal conducting magnets 'warm magnets'.

activation of the equipment [24], with the produced radionucleids depending on the decay chains and the material the particles are interacting with. This leads to access restrictions for people entering these areas until the area has 'cooled' down to acceptable radiation levels. The radiation is also impacting the surrounding environment, such as the electronics. The radiation to electronics can cause cumulative effects and single-event-effects [25]. Electronics exposed to radiation can suffer from single event effects that are the result of the ionisation of a single particle. This particle is able to deposit enough energy to perturb the operation of the device. These events can be destructive or non-destructive. It is important to understand the problems caused by radiation to electronics since the electronics make up a core part of the accelerator structure. Apart from radiation to electronics effects, high heat load can lead to thermo-mechanical stress in the elements like collimators.

In the following section an overview over the damages caused by collision debris that are faced in this project is given.

Quenching - Peak Power Density

Quenching of cold magnets is an instantaneous operational damage. A quench happens when particles deposit energy in the magnet, its temperature exceeds the critical temperature (T_C) and the magnet ceases to be superconducting. Consequently, the superconductivity breaks down and current cannot flow without any resistance anymore. This leads to further heating of the magnet and similarly the cooling liquid starts boiling. In the LHC the dipoles are cooled down to nearly $1.9\,\text{K}$ with liquid helium [26]. With the magnets being powered in series, this effect moves quickly on through the whole system, leading to further quenches in several other magnets. Therefore this phenomenon, that happens within a fraction of a second, has to be avoided [26].

The risk of quenching is quantified in terms of peak power density in the superconducting coils. Since quenching is a problem for cold elements, it is mainly studied for the cold quadrupole magnets and not for the dipoles and absorber elements that are normal conducting. The peak power density is expressed in mW/cm^3 and it is calculated averaging over the superconducting cables. The idea behind this is to average over the area where the energy dissipates (see Chapter 2.5). For this project a limit of $5\,\text{mW/cm}^3$ is assumed, which is considered to be conservative [6]. The goal is to stay below this value. As a prevention method absorber elements whose task it is to catch high energetic particles are placed in the accelerators. Since this is an instantaneous event, the peak instantaneous luminosity is used to normalise the simulation results.

Deterioration - Integrated Dose

The collision debris impacts the insulator material between the magnet coils as well. Over time the impacting dose leads to deterioration of the material and therefore to a subsequently damaged magnet. Compared to quenching, this effect is not an instantaneous effect but accumulates over time.

Because of the accumulated dose, the organic insulator material deteriorates and some of its properties, including tensile strength and electric resistivity, degrade. For lower energy accelerators in the MeV range this is not critical, since the insulator materials are inorganic,

like ceramics or glass. Those materials withstand high doses better than organic materials, like epoxy or G11 [27].

The radiation impacts the material in three steps. First, the radiation produces free radicals that then react in the second step. Different chemical processes, such as oxidation, gas evolution or the formation of unsaturated bonds, lead to a change of the molecular structure. This modification finally results in degradation of the insulator material. Certain circumstances like high temperature or the presence of oxygen enhance this process. The particles causing this deterioration are mainly particles, originate in electromagnetic showers, typically electrons and photons. This process is irreversible and highly localised.

In this project the upper limit of the peak integrated dose over the estimated lifetime of the FCC-hh machine is set to 30 MGy for the cold magnets. This limit is quite conservative. It is expected that it will rise to about 60 MGy-100 MGy [6]. If obtained values are below those critical values, the elements would survive the lifetime of the FCC project and would not need to be replaced, which is a huge advantage especially on the financial aspect.

Displacement per Atom

Similarly to the integrated dose the number of displacements per atom (DPA) is a long term effect. The number of DPA characterises the structural damage of inorganic materials, in particular of superconductors. For FCC-hh the critical current for the cold dipoles is $1500 \, \text{A/m}^2$, considering a field strength of 16 T and a temperature of 4.2 K [28]. The radiation occurring in the machine will affect the superconducting properties of the magnets, i.e. lower the critical values. It was found that with higher DPA the critical values of superconductivity, so T_C and B_C, are lowered which then leads to a higher risk of quenching [29]. Therefore it is important to keep the DPA as low as possible.

The number of DPA is proportional to the number of Frenkel pairs, N_F, in the material. A Frenkel defect happens when a high energetic particle hits an atom in a lattice, the primary knock on atom. This then is removed from its original position and is moved to an interstitial position, leaving a vacancy (Fig. 2.2.1). The combination the vacancy and the interstitial atom is called a Frenkel pair [30]. Similarly to Schottky defects it counts as a point defect [31]. The likelihood of Frenkel pair production increases with higher temperature.

The dimensionless DPA is given by,

$$\text{DPA} = \frac{A}{V N_A \rho} N_F \tag{2.2.1}$$

with A being the molar mass in g/mol, V the volume in cm^3, N_A the Avogadro number in mol^{-1}, N_F the number of Frenkel pairs and ρ the mass density in g/cm^3 [32]. A DPA of 0.5 means that on average 5 atoms out of 10 have been displaced from their original place in the lattice [33].

While the main reason for degradation of insulator material are electromagnetically interacting particles, other particles cause DPA as well. In case of FCC-hh around 90% of DPA is caused by neutrons, the rest is mainly caused by protons and ions (see Chapter 4.3). Even though neutrons are the majority, the protons have a worse effect on the DPA.
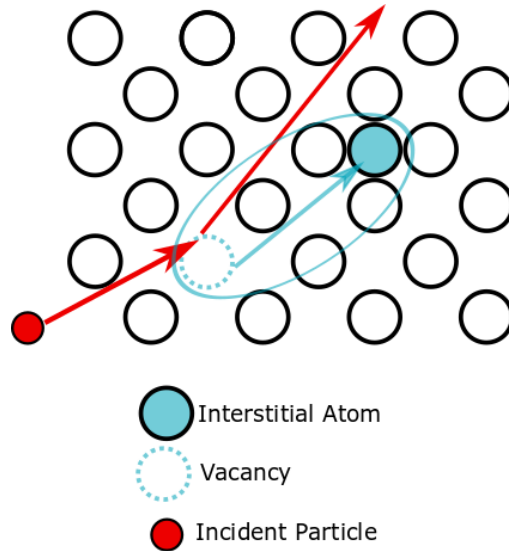
Figure 2.2.1: Visualisation of a Frenkel Pair in a lattice: The combination of the vacancy and the interstitial atom is the Frenkel Pair.

Contrary to the damages caused by dose in the insulator that are irreversible, the DPA would be reversible for temperatures higher than 700 °C. However, such high temperatures are not achievable for the cold magnets and no recovery happens at room temperature [28]. The DPA must be kept low enough, in order for the magnets to survive the lifetime of FCC-hh.

2.2.3 Atomic Interactions

A big fraction of the obtained secondaries are particles that are produced in interaction with the electrons of the atom. The interaction mechanics of photons as well as interactions of charged particles and energy loss of hadrons and muons will be presented in this section [18].

One of the main quantities to describe beam-material interaction is the cross section of an interaction type, which depends on the projectile energy E, the atomic number A and the mass number Z of the impacted material, $\sigma = \sigma(E, A, Z)$. Usually the microscopic cross section is given in barn, where $1\,\text{barn} \equiv 10^{-24}$ cm^{-2}. Additionally, the mean free path, that is the distance a particle travels inside a material between two collisions is $\lambda = \frac{1}{N\sigma} = \frac{M}{\rho N_A \sigma}$, with N being the atomic density, M the molar mass, N_A the Avogadro constant and ρ the material density.

Electromagnetic Interactions

Several electromagnetic interactions exist that contribute to the energy deposition in different energy ranges.

- *Coherent scattering or Rayleigh scattering*: In this type of scattering a photon is scattered at a bound electron from an atom (Fig. 2.2.2). The photon does not ionise or excite the atom in this process. Furthermore, the photon keeps its energy because the recoil energy of the atom is negligible. Since in this process the photon does not lose

energy, it is not crucial for energy deposition studies. The cross-section scales with $\sigma \sim Z^2$.

- *Photoelectric effect*: The impacting photon is absorbed in this process and an electron is released from the atomic binding. In more detail, if a photon with an energy higher than the binding energy, $E_0 > U_i$, interacts with the atom, an electron with the energy $E = E_0 - U_i$ is emitted. If an electron of an inner shell is involved, an atomic relaxation follows. This means that the vacancy in the inner shell then is filled with an electron from an outer shell. This process leads to the emission of a characteristic X-ray or an Auger electron[2]. With the cross-section scaling like $\sigma \sim Z^{4-5}$, this process strongly depends on the atomic number. This process is dominant for the lower energy ranges around keV and low MeV (Fig. 2.2.3).

- *Incoherent scattering or Compton scattering*: Here, a photon interacts with an atom and transfers energy to an emitted electron (Fig. 2.2.2). Contrary to the photoelectric effect, the photon is not absorbed. The energy of the electron after the interaction can vary from a small fraction of the energy of the original photon to the majority of its energy. This effect can be followed by an atomic relaxation. Compared to the photoelectric effect, this process has a weaker dependence on the atomic number with $\sigma \sim Z$ and is dominant in the MeV energy region (Fig. 2.2.3).

(a) Rayleigh Scattering   (b) Photoelectric Effect

(c) Compton Scattering   (d) Pair Production
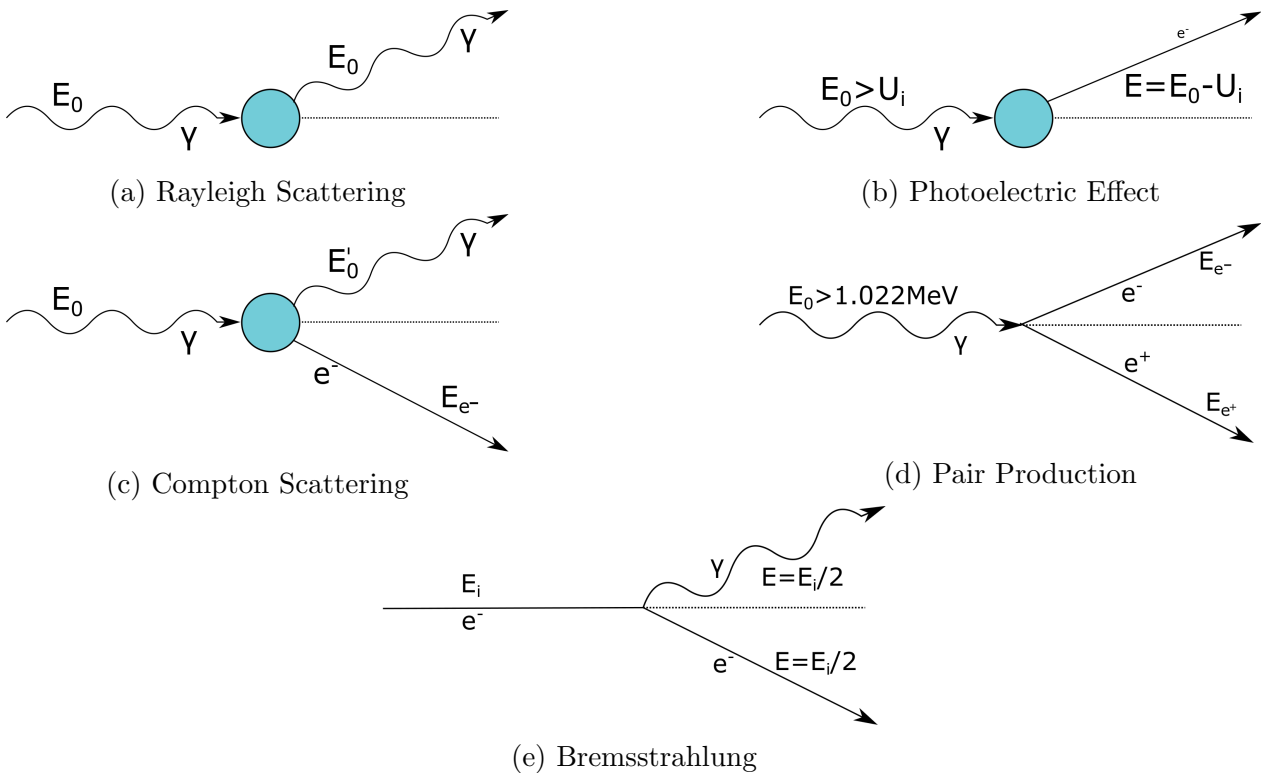
(e) Bremsstrahlung

Figure 2.2.2: Electromagnetic Interactions.

- *Electron positron pair production*: This process, in which a photon creates an electron and positron in the field of a nucleus, is dominant at high energy ranges, with a threshold energy of $1.022\,\text{MeV}$ (Fig. 2.2.2). This energy is equal to the combined rest energies

---

[2]An Auger electron appears if an electron from an inner shell of an atom fills a vacancy further in the atom. The released energy then leads to the emission of an additional electron, the Auger electron.

of an electron and a positron. For high energies pair production is relevant for the observed electromagnetic cascades. The cross-section scales with $\sigma \sim Z^2$ and the energy, for which this process becomes dominant is smaller for high Z materials (Fig. 2.2.3).

- *Bremsstrahlung*: For high energies, electrons and positrons can lose energy through Bremsstrahlung. In this case, the electron emits a photon that has a fraction of the energy of the original electron (Fig. 2.2.2). Similarly, the energy of the electron also is reduced.

A comparison between the different cross sections and in which energy ranges they are dominant is given in Fig. 2.2.3.
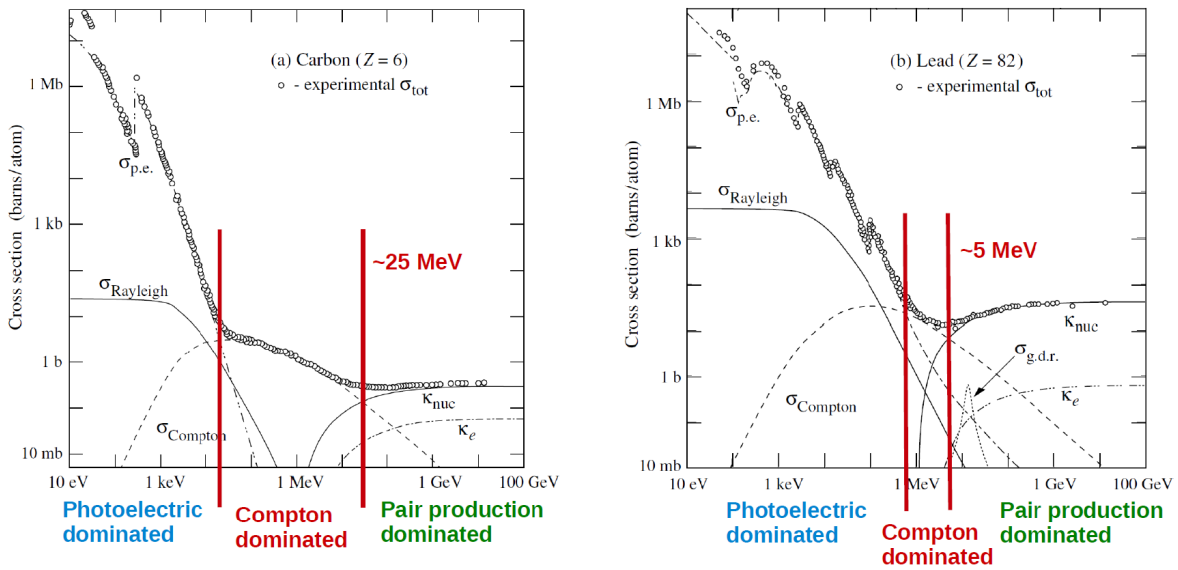

Figure 2.2.3: Comparison of cross sections with the total cross section displayed as points. For high Z materials like lead, the Compton dominated range is much smaller than for low Z elements [18] [34].

Interactions of Charged Particles

Charged particles interact electromagnetically with the atomic electrons as well as with the nucleus of the material.

In the first case Coulomb interactions with electrons lead to excitation or ionisation of atoms. In case an electron with high energy is ejected in the ionisation process, it is known as δ-ray. Depending on the type of incident particle, this process is dominant for different energy ranges. For electrons and positrons it is dominant up to a few $10\,\mathrm{MeV}$, for muons up to a few $100\,\mathrm{GeV}$ and for charged hadrons even higher. For hadrons with higher energies above GeV, inelastic nuclear collisions occur as well. They are less frequent but they are crucial for energy dissipation in the material.

'Electronic energy loss' is also responsible for the temperature rise of the material. While the energy transfer is small in such a Coulomb interaction, the inelastic cross sections are rather large and therefore the probability of an interaction is large.

The Coulomb interactions with the nuclei instead, are responsible for the angular deflection of charged particles interacting with material. In general, particles with higher energies have a smaller deflection angle. Comparing light and heavier particles with the same energy, particles with lower rest mass are scattered more.

The energy loss of particles caused by interaction with the nuclei is lower than in case of interaction with the electrons, except for low energy heavy projectiles for which NIEL (Non Ionising Energy Loss) can be observed. In case the energy is high enough, this type of interaction causes DPA.

For even higher energies radiative losses are observed. In case for electrons and positrons this happens above a few 10 MeV, with Bremsstrahlung dominating the energy loss, emitting a photon. For muons radiative losses happen above a few 100 GeV, with Bremsstrahlung, electron-positron pair production and photo-nuclear interactions.

Depending on the process, the mean energy loss per unit length is either called electronic stopping power, nuclear stopping power or radiative stopping power.

Energy Loss of Hadrons, Muons, Electrons and Positrons

The mass stopping power for muons or hadrons is usually expressed as $\frac{\text{MeV} \cdot \text{cm}^2}{\text{g}}$, which is equal to the stopping power multiplied by the material density. Over a large range in the area from 10 MeV to a few 10 GeV electronic stopping power for muons and hadrons is described by the Bethe-Bloch equation [35]:

$$-\langle \frac{dE}{dx} \rangle = \frac{4\pi}{m_e c^2} \cdot \frac{nz^2}{\beta_r^2} \cdot (\frac{e^2}{4\pi\varepsilon_0})^2 \cdot [\ln(\frac{2m_e c^2 \beta^2}{I \cdot (1 - \beta_r^2)}) - \beta_r^2] \tag{2.2.2}$$

In Eq. 2.2.2

- E is the energy

- x the travel distance into the target with an electron number density n and mean excitation potential I

- $\beta_r = \frac{v}{c}$ with v being the velocity of the particle

- e and m_e the electron charge and mass

- ε_0 is the vacuum permittivity

- n is the electron density and can be calculated with $n = \frac{Z \cdot \rho}{A \cdot u}$, where ρ is the density of the material, u the atomic mass unit, Z the atomic number and A the mass number.

Since this equation is proportional to Z/A, the stopping power does not depend strongly on the material the particle is interacting with. The loss does not depend on the mass of the impacting particle, but it depends on its velocity and its charge. For low energies, meaning $\beta_r \gamma_r \approx 0.1 - 1$, $\frac{dE}{dx}$ is proportional to $\frac{1}{v^2}$. With the minimum stopping power at $\beta_r \gamma_r \approx 3 - 3.5$, particles with such a velocity are known as minimum ionising particles and they have a stopping power of around 1-2 $\frac{\text{MeV} \cdot \text{cm}^2}{\text{g}}$ (Fig. 2.2.4). For even lower energies the stopping power is found by empirical data. For high energies above a few 100 GeV, radiative losses dominate the process.

Compared to hadrons and muons, radiative losses become dominat at lower energies, i.e. for electrons and positrons above a few 10 MeV for low Z and above a few 1 MeV for high Z materials.
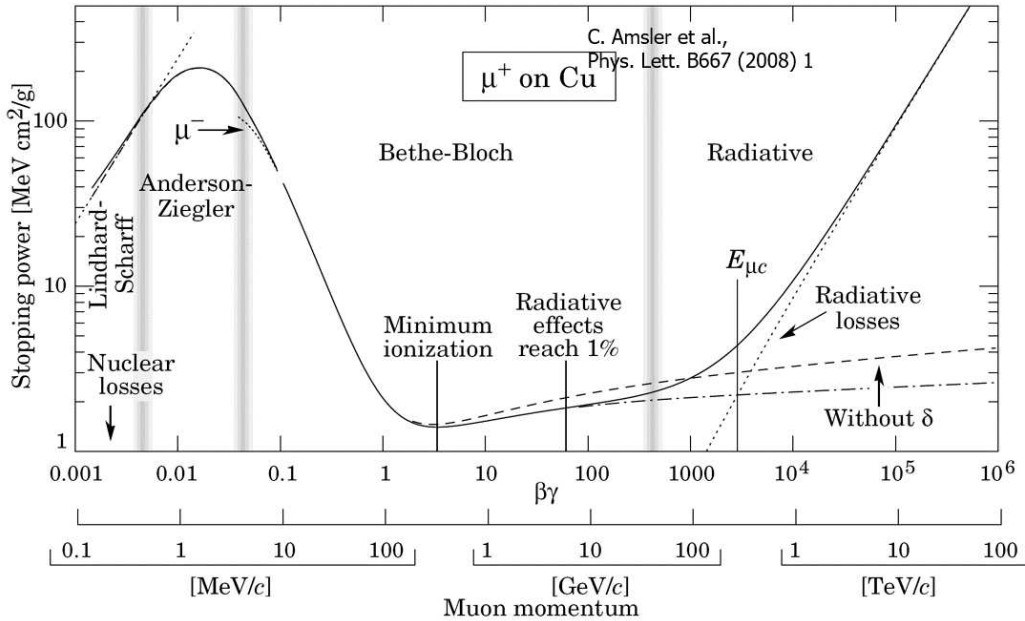

Figure 2.2.4: Stopping power of a positive muon hitting copper. [36]

2.2.4 Nuclear Interactions

Hadron Nucleus Collision

In a hadron machine like FCC-hh, in which protons or ions are collided, the physics of hadron nucleus collisions is a crucial ingredient. Going down one level deeper into fundamental physics, it is shown that elastic and inelastic collisions between hadrons and nuclei are caused by the strong force. In inelastic interactions the internal structure of either the nucleus, the impacting particle or both is changed. The ideal cross-section of a nucleon-nucleon interaction is the sum of all elastic and inelastic cross-sections. At higher energies, above a few GeV, the cross-section becomes energy independent (Fig. 2.2.5).

The hadron-nucleus interaction can be divided into two stages, the fast and the slow stage. The fast stage happens within 10^{-22} s, where new particles can be produced if the energy is high enough, i.e. above 1 GeV. In this process the most abundant products are pions, which are the lightest hadrons. By definition mesons consist of two quarks. Pions are mesons that consist of an up and a down quark or a superposition of these two. In case of a nucleus-nucleus collision the production threshold of pions is 290 MeV. As pions are created so easily, they dominate the area close to the interaction point.

In this stage hadrons, such as protons, neutrons or pions can form intranuclear cascades, in which particles with high energy can leave the nucleus. As already mentioned before, such particles with high energy are mainly focused into the forward direction. The multiplicity of the cascade scales with $log(E)$. Particles that do not have enough energy to launch a cascade still can deposit their energy in the nucleus, leaving it in an excited state.
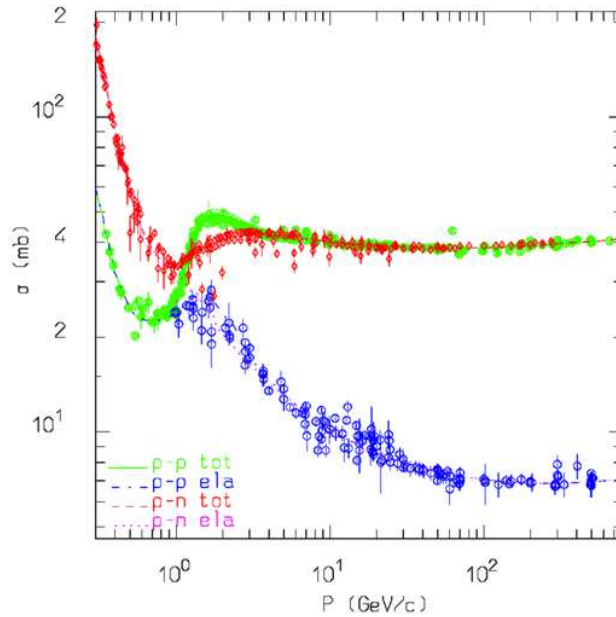
Figure 2.2.5: Total and inelastic p-p and p-n cross sections, given as the momentum of the proton. [17]

The slow phase, also known as the de-excitation state, happens after 10^{-16} s. In this state the *evaporation* phase happens, where neutrons with lower energy (MeV), protons and light fragments, like α-particles are emitted isotropically from the excited atoms. In case of heavy elements, *fission* is more likely to happen. In this process the nucleus breaks up into larger residuals than the previously mentioned α-particles. These residuals can undergo evaporation processes by themselves and they can also be radioactive.

Low-Energy Neutron Interactions

Compared to all other neutral hadrons, neutrons are the only fairly stable hadrons with a lifetime of $\tau = 15\,\text{min}$. Not carrying any charge, they can be really penetrating. Over a big energy range, down to a level of MeV they are slowed down by elastic scattering. If the energy gets even lower, at a certain point they are thermalised and captured by a nucleus. The cross-section of this kind of neutron capture is inversely proportional to the velocity of the moving neutron. This means that a slower thermal neutron is more likely caught than a fast one. The capture of neutrons is also known as radiative capture, if the capture is then followed by a gamma emission. For heavy materials, neutrons can be the cause for fission.

Inelastic interactions that occur above a certain threshold energy contribute as well to the deceleration of neutrons in the range of MeV. In those inelastic interactions, one or more neutrons with lower energy are emitted from a subsequently excited nucleus.

2.2.5 Energy Deposition and Particle Showers

All phenomena discussed in the previous section contribute to the interaction of beam particles with matter.

Chapter 2 Key Concepts and Principles

The main contribution is given by Coulomb interactions of charged particles that are caused in atomic and nuclear processes. It is also worth noting that energy deposition and energy loss of particles is not necessarily the same thing, since energy can be transported away by δ-rays and secondaries.

In case of lower energy charged hadrons up to an energy of hundreds of MeV, the energy deposition is characterised by a distinct peak at the end of the range, the so-called *Bragg* peak (Fig. 2.2.6). For electrons this peak does not exist, while in case of protons the angular deflection is smaller and most protons are stopped in the same spot. This property of low-energy protons is used in medical facilities for cancer treatment, since the peak can be exploited to focus energy deposition in a localised region, minimising damage to healthy tissue [37].
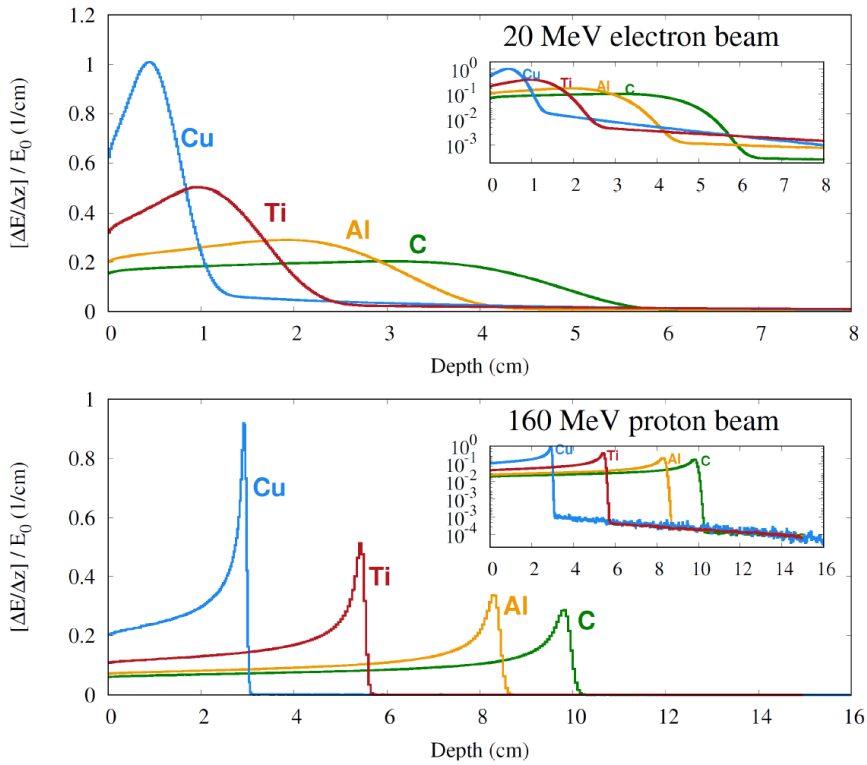

Figure 2.2.6: Bragg peak for electrons and protons. [18]

Another large contribution to energy deposition is through electromagnetic showers that involve photons, electrons and positrons. At high energies electrons and positrons mainly lose energy through Bremsstrahlung where a photon is produced and the electron loses a certain amount of its original energy. The photon then can produce another electron positron pair, in which the average energy of the electron and positron, respectively is half of the energy of the original photon. This phenomenon happens in an energy range above GeV. In each step the energy of the produced particles decreases until the energy is not sufficient anymore to perform Bremsstrahlung or pair production. Then the cascade dies and ionisation and excitation become dominant.

If a high energy hadron undergoes an inelastic interaction, several energetic secondaries can be produced. These products, like neutrons, pions, protons, etc are causing further collisions giving rise to a particle multiplication called hadronic shower. As those particles have high energies, their angular spread is small and they are mainly directed forward. In this process

20

a non-negligible amount of energy is consumed by breaking up binding energy and recoils of nuclei. As discussed before, lower energy particles are produced in de-excitation, evaporation and fission. With several neutral pions produced that then decay into two photons, a hadronic shower also has an electromagnetic component, whereas an electromagnetic shower hardly ever initiates a hadronic shower. The hadronic shower decreases as soon as the energy level goes below the pion production level, that is in the energy range of a few $100\,\mathrm{MeV}$. The depth of the shower in the material is proportional to $log(E_0)$.

2.3 Monte Carlo Simulation

In this section the necessity of Monte Carlo simulation for this project is discussed, as well as the theoretical background.

The Monte Carlo method was originally developed to solve multi-dimensional integro-differential equations with the help of stochastic processes by John von Neumann, Stanislaw Ulam, Nicholas Metropolis [38] [39] and separately Enrico Fermi. It was also found that this method is helpful for simulating particle transport and interaction since it is a stochastic process. In principle one can roughly differentiate between simulations where the history of each particle has to be thoroughly tracked, for example for medical applications, or simulations where the only quantity of interest in the expectation value. For the latter case the correct simulation of the variations and fluctuations are not of high importance. Such a set-up is used in case of energy deposition studies, like they are studied in this thesis. Whereas the first type is slow but accurate in the fluctuations and correlations as well, the values converge much faster in the second case. This acceleration of convergence is achieved with a modified biased process in respect to the original value but it leads to the same expectation value. This type of simulation has the advantage that problems of any complexity can be solved.

As underlying literature the books [40] and [41] were used in this chapter.

Phase Space and Boltzmann Equation

In statistical mechanics the phase space is crucial. It consists of six dimensions that represent the degrees of freedom, where three dimensions are used for the real space (x, y, z) and three dimensions are used for the momenta (p_x, p_y, p_z). In case of more degrees of freedom, the number of dimensions of the phase space increases. An important quantity is the so called phase space density $n(t, x, y, z, p_x, p_y, p_z)$ that gives the number of particles in an infinitesimal volume of the phase space. If the phase space density is then multiplied by the velocity of the particles, $n\mathbf{v}$, one obtains the rate of the path length density that is crucial to the interaction of particles with matter. This quantity is further known as angular flux, $\Psi = n\mathbf{v}$. Using the fluence, Φ, the angular flux is also known as

$$\Psi = \frac{\partial^3 \Phi}{\partial t \partial E \partial \vec{\Omega}} = \dot{\Phi}_{E,\vec{\Omega}}, \tag{2.3.1}$$

with all the phase space coordinates in the denominator. The fluence is known as

$$\Phi = \int_E \int_{\vec{\Omega}} \int_t \dot{\Phi}_{E,\vec{\Omega}} dE d\vec{\Omega} dt. \tag{2.3.2}$$

Usually no dependence in time t is assumed, to the fluence is given with $\Phi(E) = \frac{d\Phi}{dE}$.

The Boltzmann equation is a balance equation in phase space. In particle transport codes this equation is solved in its integral form with Monte Carlo simulation. Using the quantities discussed before and x being all the phase space coordinates, the Boltzmann equation is given as

$$\frac{1}{v}\frac{\partial \Phi(x)}{\partial t} + \vec{\Omega} \cdot \nabla \Phi(x) + \Sigma_t \Phi(x) - S(x) = \int_{\vec{\Omega}} \int_E \Phi(x) \Sigma_S(x' \to x) dx' \tag{2.3.3}$$

According to Eq. 2.3.3, the sum of all production terms minus the destruction terms is equal to the increment of the particle density in an infinitesimal volume of the phase space:

- The first term $\frac{1}{v}\frac{\partial \Phi(x)}{\partial t}$ describes the time dependent change of the angular flux, caused by particle decay, for example.

- $\vec{\Omega} \cdot \nabla \Phi(x)$ represents the change of energy and direction caused by the translation movement

- Absorption of particles is described with $\Sigma_t \Phi(x)$, where Σ_t is the macroscopic cross section. The macroscopic cross section is the inverse of the mean free path.[3]

- The source of all particles is given by $S(x)$

- The right hand side describes the scattering, i.e. the change of the angular flux, with Σ_S being the macroscopic scattering cross section.

In order to solve the Boltzmann equation with Monte Carlo simulations it is necessary to have at least one source of particles as well as detectors. In this project proton-collisions are used as a source and the detectors are the scorings on the elements in the line.

Mathematical Background to Monte Carlo Simulation

The goal of the Monte Carlo simulation is to find the expectation value of a certain problem. The mathematical foundation for this is given by the Central Limit Theorem (CLT).

To understand the concept of CLT it is important to define the mean of a distribution. The mean of a function $A(x)$ depending on the variable x over a closed interval $[a, b]$ is given as

$$\bar{A} = \int_a^b A(x)f(x)dx. \tag{2.3.4}$$

Here $f(x)$ is the normalised probability density function (PDF), which implies that it is defined over an interval $[a, b]$, where $b > a$ and a and b are real numbers or infinite limits. Furthermore, the PDF is non-zero, and is normalised in such a way that $\int_a^b f(x) = 1$.

---

[3]The mean free path is the average distance a particle travels through a material without collisions.

In Eq. 2.3.4 the mean of a function in one dimension is given. In a similar way it is possible to calculate the mean of a multi-dimensional integral,

$$\bar{A} = \int_x \int_y \int_z ... \int A(x, y, z, ...) f(x) g(y) h(z) ... dx dy dz... \tag{2.3.5}$$

A multi-dimensional integral is often too complicated or impossible to solve with common methods. Sampling N values of $A_i(x_i, y_i, z_i, ...)$ with the probabilities $f(x)g(y)h(z)$ and then dividing it by the number of samples leads to

$$S_N = \frac{\Sigma_1^N A_i(x_i, y_i, z_i, ...)}{N}. \tag{2.3.6}$$

If the number of samples is very high ($N \to \infty$) the value obtained in Eq. 2.3.6 is equal to the mean value:

$$\lim_{N \to \infty} S_N = \lim_{N \to \infty} \frac{\Sigma_1^N A_i(x_i, y_i, z_i, ...)}{N} = \bar{A}$$
$$\lim_{N \to \infty} P(S_N) = \frac{1}{\sqrt{\frac{2\pi}{N}}\sigma_A} e^{-\frac{(S_N - \bar{A})^2}{2\sigma_A^2/N}} \tag{2.3.7}$$

In Eq. 2.3.7 the central limit theorem is given. It states that for large N the sum of the averages of N independent, random variables identically distributed tends to a normal distribution with mean value $\bar{A}$ and variance σ_A^2/N. This also implies that the more samples are given, the closer you get to the 'real' expectation value, meaning that

$$\text{Accuracy} \propto \frac{1}{\sqrt{N}}. \tag{2.3.8}$$

Comparing this to other traditional methods that converge with $N^{-1/n}$, with n being the number of dimensions, Monte Carlo simulation converges faster for two dimensions or more. Since the Boltzmann equation depends on seven dimensions, Monte Carlo simulation is the fastest way to solve the equation.

As it already has been established, a random sampling from the PDF is required for a Monte Carlo simulation. Since it is not possible to create real random numbers with algorithms, pseudo random numbers are used. After a certain number of digits, the sequence is repeated, i.e. they are periodic. It is necessary that the period of the pseudo random numbers is longer than the necessary numbers required, otherwise the result would be biased. Several methods to produce pseudo random numbers exist, but they are not discussed here.

Particle Transport with Monte Carlo Simulation

In the case of particles moving through matter, the Monte Carlos simulation works as described below. The simulation follows every particle individually. For every step the occurrence and the outcome of the interaction is decided randomly following the given probability distribution, that defines which events are more likely to happen than others. Next, all produced secondaries are followed until they are absorbed, lost or fall below a specific threshold, e.g. energy. The information is stored, and the next primary is simulated.

For performing a Monte Carlo simulation for particle transport several assumptions are generally made. First, the geometry has to be static, and the material is homogeneous and amorphous. This represents a challenge in case of moving elements. Furthermore, the material properties are not affected by particle reactions. So for example even though the material is impacted by the dose, its properties do not change. This does not represent the reality. Another assumption is that the particles do not interact with each other, they only interact with individual electrons, nuclei, molecules, etc of the material. Finally, for the simulation a Markovian process is assumed [13]. This means that the history of a particle does not matter, so the next step of a particle does not depend on the previous ones.

2.4 Simulation Tools: FLUKA, FLAIR, Linebuilder

FLUKA - The Particle Transport Code

As discussed in the previous section, Monte Carlo simulation is a powerful tool for particle tracking. For this, several particle tracking codes exist, such as FLUKA [42] [43], Geant4 [44] or MCNP [45]. In this thesis the simulations are performed with FLUKA. FLUKA stands for "Fluktuierende Kaskade" and is based on a Fortran code. FLUKA is used for simulating the particle transport itself, as well as the interaction between particles and matter. The applications of FLUKA are varied, and include shielding design, calorimetry, as well as target and detector design.

The main focus of FLUKA is to provide a code that represents sound and modern physical models, and provide consistent results. Furthermore, conservation laws are enforced after each step. With this high accuracy it is possible to make predictions for data where no experimental data exists so far.

In FLUKA it is possible to simulate 60 different kind of particles with high accuracy. Each type of particle has a certain ID number (see Appendix B). Different kind of particles are simulated in different ranges. So electromagnetic particles like electrons, positrons and photons are simulated in a range from 100 eV-1 keV up to a few 1000 TeV. Hardly interacting particles like neutrinos and muons can be simulated in any energy range. Hadrons can be simulated up to 20 TeV using the standard routines. It is possible to simulate them up to 10 PeV, if the DPMJET generator [46] is linked. This strategy is used in this project, since collisions at 50 TeV are simulated.

With FLUKA it is possible to simulate highly complicated geometries with the Combinatorial Geometry (GC) [47] package. Customisable user routines allow maximum flexibility. For the

standard tasks, there is the possibility to work with FLAIR [48], the graphical user interface of FLUKA.

Each simulation needs its own FLUKA input file. This is a simple human readable text-file with the ending '.inp'. Commands are given with so-called cards that go over one line or more in certain cases. Even though this input file is different for each simulation, the underlying structure is the same:

- Title of the project

- In the *physics* settings all properties regarding the beam, its energy and its shape are defined. The particle source is defined as well. Several options for the particle source are available, like collisions or loading particles from another file. For the beam profile several shapes can be selected. The simplest beam is a simple point-like pencil beam.

- Description of the geometry of the problem, which is split into two parts: the definition of the used *bodies* and *regions*. The bodies can overlap and are either finite or semi-infinite bodies. With the help of Boolean operators so-called zones are created. Several zones together then make up a region. It is important to know that each point in the geometry has to belong to one and only one region. If a point belongs to no region an error is given.

- This is followed by the definition of the *materials* used in the project. Either the material is already implemented in FLUKA or the user also has the possibility to create a new material.

- Next, each region then has material assigned. With this, all geometry related steps are completed.

- In the following the 'detectors' have to be implemented in terms of *scoring* cards. The user can freely choose the mesh of the scoring and which property is measured. Without those detectors the user would not receive any results. It is not necessary though to have scoring on each element of the line. It is possible to have several overlapping scoring volumes on the same element, either for different quantities or in a different resolution.

- Optionally, the user can apply *biasing* and energy cut-offs. One has to be cautious to not cut off important information, so those techniques have to be handled with care.

- Eventually, a *randomise* card that initialises the random number sequence follows. The last two cards are then given with the start and end simulation card.

With so much information, such an input file easily can reach several hundred lines and be hard to work with for the user. Therefore FLAIR was developed, to facilitate the work with FLUKA.

FLAIR - FLUKA Graphical Interface

FLAIR [48] (FLUKA advanced interface) is a graphical user interface based in Python. It is made to facilitate the work with FLUKA which is Fortran based and critical for syntax errors, especially in regard to alignment errors. The huge input files that were previously discussed and are in a common ASCII text file can be opened with FLAIR and are much

clearer to understand as such. FLAIR is based in Python, more specifically Tkinter, while Gnuplot is used for plotting. It is aimed to give FLAIR a native look to users, similar to other modern programs.

With FLAIR it is possible to create and check the input files and in particular the geometry. Errors are highlighted so they can be spotted easily. Furthermore, it is possible to directly compile input files in FLAIR, as well as to start a simulation and to check the output files for errors or problems. After the simulation has finished the user can post process the data to get human readable results that can be plotted as well in FLAIR. For this thesis, especially creating and checking of input files as well as most plotting of results was done in FLAIR.

The main goals of FLAIR are to make a complex code like FLUKA simple and intuitive to use. The input editor is an integral part of FLAIR, with the FLUKA input cards displayed as a mini-dialogue. While the FLAIR window is telling the user which values should be written in the different fields, it then automatically converts the information and plugs it into the right position and format in the FLUKA input card. With a right click, help can be accessed with the information window opening, providing the user with documentation for this type of card. Compared to other programs, the common conventions like the short cuts for copy and paste etc are kept. Furthermore, while working on an input card in FLAIR, the same input card is displayed in the bottom as it is written in FLUKA. So the functionality of FLUKA is not hidden and can be seen by the user (Fig. 2.4.1).

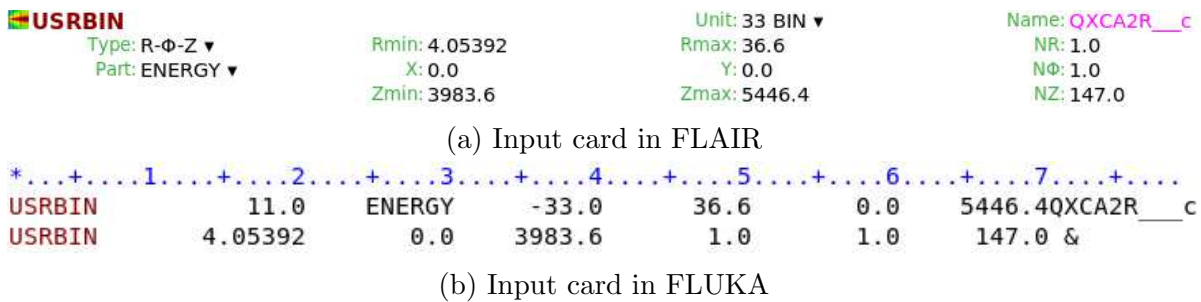
(a) Input card in FLAIR

(b) Input card in FLUKA

Figure 2.4.1: The same input card in FLAIR and FLUKA. While working in FLAIR, the FLUKA input card is permanently visible. Changes made in FLAIR are immediately shown in FLUKA.

While setting scoring, physics properties, biasing etc in the input editor, building the geometry can be done in the geometry editor. The geometry is displayed in different perspectives, in maximum four windows (Fig. 2.4.2). It can be selected which properties, like 3D, lattice, material or geometry, should be shown. If errors appear while designing or adapting an element they are displayed in red to facilitate the corrections. For transformation of bodies the option of selecting several of them at once and adapt them simultaneously exists.

A big part of the simulation is the analysis of the results in a visual way. For this, several plotting tools are already implemented in FLAIR and can be selected with a graphical interface. In general, 1D max, 1D average, the geometry, the field or 2D maps can be plotted. For more advanced plotting, it is possible to add Gnuplot lines in the window below and create more personalised plots.

Simpler simulations that imply a limited computational effort are done completely locally on the machine itself in FLAIR. For more complex simulations like in this project, this is not feasible anymore, so some additional tools have to be used.
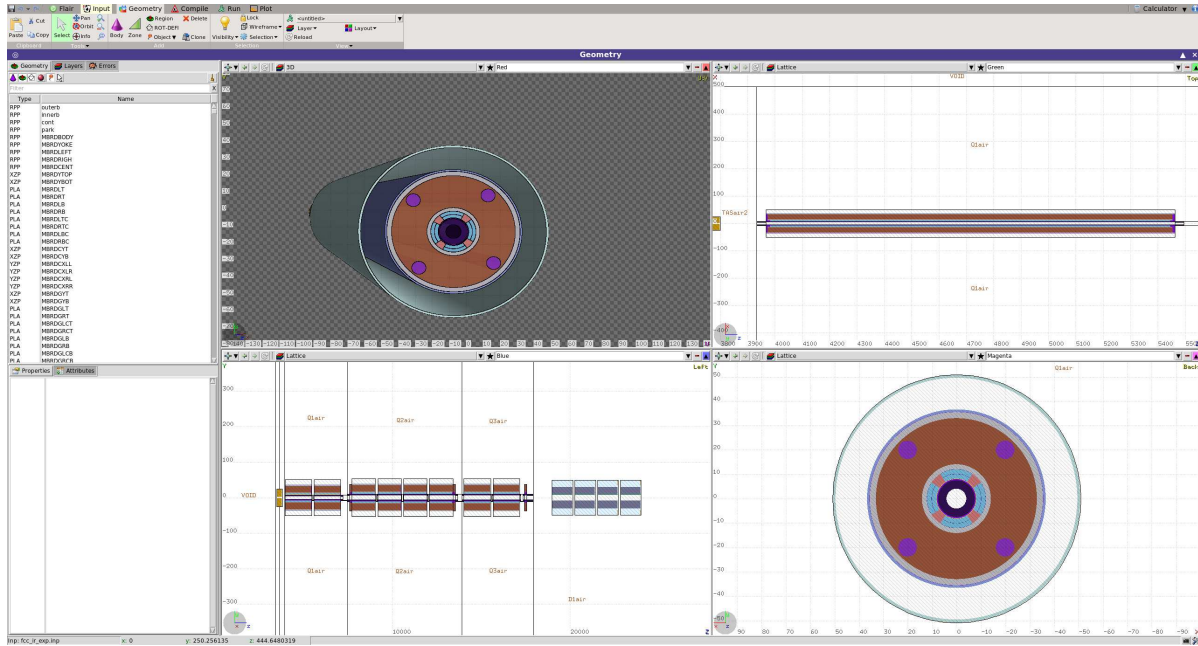
Figure 2.4.2: Screenshot of the geometry viewer in FLAIR.

Linebuilder - Framework for assembling comprehensive simulations

As mentioned above, creating the input file for a comprehensive simulation like an insertion region of FCC-hh solely with FLAIR is impractical. To solve this problem, a framework called 'Linebuilder' [49] to dynamically assemble complex input files was developed. Similarly to FLAIR it is Python based. Using Linebuilder the FLUKA models of the accelerator components are immediately placed in the correct position in the line, they have the correct magnetic field and the scorings are automatically set up. This tool enables to set up the simulations in a faster way.

All elements are stored in the FEDB (FLUKA element data base), where each of them is built in a file itself around the origin. Those files are then split into three files, 'machine_name.bodies', 'machine_name.regions', 'machine_name.materials', where all the information about the element is stored. Additionally, there is the possibility of so-called assemblies, where an element is built from several parts that can have different relative positions to each other. Usually collimators are stored as assemblies, with the jaws then automatically positioned correctly with an additional collimators file. As soon as Linebuilder is launched, these files are used to build the geometry. In case of errors appearing, debugging is easier with Linebuilder since each element is set up in a separate file.

The correct position of the elements is given in the TWISS file which is produced with MAD-X [50], an optics code. In this file, not only the position and length of the elements can be found, but also the gradient for quadrupoles and the field strengths for the dipoles. From a beam related point of view, the TWISS file provides the expected transverse displacement of the beam position in x and y for each position along the beamline. It is always necessary to provide a TWISS file for both beam directions.

The general configurations are summarised in the 'inputcard.txt, which is a simple text file. There the name of the project is given and the files that should be included, as well as

additional user routines that need to be used.

Further information needed by Linebuilder is spread in some configuration files in the folder of 'customized_files'. In particular, files are provided for customised scoring, biasing, physics settings, beam setting, beam pipe profile and tunnel settings. Additionally, the input file for the tunnel geometry, in either 2D or 3D, is stored in this folder.

To select which elements are included in the line, Linebuilder uses a file called 'prototypes.lbp', where all elements that are used for the simulation are listed. In addition to the name, the magnetic length and the type of magnetic field is given, as well as the scoring for the elements is implemented here. If the name of an element in the TWISS is different to the name in the FEDB, then it is also possible to note this in this file, and Linebuilder will be able to associate the element in the TWISS file with the described FEDB model. When Linebuilder is launched it goes through the TWISS file, reads the element names and looks for an element in the prototypes file with the same name. If a match is found, the element is then placed at the correct position, otherwise it is ignored. Similarly, if an element appears in the prototypes file but not in the TWISS file it is ignored.

For elements that should be added to the line but that are not part of the TWISS file so far, an additional files folder exists, where such elements can be implemented. If collimators are used in the simulation, the file that provides information about the jaw opening and further collimator properties are stored in this folder as well.

Finally, Linebuilder is launched by calling the script and the input card. The script automatically assembles the geometry and sets up scoring, magnetic fields, etc, leading to the input file in the correct FLUKA syntax (Fig. 2.4.3). Before starting the simulation, the user should thoroughly check the input file for potential errors. For checking the magnetic fields it is recommended to launch a trajectory check simulation first. The (x, y, z) position of beam particles can be saved in an output file and compared to the (x, y, z) values of the TWISS file. If it is assured that these data overlap, the complete simulation can be started.
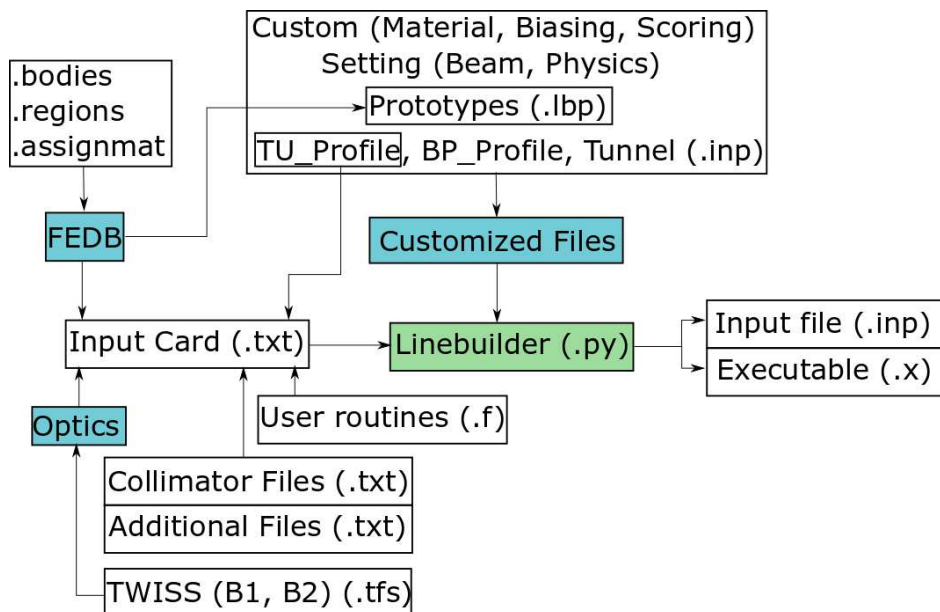

Figure 2.4.3: Diagram of the Linebuilder - folders are coloured in blue. The file endings of the custom and setting files are '.inp'.

Cluster

In case of CPU intensive simulations, they are not launched locally on the machine but on a dedicated cluster. The user can choose in which queue the simulation should be launched, depending on the length of the simulation. Each queue has a different maximum run-time and a different number of jobs that can be launched. In the case of this thesis for testing simulations the 'testing' queue was used, where a maximum number of ten jobs can be launched and the maximum run-time is two hours. For the actual simulations the 'normal' queue was used, with a maximum of 100 jobs and the run-time limited to 96 hours. Each job is launched to a different node that cannot be selected by the user.

For a simulation one should aim for a high number of primaries to achieve adequate statistics. The number of primaries is then launched split up to different jobs that run in parallel. Within those jobs, the primaries run in cycles. Thus, if a simulation is launched, the total number of primaries is calculated as:

$$\text{Total primaries} = \text{Number of jobs} \cdot \text{Number of cycles} \cdot \text{Number of primaries per cycle.}$$

To achieve meaningful results in this project, the number of total primaries should be of the order of several 10^4. Otherwise the statistical error is too high to make quantitative statements.

Even though post-processing is possible in FLAIR, it can be performed directly from the terminal as well. The script for post-processing can be launched even though not all the cycles have finished. This then will only post-process the finished cycles and allow a glance at the simulation results.

2.5 Simulation Settings

2.5.1 Thresholds and Biasing

In this project energy deposition in the experimental insertion of FCC-hh was studied. The source term of the simulation is a 100 TeV centre-of-mass proton-proton collision [6]. The particles produced in the collision are highly energetic and therefore generate dense particle showers. Tracking every single particle in a 700 m long line until it has deposited all its energy in the machine would be a huge computational effort. Thresholds have to be considered to absorb particles locally below a certain energy level that do not have a recognisable effect on the results and reduce the computational time. Furthermore, thresholds are necessary to only track the particles in an energy range where FLUKA can provide the correct physical models.

Thresholds can either be applied for the transport or for the production. The production threshold, as the name says, sets an explicit limit on the production of secondaries by electrons and positrons [40].

The first threshold that is used is impacting particles interacting electromagnetically that includes photons, electrons and positrons and is called EMFCUT. Usually this threshold is set to $500 \, \text{keV}$ for electrons and positrons, and $100 \, \text{keV}$ for photons. It is necessary to have a lower threshold for photons than for electrons and positrons, since photons are more penetrating at the same energy. For other particles PART-THR is used and set to $1 \, \text{keV}$. Only neutrons are left at their default value of 10^{-14}GeV [51].

In addition to the cutoffs, there is the possibility to apply biasing for certain particles, energies, regions, etc. Biasing is used to achieve a faster convergence of the data with the help of artificial probability distributions and is a powerful tool to reduce the CPU time per primary. Secondly, biasing techniques also can be used to reduce the variance of data and maintain the same CPU per primary. In this project, the first type of biasing was used. Since it is using an artificial probability distribution, this tool has to be handled with care, so that the results still represent the reality. A range of biasing techniques exist and are used.

For electromagnetically interacting particles there is the possibility of applying a leading particle bias (LPB) which reduces only the computation time. After each electromagnetic interaction, in which two particles are generally produced, only one of those two particles is randomly kept and its weight in terms of probability is adjusted. The more energetic particle is kept with higher probability, since it is more likely to propagate the shower.

Electromagnetic particles can undergo several physical mechanisms. By giving a number that is a power of two in the EMF-BIAS card, it is defined which mechanisms are taken in account [51]:

$$2^0 b_0 + 2^1 b_1 + 2^2 b_2 + 2^3 b_3 + 2^4 b_4 + 2^5 b_5 + 2^6 b_6 + 2^7 b_7 + 2^8 b_8 + 2^9 b_9 \qquad (2.5.1)$$

with the variables standing for different electromagnetic effects like bremsstrahlung, pair production, photoelectric effect and different scattering phenomena. For the LPB, a value of 1022 is selected, meaning the LPB is turned on for all the mechanisms mentioned above. In case this biasing is used, it is applied to all regions of the line.

It is possible to apply this biasing not to all particles but only particles below a certain energy level. In this project, particles that are below $1 \, \text{GeV}$ are biased, which was found to be a good balance between gaining CPU time and not losing critical information. The LBP leads to an increase in the fluctuations but since for energy deposition the expectation value is a point of interest, this is not problematic.

Furthermore, a so-called multiplicity bias is used in some simulations. In this biasing type just a certain percentage of the particles in a shower is kept and tracked. Following the central limit theorem, after a high number of simulated primaries, the tracked particles coming from showers will still represent the complete range of showers. For certain simulations multiplicity biasing was applied for hadrons and muons at a factor of either 20% or 40% for all regions of the line. Similarly to the EMF-BIAS this is used to reduce the CPU time, but it was not found as effective.

2.5.2 Scoring

In FLUKA scorings are used to perform 'measurements'. It can be selected which property should be measured, for example energy, dose or DPA. This is done with USRBIN cards. There is also the possibility to measure the spectra of particles at a boundary. In that case, a USRBDX card is used instead. For USRBINs the scoring can be done in a regular spatial mesh, independent of the geometry. Similarly, the size of the bins, also known as mesh, can be chosen freely. With larger bins the data converges quicker and the statistical error is smaller, while for smaller bins more precise results can be found with the disadvantage of higher statistical errors. Depending on the element, different forms of the mesh can be selected. In case of cylindrical elements, like the quadrupole magnets, a cylindrical mesh is chosen, while for rectangular elements, like the separation dipoles, a Cartesian mesh is chosen.

The investigated properties are absorbed power per metre, peak power density, integrated dose and DPA. For each of them, different meshes were selected, depending on their effect on the machine. In case of absorbed power per metre it is interesting to see how much power the whole magnet receives but not in a local spot, since the heat has to be transported from the whole magnet. So therefore the bins are relatively large, with slices of 10 cm in z direction and just one bin in the radial and angular distribution. For peak power density the critical problem is the quenching of the cold magnets. So first, investigations were focused on the cold elements. Furthermore, quenching is a local phenomenon so a finer mesh compared to absorbed power is required. In the longitudinal direction z, the bins have again a length of 10 cm. In the radial direction the radial average of the coil thickness is selected, that either leads to one or two bins in this direction. For the angular distribution 180 bins are selected. With these settings, the scoring reflects the width of the superconducting cables. The phenomena that are studied with integrated dose and DPA are highly localized effects. Therefore it is necessary to have a fine mesh, so localized peaks can be found. This is the reason why the integrated dose is the most challenging property for which to obtain good statistics. The dimensions of the mesh are 10 cm in the longitudinal direction z, 3 mm in the radial direction and 180 bins in the angular distribution. While the bins for absorbed power go over the whole area of the element, the mesh for peak power density, integrated dose, and DPA are only covering the radial area of the coils (Tab. 2.5.1).

	Mesh	Scoring	ΔR	$\Delta\Phi$	ΔZ
Absorbed Power	R-Phi-Z	Energy	Magnet Radius	360°	10 cm
Peak Power Density	R-Phi-Z	Energy	Coil Radius	2°	10 cm
Integrated Dose	R-Phi-Z	Dose	3 mm	2°	10 cm
DPA	R-Phi-Z	DPA	3 mm	2°	10 cm

Table 2.5.1: USRBIN Settings Cylindrical Elements.

2.5.3 Normalisation

The results from FLUKA are not obtained in the common SI units [51]. Thus, in case of measuring energy, the results are given in $\frac{\text{GeV}}{\text{cm}^3}$pp and for dose measurements in $\frac{\text{GeV}}{\text{g}}$pp, where pp means 'per primary'. These results must be converted to SI units. The three main properties that were investigated are the absorbed power per metre, the peak power

density and the integrated dose, which are measured in W/m, W/cm^3 and MGy, respectively. Depending on the quantity either the integrated luminosity of $30\,\mathrm{ab}^{-1}$ or the instantaneous luminosity of $30 \cdot 10^{34}\,\mathrm{cm}^{-2}\mathrm{s}^{-1}$ is used. Furthermore, the cross-section of a proton-proton collision at $50\,\mathrm{TeV}$ is assumed $\sigma = 108\,\mathrm{barn}$. The exact calculation can be found in Appendix A.

Chapter 3

Geometry Setup

This chapter describes the geometry setup used for the simulations of the high luminosity experimental insertion regions (IR), IR1 and IR5. The same geometry is considered for IR1 and IR5 at present. While the crossing angle is $100\,\mu$rad in both cases, the crossing anlge plane is vertical in IR1 and horizontal for IR5 [6]. The distance between the interaction point (IP) and the first quadrupole is $L^* = 40\,$m. The $700\,$m long Long Straight Section (LSS) (Fig. 3.0.1) is split into two parts that have different functions. The quadrupole triplet is located from $0\,$m to $490\,$m after the IP and then the matching section is located from $490\,$m to $700\,$m, starting with MCBDRH/V in Fig. 3.0.1. Further downstream there is the curved dispersion surpressor, which is not included in the scope of this work.
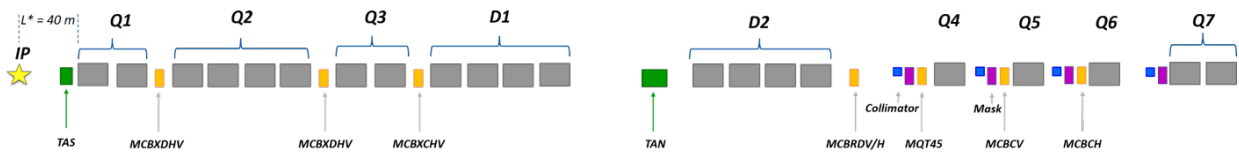
Figure 3.0.1: LSS Layout - Green: TAS, TAN; Grey: quadrupoles, dipoles; Yellow: correctors; Blue: collimators; Purple: masks.

3.1 Geometry: Triplet to TAN

This part of the line is the closest to the experiment. The quadrupoles in this section are used to focus the beam for collision. The separation dipoles, D1 and D2, are located further downstream and move the beams into two beam pipes. Additionally, absorber elements are found in this part of the line as well, catching a large amount of collision debris [52].

The closest element to the IP, $34\,$m downstream, is the Target Absorber Secondaries (TAS). As an absorber element close to the experiment, it catches a huge amount of collision debris, also known as secondaries, and protects the machine from fatal impact [52]. This highly impacted copper element has an aperture of $34\,$mm and an outer radius of $250\,$mm.

The TAS is followed by the quadrupole triplet, focusing the beam with superconducting magnets that have a gradient of $126\,$T/m (Q1), $101\,$T/m (Q2) and $100\,$T/m (Q3) [53]. Having one beam pipe for both beams, the aperture is $164\,$mm for Q1 and $210\,$mm for the modules of Q2 and Q3. These quadrupoles are split into submagnets, Q1 and Q3 into two magnets of $14.3\,$m of magnetic length and Q2 into four magnets of $12.5\,$m for manufacturing and transport

reasons. For protection measures a 35 mm tungsten alloy shielding, INERMET180[1] is applied as the innermost layer. Outside of the shielding the next layer is the cold bore and a thin layer of insulation. This is followed by a layer of liquid helium at 1.9 K used for cooling of the superconducting coils that make up the next layer. Two layers of superconducting Nb$_3$Sn coils are placed radially, separated by thin layers of insulator material, G11. Outside of the coils, there is one layer of aluminium, followed by the iron yoke. In this yoke there are four pipes for transporting the liquid helium at 4 K. A visualisation of the elements is given in Fig. 3.1.1.

(a) Cross Section: Triplet Quadrupole

(b) Cross Section: D1
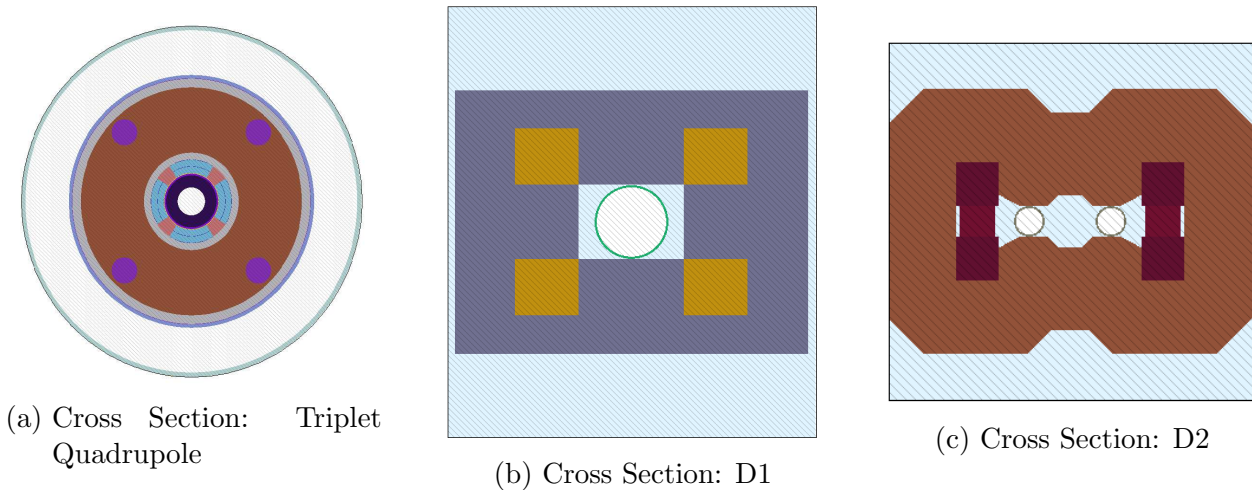
(c) Cross Section: D2

Figure 3.1.1: Cross sections of the magnets in the area of the triplet. The magnets are not scaled correctly in respect to each other.

Between Q1, Q2 and Q3 there are orbit correctors (C1-C3), responsible for the crossing angle of the beam at collision. The magnetic length is 1.3 m, the aperture is 210 mm and their field equals 0.5 T and 1.9 T, respectively [53].

Downstream of the triplet is the single bore beam separation dipole, D1. In this element the beams are deflected by the magnetic field to move apart from each other to eventually be located in two beam pipes further downstream. Similar to Q2, D1 is split into four magnets with a magnetic length of 11.3 m and a field of 2 T [53]. As warm magnets they are more tolerant for energy deposition compared to the quadrupole triplet. For protecting the coils from collision debris, they are placed as far away as possible from the beam, seen in yellow in Fig. 3.1.1.

Next is the TAN (Fig. 3.1.2), Target Absorber Neutrals, catching the neutral particles [52]. As those particles are not charged, they do not interact with the magnetic field of the quadrupoles and dipoles. Therefore they are neither focused in the triplet nor deflected in D1, so they move through the geometry without being disturbed. In the TAN those neutral particles are finally absorbed and do not go further into the accelerator. Being highly impacted, this element is warm. In this element the single beam pipe splits into two separate beam pipes, one for the incoming beam and one for the outgoing beam. Within a length of 5 m a beam separation of 104.2 mm is reached.

The last element before the matching section is the D2 (Fig. 3.1.1), the second beam separation dipole. It is used to deflect the diverging beams back into nearly parallel beams.

---

[1]INERMET180 is a tungsten alloy used for shielding elements.
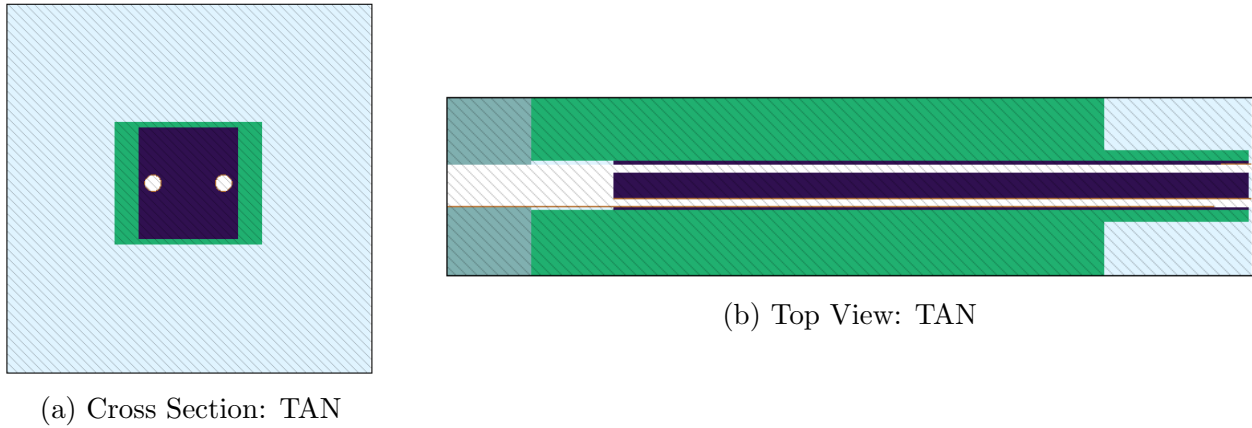
(a) Cross Section: TAN

(b) Top View: TAN

Figure 3.1.2: Cross sections and top views of the TAN. For the cross section the back end is displayed, where there are already two beam pipes. The two plots are not correctly scaled with each other.

For known reasons it is split into four magnets of 11.3 m. Each module has a different beam separation, finally reaching 250 mm. Similar to D1, the magnets of D2 are warm with a 2 T field.

3.2 Geometry: Matching Section

The matching section provides a smooth transition from the straight IR into the DS, so the optics of the beams are matched for the transition between these two regions. A set of four quadrupoles, Q4-Q7, with different lengths, apertures and strengths is used for this. All of the magnets have a beam separation of 250 mm (Fig. 3.2.1). Q4 has a magnetic length of 9.1 m, an aperture of 70 mm and a gradient of 144 T/m. Q5 and Q6 are both 12.8 m long with an aperture of 60 mm. They differ in both orientation of the aperture (Q5: vertical, Q6: horizontal) and gradient (Q5: 168 T/m, Q6: 127 T/m). Q7 then is split into two magnets of 14.3 m with an aperture of 50 mm and a gradient of 320 T/m [53]. The split of Q7 is needed to achieve the required focusing [54]. The further away from the IP a magnet is placed, the smaller the aperture.

In front of the matching section itself, there is a set of two correctors for closing the orbit and setting the beams into a parallel position with a beam separation of 250 mm. While MCBRDV is impacting in the vertical crossing scheme and MCBRDH is impacting in the horizontal crossing scheme. The magnetic length is 0.5 m and the field 1.5 T.

Since there is no shielding in the quadrupoles themselves, different strategies to reduce the impact of the collision debris are necessary [53]. With the collision debris mostly focused on the outgoing beam pipe, collimators (TCL) are placed on the outgoing beam pipe in front of the mask, corrector and quadrupole as protection elements. The size of the halfgap depends on the beta function at the longitudinal position of each collimator. Their active length is 1 m, similar to TCLs (Target Collimator Long) from LHC (Fig. 3.2.2).

The masks in front of each of the four quadrupoles Q4 to Q7 are a further protection element, covering both beam pipes (Fig. 3.2.1). In this project two different kinds of masks were tested, both made out of tungsten alloy (INERMET180). In the first case the length is 1 m
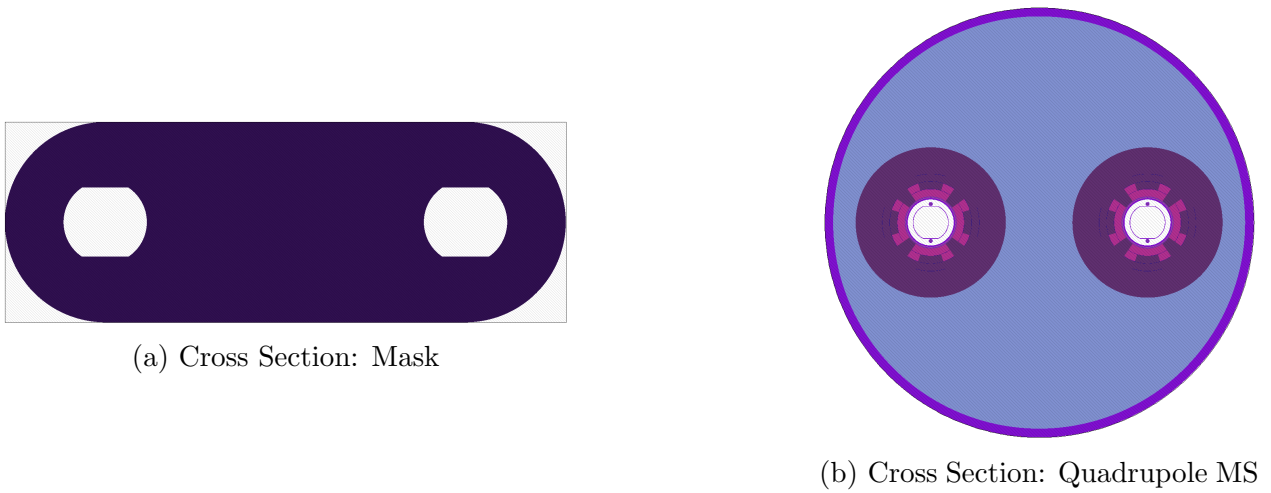
(a) Cross Section: Mask

(b) Cross Section: Quadrupole MS

Figure 3.2.1: Cross sections of quadrupoles and masks in the area of the matching section. The cross sections are not scaled correctly.

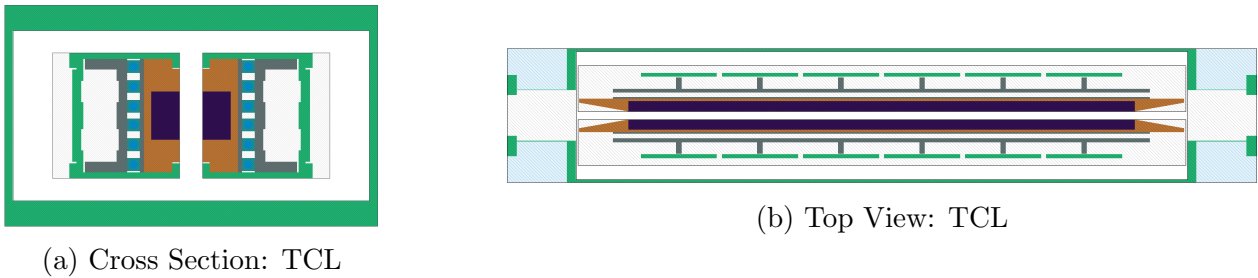

(a) Cross Section: TCL

(b) Top View: TCL

Figure 3.2.2: Cross sections and top views of the collimators (TCL) in the area of the matching section.

and the beam screens were circular with a radius overlapping the smallest circular radius of the magnet behind (Fig. 3.2.1) [55]. After the optimisation, the masks have a length of 2 m with rectellipse beam screens, perfectly overlapping with the beam screens in the next element.

To better control the beam orbit, correctors were placed between the mask sand the quadrupoles at Q4, Q5 and Q6. Their magnetic length is 1.6 m (MQT45) and 0.5 m (MCBCH, MCBCV) respectively. Since they catch a non-negligible amount of debris and therefore act as protection elements for the quadrupoles, they were added to the geometry, even though they are turned off and therefore do not have any optical impact for now.

Name	**L in** m	**A in** mm	**F in** T	**G in** T/m	**BS in** mm
TAS	3.0	34	-	-	-
Q1a, Q1b	14.3	164	-	126	-
Q2a - Q2d	12.5	210	-	101	-
Q3a, Q3b	14.3	210	-	100	-
C1 - C3	1.3	210	-	-	-
D1a - D1d	11.3	170	2.0	-	-
TAN	5.0	52	-	-	104.2
D2a - D2d	11.3	85	2.0	-	*
C4	3.0	70	1.5	-	250
TCL.4	1.48	8.1	-	-	-
Mask Q4	1.0	63	-	-	250
MQT_45	1.6	70	-	-	250
Q4	9.1	70	-	144	250
TCL.5	1.48	5.8	-	-	-
Mask Q5/6	1.0	53	-	-	250
MCBCH/V	0.5	60	-	-	250
TCL.6	1.48	1.9	-	-	-
Q5, Q6	12.8	60	-	168/127	250
TCL.7	1.48	1.3	-	-	-
Mask Q7	1.0	44	-	-	250
Q7a, Q7b	14.3	50	-	320	250

Table 3.2.1: Properties of the components in beamline in the final setup. (L...Length, A...Aperture, F...Field, G...Gradient, BS...Beam Separation). *: For each of the four modules of the D2 the beam separation is different since the beams are moving apart [53].

Chapter 4

Triplet

4.1 Particle Type Analysis

In this simulation, the debris of proton collisions is investigated. Per proton-proton collision at a centre-of-mass energy of 100 TeV, 197 particles are produced at the interaction point (IP). Moving away from the IP, the debris evolves because of decays which leads to 256 particles at 5 mm away from the IP. The majority of particles is given by photons (47%), produced in the decays of neutral pions (Fig. 4.1.1). The second most abundant particles are charged pions, that both equal roughly 18% of all the particles. The other particles are less dominant with percentages around 1%-3%. Only 11.2 particles per collision pass through the TAS with a slightly different particle distribution compared to the situation at the IP. The percentage of photons is slightly reduced to 42%, for the pions the numbers stay the same. However, the fraction of protons increases from 1.5% to nearly 7%.
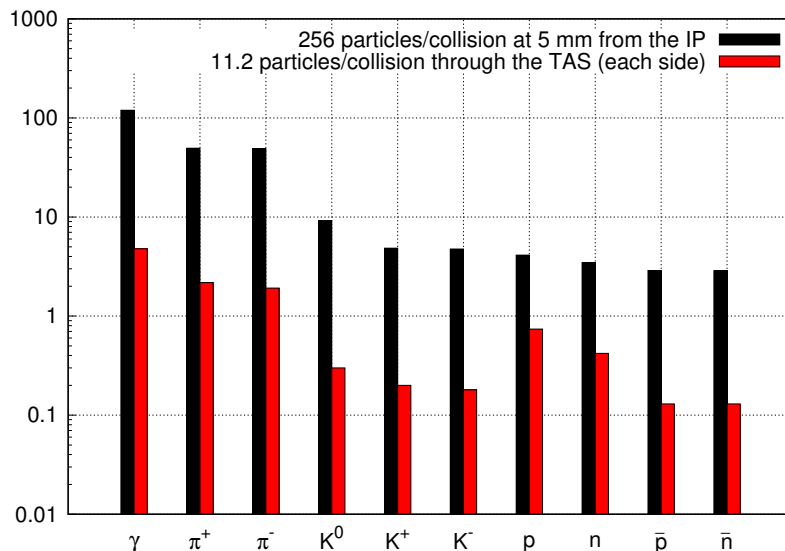
Figure 4.1.1: Particles from a proton-proton collision at a 100 TeV centre-of-mass energy. The black column represents the particles detected 5 mm after the IP, the red one the particles detected at the TAS 38 m after the IP. In case of HL-LHC only 155 particles are detected 5 mm from the IP and 6 particles at the TAS (20 m after the IP) [52]

.

The particles moving through the TAS will impact the accelerator elements further downstream. With only 11 particles per collision the number is quite small compared to the 256 particles that are present at 5 mm from the IP, but those particles are the most energetic ones [56].

Furthermore, an analysis of the evolution of the particle population was made. Scoring with USRBDX cards was introduced, to investigate the energy spectra in the different magnets, in particular Q1, Q2, Q3 and D1 [57].
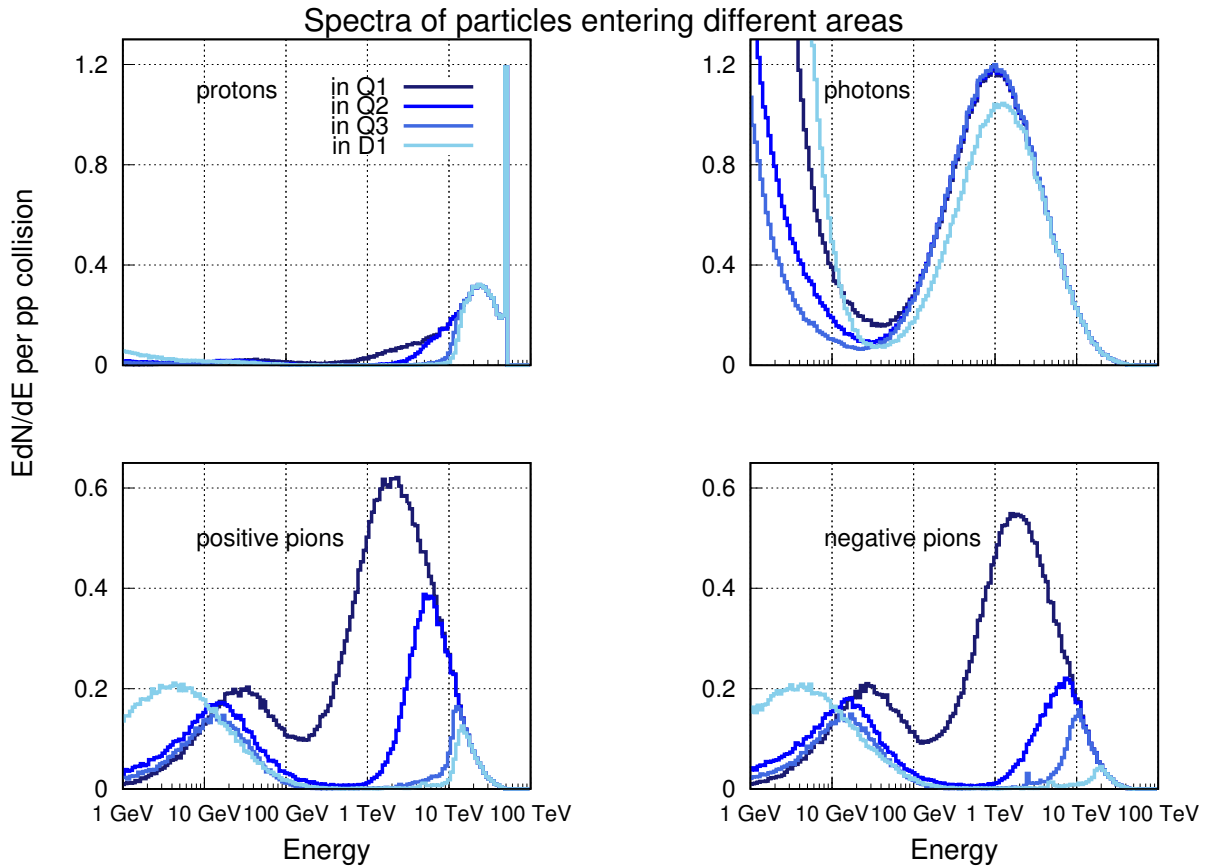
Figure 4.1.2: Spectra of particles entering into the different magnets of the triplet up to the D1 (horizontal crossing scheme). The y axis is given as $E \cdot \frac{dN}{dE}$, coming from: $\frac{dN}{d(logE)} = \frac{dN}{\frac{1}{E}dE} = E \cdot \frac{dN}{dE}$. The energy bins are split logarithmically from 0.0001 GeV to 100 000 GeV into 270 bins.

For protons, the peak is at 50 TeV in all magnets, which corresponds to protons produced in diffractive events (Fig. 4.1.2) [56]. These protons are not absorbed in the triplet and in the matching section, but they impact into the DS region further downstream. Photons peak at around 1 TeV and the population stays nearly constant over the triplet. The number of charged pions decreases significantly moving away from the interaction point. The highest peak occurs in Q1 around 1 TeV. The peak then decreases continuously for Q2, Q3 and D1 but it moves to higher energies, 10 TeV or more. Only the most energetic particles arrive at D1. This means that particles with lower energy are captured by the magnetic field of the quadrupoles and they are absorbed in the magnets. At the end of the matching section only protons are left over.

4.2 Energy Deposition: Crossing Angle Plane Comparison

The goal of this section is to give a complete picture of the energy deposition studies in the triplet, investigated for the vertical and the horizontal crossing angle scheme. In terms of feasibility of the cryogenics system the absorbed power per metre will be discussed. For protection of superconducting coils, the peak power density is studied, whereas for long term damage of the insulators, the integrated dose is investigated.

Absorbed Power per Metre

The absorbed power per metre is discussed first to asses the power load on the cryogenics system for all elements of the triplet. With the mesh described in Chapter 2.5, sufficient statistics were achieved. The TAS, just 35 m from the IP, is impacted the most in the triplet (Tab. 4.2, Fig. 4.2.1). Designed as an absorber element this was expected. The amount of absorbed power in the TAS is 26.5 kW for vertical and 26.8 kW for horizontal crossing. Taking the statistical error of $\leq 1\%$ in account, those two values are compatible. In the following quadrupole triplet Q1b in the vertical case is the most impacted module, with about 12.3 kW deposited on the tungsten shielding and 1.7 kW deposited on the cold mass itself.
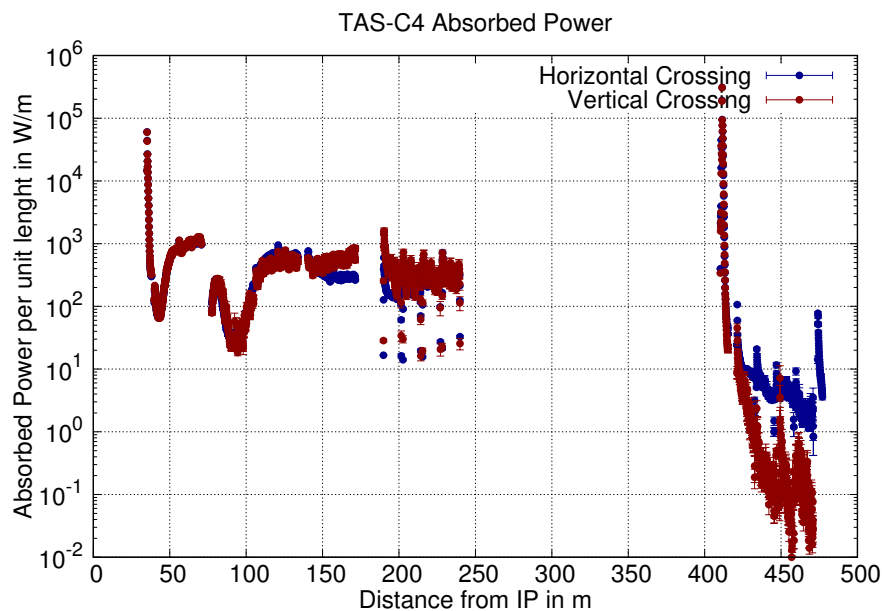
Figure 4.2.1: Absorbed power per metre as function of the distance from the IP including the area from the TAS to C4 for an ultimate instantaneous luminosity of $30 \cdot 10^{34} \, \mathrm{cm^{-2}s^{-1}}$

The vertical case for Q1b is worse than the horizontal case, because of the magnetic fields of the magnets. The quadrupole field of Q1 is focusing in the horizontal plane but defocusing in the vertical one. The similar situation of the magnetic field occurs in the magnets of Q3. For the modules of Q2, the magnetic field is focusing in the vertical plane and defocusing in the horizontal one. In case of vertical crossing, the beam is already moving towards the vertical

plane of the magnets. This effect is then amplified in Q1 with the magnetic field defocusing in the vertical plane. This leads to a high impact on Q1b.

The amount of power absorbed in Q1b is too high for the cryogenics system, to be guaranteed a safe and reliable heat transfer out of this magnet to keep it at the required temperature. Therefore mitigation strategies to reduce the heat load were studied and will be discussed in section 4.4 [58].

In kW	Horizontal		Vertical	
Element	CS	CM	CS	CM
Q1a	4.60 (±0.4%)	0.70 (±0.3%)	4.60 (±1.1%)	0.78 (±1.2%)
Q1b	12.3 (±0.4%)	1.69 (±0.3%)	13.0 (±1.0%)	1.92 (±0.8%)
C1	0.06 (±1.7%)	0.06 (±1.0%)	0.06 (±4.5%)	0.06 (±2.5%)
Q2a	1.47 (±1.2%)	0.20 (±0.9%)	1.53 (±3.2%)	0.32 (±2.7%)
Q2b	0.91 (±1.5%)	0.11 (±1.1%)	0.70 (±4.2%)	0.09 (±3.1%)
Q2c	6.30 (±0.7%)	0.83 (±0.5%)	4.60 (±2.1%)	0.63 (±1.5%)
Q2d	7.64 (±0.8%)	0.97 (±0.6%)	5.93 (±2.3%)	0.81 (±1.7%)
C2	0.71 (±2.0%)	0.08 (±2.2%)	0.51 (±5.1%)	0.05 (±4.5%)
Q3a	5.07 (±0.9%)	0.63 (±0.7%)	6.02 (±2.2%)	0.77 (±1.6%)
Q3b	3.97 (±1.1%)	0.41 (±0.9%)	7.80 (±2.3%)	0.95 (±1.7%)
C3	0.43 (±2.5%)	0.04 (±2.2%)	0.94 (±4.5%)	0.17 (±3.8%)

Table 4.2.1: Absorbed power per metre (1): CS...Cold Shielding, CM...Cold Mass

The results of the simulations were normalised with the instantaneous luminosity $30 \cdot 10^{34}\,\mathrm{cm^{-2}s^{-1}}$ and the area of the cross-section A in cm^2 by a factor $518.4 \cdot A$ to convert the results to W/m (see Appendix A).

In Q2 less power is absorbed in vertical crossing compared to horizontal crossing, because the magnetic field of the magnets is defocusing in the horizontal plane and focusing in the vertical one. So this means that the horizontal crossing angle gets amplified and the magnets are impacted more in this case. For Q3, vertical crossing impacts the modules more than horizontal crossing instead. This is caused by the magnetic field which focuses the beam in the horizontal plane and defocuses it in the vertical plane.

In kW	Horizontal	Vertical
Element	WM	WM
D1a	2.0 (±0.9%)	4.99 (±1.7%)
D1b	2.1 (±1.0%)	3.57 (±2.0%)
D1c	2.7 (±0.9%)	3.57 (±2.1%)
D1d	3.8 (±0.7%)	3.96 (±2.1%)
TAN	110 (±0.2%)	107 (±0.6%)
D2a	0.14 (±2.1%)	0.07 (±10.7%)
D2b	0.06 (±3.2%)	0.01 (±18.5%)
D2c	0.05 (±5.0%)	0.003 (±13.9%)
D2d	0.03 (±6.0%)	0.003 (±14.5%)

Table 4.2.2: Absorbed power per metre (2): WM...Warm Mass

The first separation dipole D1 absorbs more power in the vertical crossing case, while in D2

the modules are significantly more impacted in the horizontal crossing. Since the separation dipoles are warm magnets, the values are acceptable [53].

Similar to the TAS, the TAN absorbs more power compared to the magnets. Absorbing $>100\,\mathrm{kW}$, this is the most impacted element in IR1 as well as IR5, corresponding to vertical and horizontal crossing scheme.

Peak Power Density

Investigating the peak power density, the focus is on the superconducting areas of the cool magnets. Therefore an analysis for the quadrupoles of the triplet will be given. The absorber elements TAS and TAN and the two separation dipoles are not in the centre of interest, since they are warm magnets. For the peak power density a quench limit of $5\,\frac{\mathrm{mW}}{\mathrm{cm^3}}$ is assumed [6]. This should be seen as a tight design limit, since the hard limit will be probably higher. Above the quench limit, superconductivity breaks down and leads to several problems, discussed in section 2.2.2. The mesh for the scoring is selected so the peak power density is averaged over the cable thickness (see Chapter 2.5). In case of peak power density the ultimate instantaneous luminosity of $30 \cdot 10^{34}\,\mathrm{cm^{-2}s^{-1}}$ is used [6].

In Q1 peak power density is higher in the vertical crossing scheme case (Fig. 4.2.2), caused by the magnetic field as explained previously. The highest value is obtained in Q1b, similar to the situation for absorbed power per metre, however, the design limit of $5\,\frac{\mathrm{mW}}{\mathrm{cm^3}}$ is hardly exceeded. For Q2 the situation is worse for horizontal crossing, but the peak at $3\,\frac{\mathrm{mW}}{\mathrm{cm^3}}$ is below the design limit. Having turned the magnetic field around again, vertical crossing is worse in Q3, but the maximum lays around $3\,\frac{\mathrm{mW}}{\mathrm{cm^3}}$.

Therefore it can be concluded, that the $35\,\mathrm{mm}$ of tungsten shielding is sufficient enough in terms of protection against quenches for vertical crossing as well as for the horizontal case.
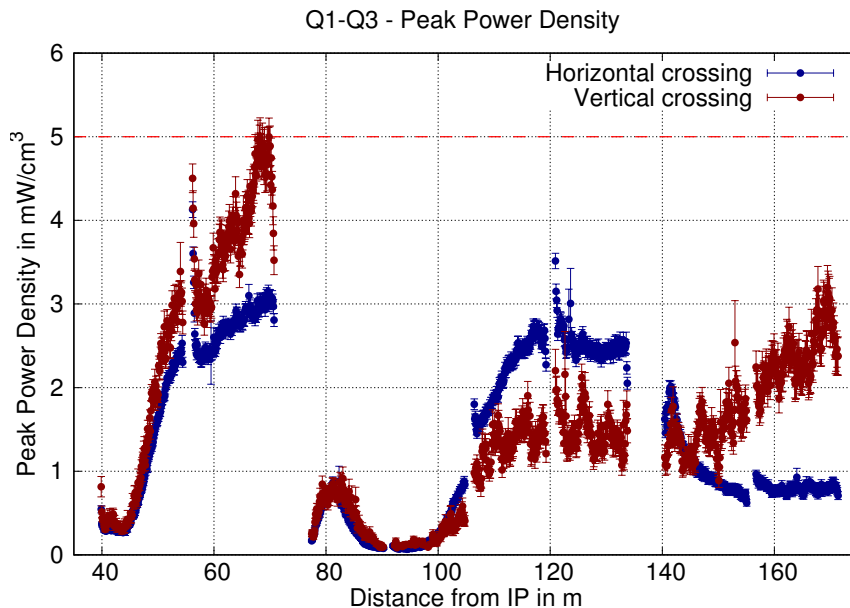

Figure 4.2.2: Peak power density in triplet as function of the distance from the IP with the ultimate instantaneous luminosity of $30 \cdot 10^{34}\,\mathrm{cm^{-2}s^{-1}}$.

Integrated Dose

To prevent insulator material to suffer from severe long term damage, the integrated dose should not exceed a certain limit. Otherwise the material degenerates and loses its properties (see Chapter 2.2.2). The design limit is tightly set at 30 MGy, but it is expected that it will rise to about 60 MGy to 100 MGy [6] [59]. Compared to the two properties discussed before, the integrated dose is still the most challenging one.

In Q1b a maximum value of 80 MGy is reached in case of vertical crossing (Fig. 4.2.3), with an highly localized maximum in the vertical plane (Fig. 4.4.1). For horizontal crossing the maximum in Q1b is around 47 MGy, clearly above the design limit as well. The difference between the two cases is caused by the quadrupole field in Q1 that is focusing in the horizontal plane but defocusing in the horizontal plane. For the modules of Q2 and Q3 the values are lower than in Q1. In Q2 the integrated dose is expected to exceed the design limit for horizontal crossing and in Q3 for vertical crossing by around 20 MGy.
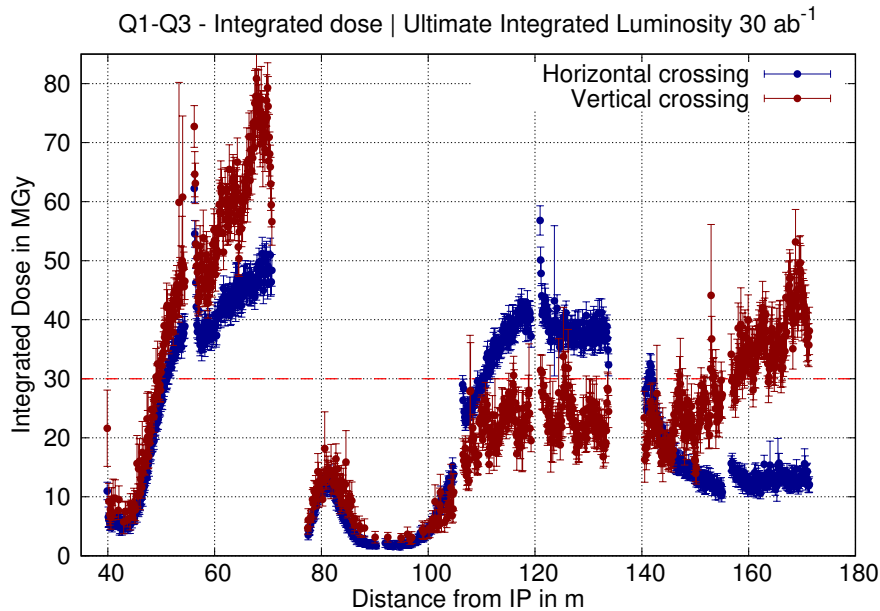
Figure 4.2.3: Integrated dose in triplet: data with an statistical error ≤35% are displayed at an ultimate integrated luminosity of $30\,\mathrm{ab}^{-1}$).

Mitigation strategies to improve this situation will be presented in section 4.4 (Fig. 4.4.1).

4.3 DPA Simulation

The irradiation of superconductors leads to displacement of atoms which changes the material critical properties (see Chapter 2.2.2). Therefore this physical quantity is studied for the cold quadrupole magnets of the triplet. Compared to the peak power density or the integrated dose, thicker shielding in the magnet is not effective in reducing the DPA [60].

The current simulation with $L^* = 40\,\mathrm{m}$ and a shielding of 35 mm is compared with two former simulations with an $L^* = 45\,\mathrm{m}$ and a shielding of 15 mm and 55 mm respectively [60]. For a more straight forward comparison of the result, the results of the previous simulations are

shifted 5 m closer to the IP, so the data sets are overlapping in the longitudinal direction. In Fig. 4.3.1 the comparison between the DPA distribution in Q1, depending on the shielding thickness, is shown.
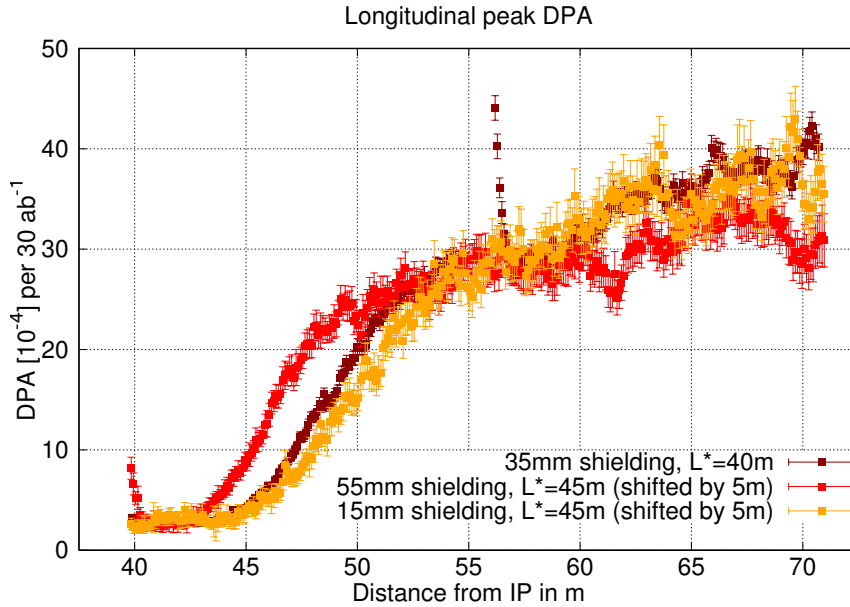

Figure 4.3.1: DPA for different shielding thickness.

Focus for this simulation lies in Q1, that was originally not split, but a unique 30 m long magnet. The split appears just in the current simulation.

For the first half of Q1, the highest DPA is observed for the 55 mm case. The lowest DPA is obtained in the simulation with 15 mm shielding. The reasoning behind this is that the thinner the shielding, the larger the aperture, so less particles are intercepted by the material.

A peak of $45 \cdot 10^{-4}$ DPA per $30 \, \text{ab}^{-1}$, is observed at the entrance of Q1b because of the presence of the interconnect. This peak does not appear in the simulations, where Q1 is continuous. In the second half of Q1 and Q1b respectively, the highest DPA is equally observed in the simulation with 35 mm and 15 mm. In general the results for the DPA are acceptable [29].

Particles	15mm	35mm	55mm
Protons	1.5	0.6	0.4
Neutrons	78	96.1	91.5
Ions	19	2.5	8
Electrons	1	0.1	0.1
Pions	-	0.2	-
Total	**88.5**	**99.5**	**100**

Table 4.3.1: Particle distribution in % for DPA. The values for the 35 mm shielding simulation are calculated with a new routine and therefore vary slightly from the older simulations [60].

The majority of DPA is caused by neutrons. Since they are neutral particles they are not intercept by the tungsten shielding and lead to DPA on the superconducting material. Electromagnetic particles like electrons and protons are absorbed in the shielding and hardly cause any DPA in the superconducting coils anymore [61].

4.4 Mitigation Strategies

Mitigation strategies are needed, to reduce integrated dose in the triplet and absorbed power in Q1b.

4.4.1 Combination of Crossing Schemes

The idea of this section is to provide a method to achieve a homogeneous distribution of the dose over the cross-section of the magnet. So far the azimuthal position of the peaks is strongly localized (Fig. 4.4.1) either on the vertical or horizontal plane, depending on the crossing angle and on the magnet. The values can be mitigated by changing and combining the crossing angle plane scheme and the angle polarity for vertical crossing [57] [62]. Eventually this leads to a lower integrated dose for the magnet and therefore a longer lifespan.
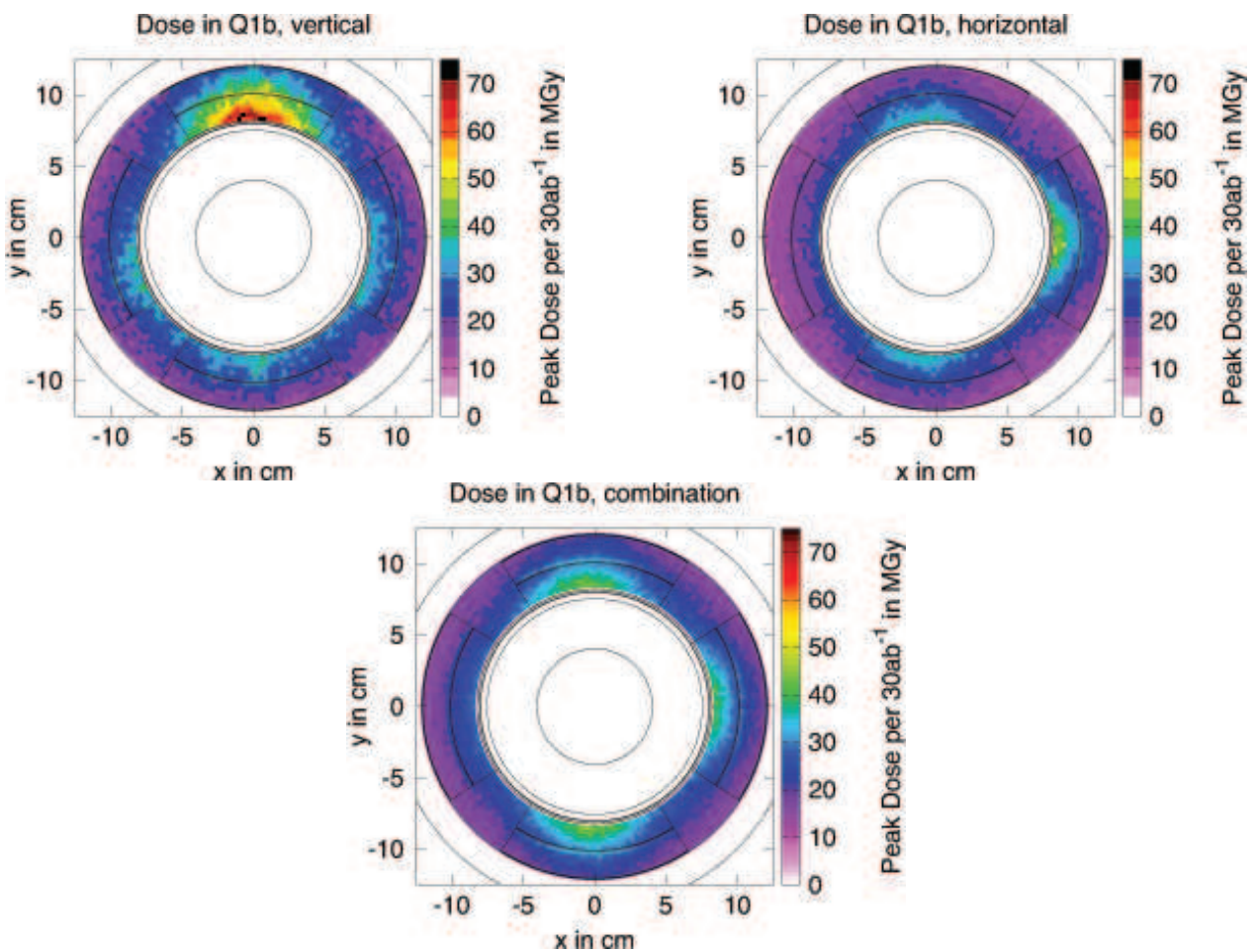
Figure 4.4.1: Comparison of crossing schemes in 2D: vertical, horizontal and combined crossing scheme.

For vertical crossing a maximum in Q1b of nearly 80 MGy is reached, that is highly localized in the vertical plane (Fig. 4.4.2). In case of horizontal crossing the maximum lays around 50 MGy, but with the maximum in the horizontal plane. Using the combination leads to a maximum of around 45 MGy, much closer to the current design limit of 30 MGy, but well distributed over the magnet (Fig. 4.4.1). Using the combination of crossing scheme, in Q1a the majority of the magnet faces an integrated dose below the critical value and the maximum is at around 34 MGy. So the hard limit is exceeded for Q1a in the combination of crossing schemes, but those values are acceptable, if the limit rises up to 60 MGy (see Chapter 2.2.2).
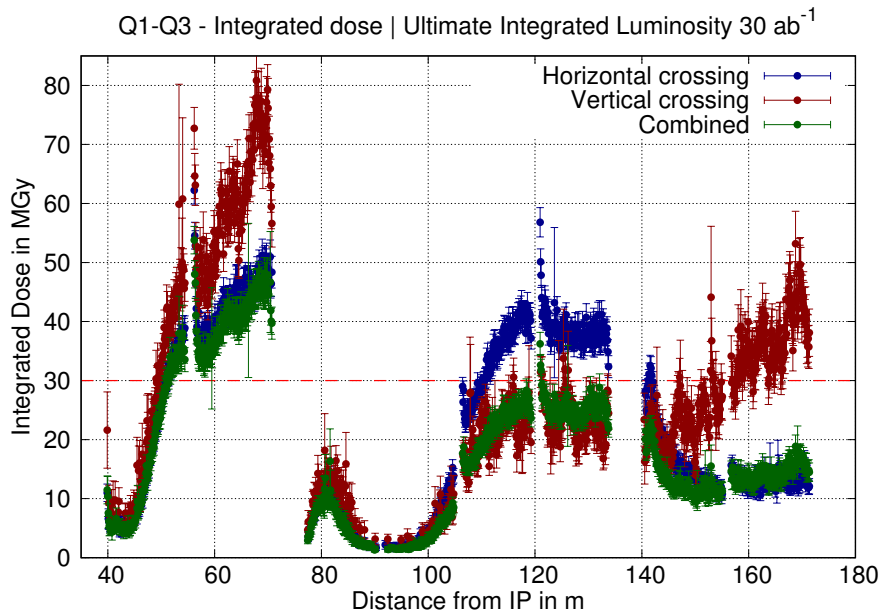
Figure 4.4.2: Combined integrated dose in the triplet as a function of the distance from the IP for pure h-crossing, pure v-crossing and a combined crossing scheme (50% horizontal, 25% vertical up, 25% vertical down) for an integrated luminosity of $30\,\text{ab}^{-1}$.

For all the following magnets in the triplet, the integrated dose stays below the design limit of 30 MGy in case of the combination of the crossing angle schemes. While a maximum of 60 MGy is Q2 is reached for horizontal crossing, a reduction of a factor 2 could be achieved. Similarly a reduction by a factor 3 could be gained for the integrated dose in Q3.

4.4.2 Split of Q1b

Absorbing nearly 15 kW in Q1b in case of vertical crossing, whereas 13 kW are absorbed by the cold shielding, leads to problems for the cryogenics system to safely transfer the heat [58]. In terms of heat transfer shorter magnets are preferred by the cryogenics system [63]. Furthermore, the observed dose in Q1b exceeds the limit and the maximum of DPA is located in this magnet as well.

Since there is some margin for the absorbed power per metre in Q1a in terms of heat transfer, it is acceptable if this magnet absorbs more power. Following changes were made (Tab. 4.4.1): Q1b was split into two magnets, Q1b and Q1c, of 7.15 m magnetic length, whereas Q1a stayed the same length. The goal was to reduce in this way the absorbed power in Q1b by half. The aperture in Q1a was closed by 14 mm, so this magnet would catch more. In Q1b and

Q1c the aperture opened to 180 mm and 190 mm respectively [64]. This change in aperture also led to a change in the gradient of the magnets. At the same time the magnets received a thicker shielding, which helps in term of integrated dose but not necessarily for DPA (see section 4.3).

	L in m		**A in** mm		**S in** mm		**G in** Tm	
	old	**new**	**old**	**new**	**old**	**new**	**old**	**new**
Q1a	14.3	14.3	164	150	35	38	126	139
Q1b	14.3	7.15	164	180	35	47	126	119
Q1c	-	7.15	-	190	-	47	-	111

Table 4.4.1: Mitigation strategy for Q1b (L...Magnetic length, A...Aperture, S...Shielding, G...Gradient) [64]

The absorbed power per metre is significantly reduced. The increase in Q1a is due to the smaller aperture that now catches more debris. For the former Q1b magnet a reduction of 50% could not be achieved, but according to the cryogenics team those values are manageable [58].

In kW	**Q1b long**	**Q1b split**
Q1a		1.0
Q1b	2.0	0.7
Q1c		0.6

Table 4.4.2: Absorbed power per metre in kW on cold mass: Total: 2.8 kW (Q1b long), 2.3 kW (Q1b split).

With opening the aperture, the peak appearing at the front face of Q1b disappeared. Even lower values could be achieved for the front face of Q1c. The average values in Q1b and Q1c are similar to the ones from the original magnet (Fig. 4.4.3).
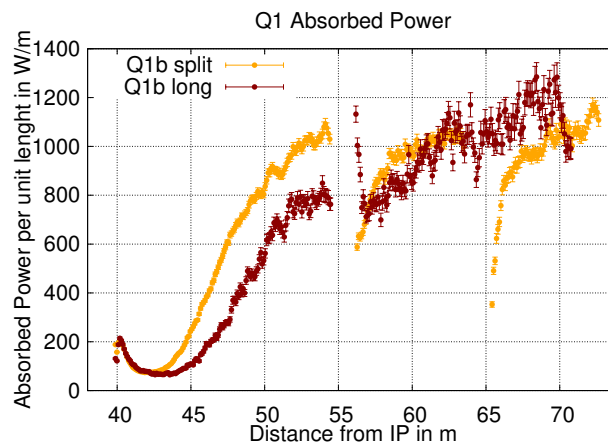
Figure 4.4.3: Absorbed power per metre for Q1b split at an ultimate instantaneous luminosity of $30 \cdot 10^{34}\,\mathrm{cm}^{-2}\mathrm{s}^{-1}$.

The splitting of Q1b has a beneficial effect on integrated dose and peak power density as well (Fig. 4.4.4). For peak power density even more margin is now achieved, with the maximum

of around $3.5 \frac{\text{mW}}{\text{cm}^3}$ in Q1a and $2.5 \frac{\text{mW}}{\text{cm}^3}$ in Q1b and Q1c. The peak power density in Q1b is reduced by a factor of 2, while the increase of peak power density in Q1a is negligible. In case of integrated dose a slightly higher dose in Q1a is observed than in the original state, caused by the smaller aperture. For Q1b and Q1c now the limit of $30\,\text{MGy}$ is hardly exceeded. These improvements in Q1b/c were achieved with introducing the larger aperture and thicker shielding, compared to the original situation. With the opening of the aperture, the peaks on the front face disappeared as well.
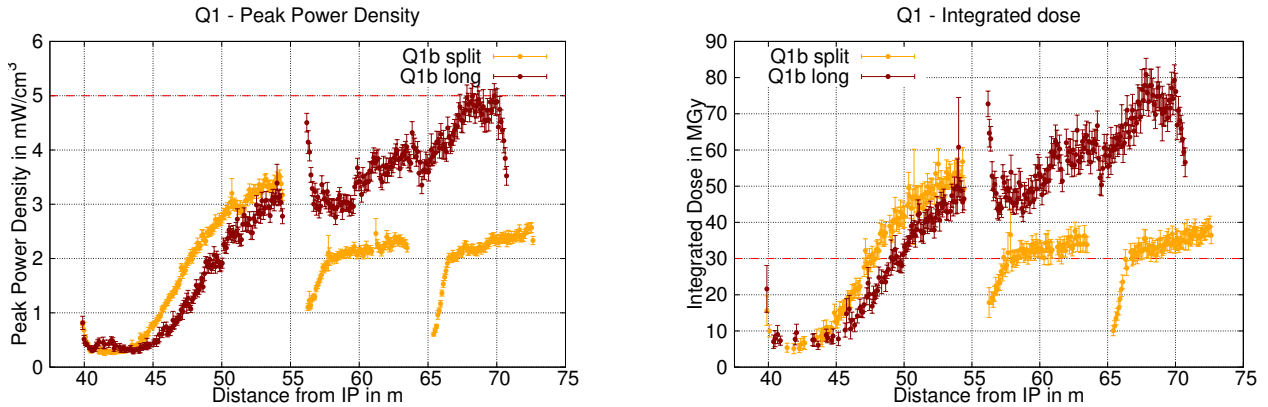
Figure 4.4.4: Peak power density at an ultimate instantaneous luminosity of $30 \cdot 10^{34}\,\text{cm}^{-2}\text{s}^{-1}$. Integrated dose at an ultimate integrated luminosity of $30\,\text{ab}^{-1}$.

The DPA values in Q1a increased significantly, because the shielding increase is not beneficial for neutrons, but it remains lower than the maximum of the previous configuration. The peak at the front face of Q1b disappears thanks to the larger aperture. The DPA in Q1b and Q1c is much lower than in the original case [61].
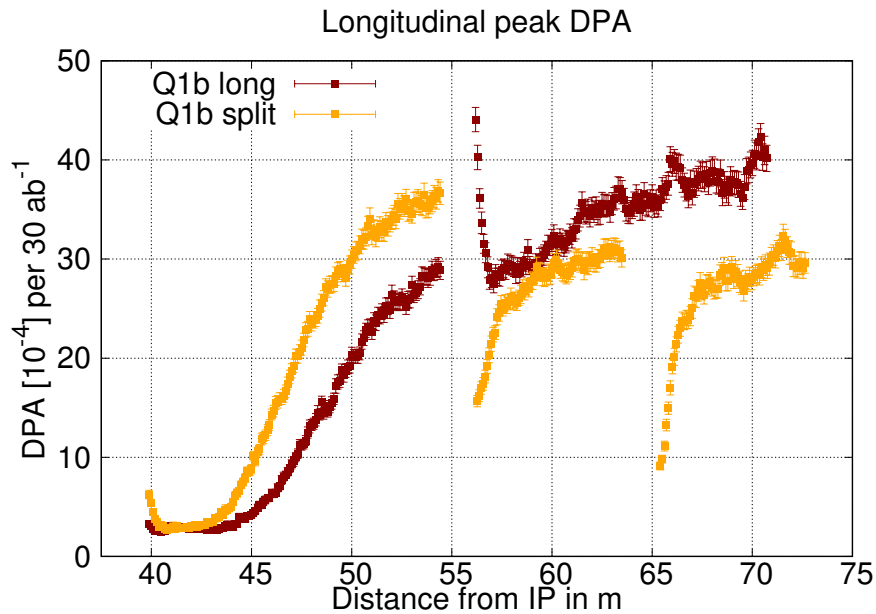
Figure 4.4.5: DPA for Q1b split.

Even though the simulation for the integrated dose and for the DPA have the same mesh, the

obtained statistics are worse in the case of integrated dose. The reason for this can be found in the tungsten shielding. While DPA is mainly caused by neutrons, the biggest contribution for the integrated dose are electromagnetic particles. These electromagnetic particles are then caught in the shielding while neutrons move through it, without interacting. Therefore higher statistics are achieved for DPA in respect to the integrated dose.

4.5 Outlook

4.5.1 Combination of splitting and crossing schemes

So far the crossing angle combination was done with a crossing angle of 50% horizontal, 25% vertical up and 25% vertical down [62]. Up to now, it was assumed that it was necessary to run one experimental insertion in horizontal crossing plane and the other one in the vertical plane. Studies have shown that this is not necessary and any arbitrary combinations of crossing plane angles can be chosen [65] [66]. In future it is also possible to combine the planes in any arbitrary way and find the most effective solution.

A quick check showed that the original distribution is already close to the optimum (Fig. 4.5.1).
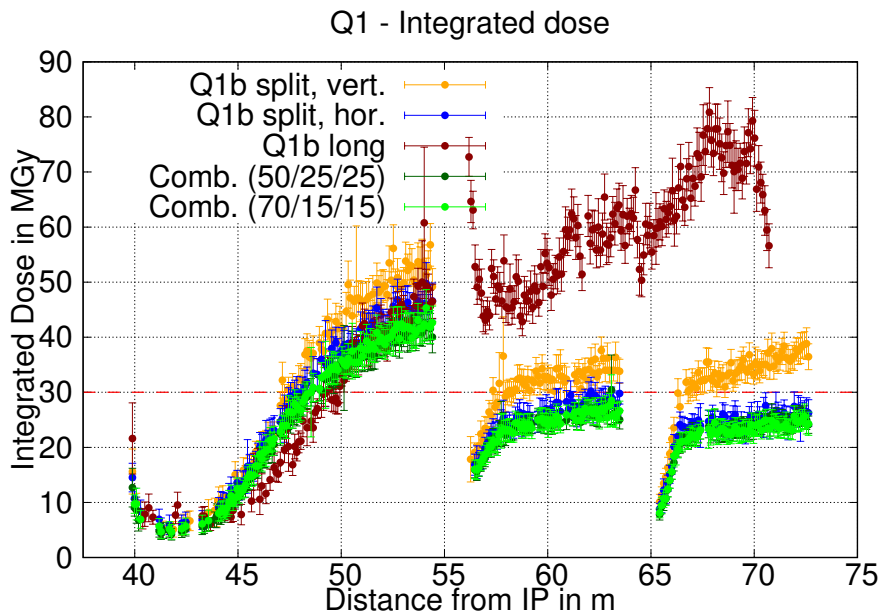
Figure 4.5.1: Integrated dose for the Q1b split and the combination of crossing angle planes at an ultimate integrated luminosity of $30\,\mathrm{ab}^{-1}$.

4.5.2 Conclusion

The situation in the triplet is now well understood and below the critical values for most of the magnets. The concerned mitigation strategies, splitting the magnet or use a combination of crossing angle polarity and plane combinations, proved to be very effective.

With the combination of the split in Q1b and the mixing of the crossing angle planes a reduction of integrated dose of more than 50 MGy in Q1b and Q1c below the design limit could be achieved. Now the maximum of around 40 MGy occurs in Q1a. Taking in account that the limit should rise to at least 60 MGy this value should be manageable.

Furthermore, there is also the option of splitting Q1 into three magnets of the same length, instead of keeping Q1a the same length and splitting Q1b into two parts can be investigated [64].

Chapter 5

Matching Section

The goal of this chapter is to give a complete picture of the energy deposition in the matching section that extends from 490 m to 700 m after the IP. Absorbed power per metre, peak power density and integrated dose were studied for the horizontal as well as for the vertical crossing scheme.

Up to this point simulations were done for this part of the line, but the statistics that could be produced were not sufficient despite the use of different biasing techniques. Therefore no quantitative predictions could be made for the matching section [55]. The reason for the lack of the statistics was the high CPU time per primary. So in the first section a method is discussed to significantly reduce the CPU time. This type of approach was not necessary for the same areas in LHC or HL-LHC, since the energies are much lower and the geometries smaller. Eventually quantitatively reliable results for energy deposition in the matching section are produced that are then discussed in the second part of this chapter.

5.1 Two-step Simulation

In this section a way of improving the statistics for computing intensive simulations is discussed and studied. Simulations for IR1 and IR5 are covering a range of 700 m and are performed at a centre of mass energy of 50 TeV. This leads to large particle showers and therefore a CPU time around 1 h per primary if the whole line is simulated at the same time with the standard scoring for energy deposition. Thus, it is hardly possible to perform simulations in a suitable time range that would lead to acceptable statistical errors in the elements of the matching section. To achieve acceptable statistics, the goal was to simulate at least 40000 primaries within 4 full days (see Chapter 2.5).

5.1.1 Simulation Settings and Goal

The idea behind this strategy is to split the simulations in two parts. In the first part, the line is simulated with high thresholds from the IPA to 490 m downstream, where the surviving particles are dumped on a plane. It is possible to have such high thresholds since the particles with a lower energy would not propagate into the area of the matching section but be absorbed in one of the elements in the triplet. The thresholds are modified using EMFCUT and PART-THR cards in FLUKA (see Chapter 2.5). The EMFCUT impacts particles that are interacting electromagnetically, like photons, electrons and positrons, while the PART-THR then is applied to all the other particles. If particles have an energy lower

than the given threshold they are absorbed locally and they are not further transported. Due to this feature no meaningful results are produced in the area of the triplet.

In this first step the CPU time per primary is maximum 10 s and around 830000 primaries were launched. The dumped particles are then used as a source term in the second step when they move on into the matching section and deposit energy in the elements. The second step is then the actual energy deposition simulation for the matching section, as it is known from the studies in the area of the triplet. Whereas in the first step no scorings are applied, since the results would be meaningless, the standard USRBINs for absorbed power per metre, peak power density and integrated dose are applied in the second step.

5.1.2 First Step - Vertical Crossing versus Horizontal Crossing

In this section the first step for vertical crossing as well as for horizontal crossing is discussed and a characterisation of the particles impacting in the matching section is given. With this type of simulation being new, different values for thresholds (EMFCUT, PART-THR) were tested in the first place, 1 GeV, 10 GeV and 500 GeV. The higher the threshold is, the more particles are absorbed in the triplet, which leads to a lower CPU time on the one hand but to a higher loss of information on the other hand. It was found that the thresholds set at 500 GeV do not impact quality of the energy deposition studies in the matching section significantly. With the threshold at 500 GeV the amount of events dumped at the plane 490 m after the IP, was lower by a factor of 2.5 with respect to the threshold set at 1 GeV. With the CPU time of 1 s per primary being lower by a factor of 15 compared to the 1 GeV simulation, it was decided to proceed with the threshold at 500 GeV.

If a particle is not dumped it is always connected to an event from where this particle comes from. One event can produce several particles that are dumped at the plane. The lower the threshold, the bigger the ratio between the number of particles and events that hit the plane. At higher thresholds particles are absorbed earlier and just high energetic particles reach the plane. So the ratio between the number of particles and number of events being dumped is getting smaller. 830 000 primaries were launched for vertical crossing as well as for horizontal crossing with the thresholds at 500 GeV. In case of vertical crossing around 150 000 particles were dumped at the plane, corresponding to nearly as many events. For the horizontal crossing scheme 200 000 particles were dumped. The number is slightly higher than for vertical crossing, because the TAN is less effective in this case (see Chapter 3.1). In the TAN the beam pipes are diverging in the horizontal plane, so the collision debris that has a crossing angle in the horizontal plane has more chances to go through the bore without interaction.

First the distribution of different particle types was investigated and it is discussed in the following. In the triplet the dominant particles are pions produced in proton decays (see Fig. 4.1.1). Going further downstream, the particle distribution changes, ending up with just protons in the dispersion supressor. In the matching section protons (Particle ID: 1) and photons (Particle ID: 7) are the most dominant particles (see Fig. 5.1.1) for vertical as well as horizontal crossing. Other non negligible contribution is due to electrons (Particle ID: 2), pions (Particle ID: 13, 14), neutrons (Particle ID: 8), anti-neutrons (Particle ID: 9), muons (Particle ID: 10, 11) and kaons (Particle ID: 24, 25). As mentioned before, the higher amount of particles per collision in the horizontal case is caused by the TAN, that is more efficient in the vertical crossing case. In both crossing schemes the majority of protons is

produced in the collision itself, while other particle types are produced in the interaction of collision debris particles with the material of accelerator components or from decays.
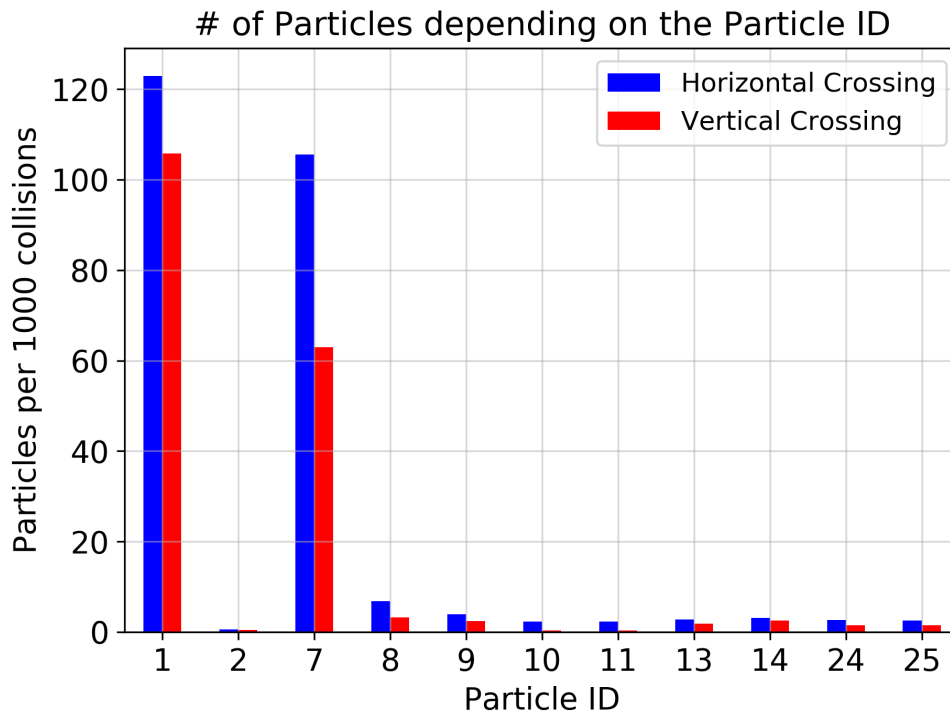

Figure 5.1.1: Particle ID Distribution - Comparison of horizontal and vertical crossing scheme: Protons and photons make up the majority of particles at the plane, while the other particles are less dominant. The particle IDs can be found in Appendix B.

In terms of energy distribution, the largest amount of protons has an energy very close to 50 TeV while photons are less energetic. As it can be seen in Fig. 5.1.2 and Fig. 5.1.3, the spectra for the photons decreases exponentially for higher energies. Protons with high energies will move through the matching section and will end up in the DS, while the lower energetic particles like photons are absorbed at some point in the matching section. Therefore the DS is then dominated by protons. Comparing the two crossing schemes, no differences in terms of energy distribution can be seen, as expected.

For a better understanding of the nature of the particles hitting the plane, the xy- distribution of the particles was studied as well. The majority of protons is located in the right beam pipe, the outgoing beam pipe, even though the collision debris is simulated and not the beam itself. Since protons are charged particles, they are bent by the magnets. Depending on the energy of the particle, they are located in different positions of the beam pipe. Particles with higher energies have a higher rigidity, meaning they have a lower bending angle. While low energy particles that have a lower rigidity are bent stronger (see Eq. 2.1.2). The lower the energy of the proton is, the larger offset to the right side of the centre of the beam (Fig. 5.1.4). The same effect is seen with positively charged particles, like positrons or kaons. Negatively charged particles are deflected to the left side.
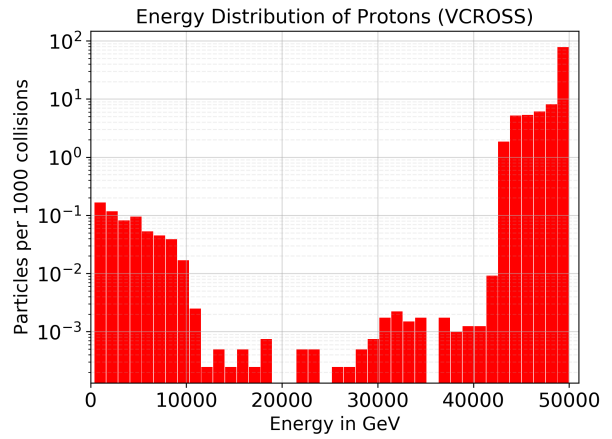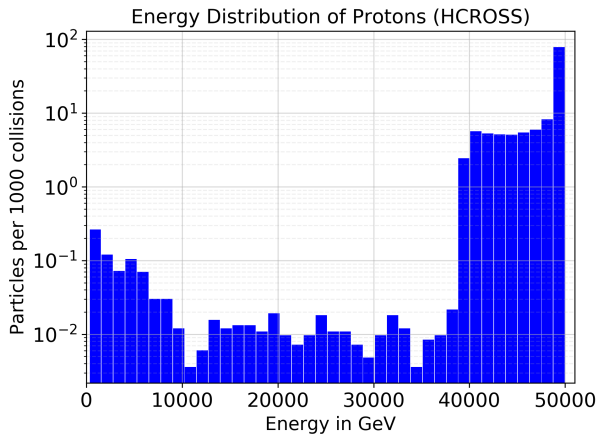
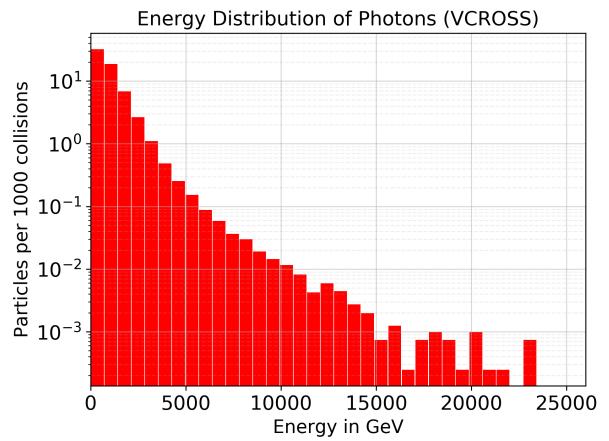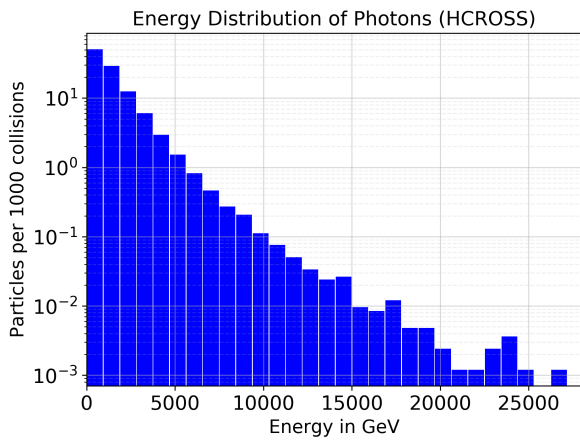Figure 5.1.2: Energy Distribution Comparison (Protons).

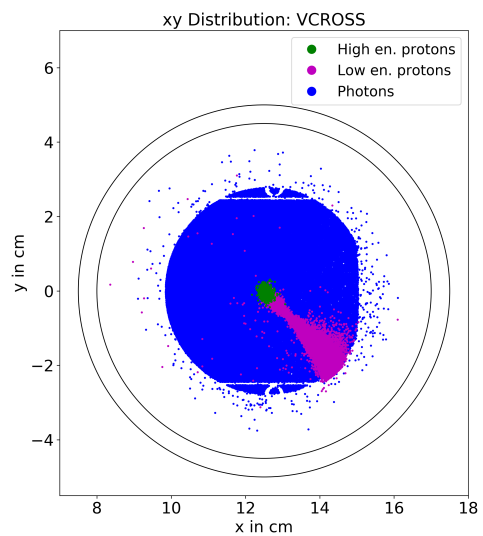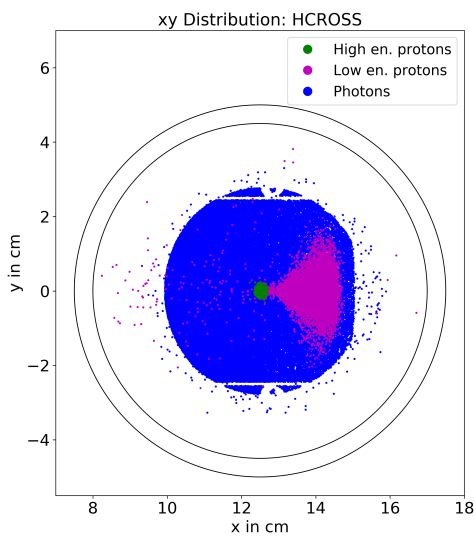Figure 5.1.3: Energy Distribution Comparison (Photons).

Figure 5.1.4: XY-distribution in both crossing schemes: High energy protons: >49.5 TeV, low energy protons: <49.5 TeV.

For the two crossing schemes the xy-distribution of protons is slightly different. While protons are located in a line from the centre of the right beam pipe to the right bottom in the vertical case, they are spread over a wider area in the horizontal case, caused by the plane of crossing.

Photons, as well as neutrons and anti-neutrons, move equally through both beam pipes. As they are neutral particles, they are not affected by the magnetic field of the magnets and so in vacuum, they move straight in a certain angle from where they were produced. This is also valid for neutral kaons. For the horizontal crossing scheme, are shifted slightly to the right side, caused by the crossing angle in the horizontal plane compared to the vertical crossing angle.

The situation is different for muons because they are more penetrating and they are not absorbed by the elements in the line. Therefore they do not impact the plane only in the spot of one of the beam pipes.

5.1.3 Second step

The goal of the second step is to investigate the energy deposition in the matching section. In the second step the normalisation (see Appendix A) has an additional factor of $\frac{\text{Number of events dumped on the plane}}{\text{Number of launched primaries}}$ on the standard normalisation, because one has to take in account that just a fraction of the launched primaries has reached the plane and was dumped [67].

The particles dumped in the first step were loaded as a source term in the second step. For keeping the randomness, it is important that the number of primaries which are launched in the second step is lower than the number of events recorded in the first step. Otherwise some events are taken twice, which leads to biased results, as discussed in chapter 2.3.

In the second step the EMFCUT and the PART-THR were set to the standard values of 500 keV for electrons and positrons, 100 keV for photons and 1 keV for the rest of the particles (see 2.5). In case of neutrons the default value of $10 \cdot 10^{-14}$ GeV is selected. Even though the particles were loaded from the plane at 490 m, right in front of the matching section, the computing time still can be optimised using biasing techniques. Therefore some tests with the multiplicity bias and the leading particle bias (EMF-Bias, see chapter 2.5) were done. Eventually the situation was optimised to a CPU time per primary of 1 min by applying the EMF-BIAS at 1 GeV. The results of these simulations are discussed in the following sections.

5.2 Energy Deposition: Crossing Angle Plane Comparison

In this section the energy deposition for vertical crossing scheme and horizontal crossing scheme will be discussed in the same manner as in the chapter about the triplet.

Energy deposition studies were already performed in this part of the line for the EuroCirCol 2018[1] but with no protection elements. This led to unacceptable high values, especially in

---

[1]EuroCirCol – The European Circular Energy-Frontier Collider Study: 4th Meeting (Karlsruhe 2018): https://indico.cern.ch/event/733292/

Q5 and Q7b. In Q5 up to 2000 MGy in terms of integrated dose were reached, without any protection elements [53]. Mitigation strategies were concerned, adding masks and collimators to the line. Furthermore, correction magnets were included in the FLUKA simulation. Even though they have no impact on the optics, because they are turned off, they have a positive impact on the collision debris of the quadrupole magnets behind [55]. With the statistical errors too high in the matching section, no quantitative statements could be given. The new approach of splitting up the simulation into two steps, leads to a lower CPU time per primary and therefore more particles could be launched and better statistics are observed. All the presented results were done with the latest design of the masks.

5.2.1 Protection Devices and Mask Optimisation

As a first protection element, collimators were added to the matching section after the Eu-roCirCol2018. The TCL (Target Collimator Long) LHC model was adapted to the FCC requirements. The length stayed the same, only the material of the jaw needed to be changed from copper to Inermet180, the tungsten alloy. The position of the collimators was chosen arbitrarily 1.5 m in front of the quadrupoles of the matching section on the outgoing beam pipe, since there were no space constraints [55]. The half gap for the collimators was set to 15σ for the collimators in front of Q4, Q5 and Q6 and 30σ for the collimator in front of Q7. Those settings would be similar to the one of HL-LHC [52]. For calculating the half gap of the collimator, the relation $\sigma = \sqrt{\beta_x \cdot \varepsilon}$ (see chapter 2.1.3) was used. The normalised emittance is $4.128 \cdot 10^{-11}$ m [6] and β_x was found plotting in the TWISS file, plotting z versus β_x.

Adding the collimators led to improvements in absorbed power up to a factor of 10 in Q5. Studies were performed for the inner beam pipe as well but no improvement of the situation was achieved there, since the collimator is placed on the outer beam pipe. So in the next step masks were introduced and the correctors, that were already in the TWISS file were added to the FLUKA geometry [55].

The masks had a length of 1 m, a rectellipse shape and cylindrical beam screens. By adding those masks, the collimators had to be shifted again an the halfgap had to be recalculated (Tab. 5.2.1). With this set-up, the situation further improved. In terms of absorbed power a factor of two to three could be gained for the different quadrupoles. For the integrated dose a reduction of up to a factor ten was achieved with this technique, but the dose was still at a level up to 200 MGy. Therefore further mitigation strategies had to be considered.

Name	L in m	S in m	Halfgap in cm
TCL.A4R	1.0	498.8	0.81
TCL.B4R	1.0	554.0	0.58
TCL.C4R	1.0	617.3	0.19
TCL.D4R	1.0	665.0	0.13

Table 5.2.1: Final collimator settings: L...Magnetic length, S...Distance from IP.

Since there is sufficient space, it was possible to modify and optimise the masks. The opti-mised design has a length of 2 m and the same shape, but the beam screen is now rectellipse, perfectly overlapping with the beam screen of the following magnet downstream. In both

cases they are made out of INERMET180. Even though the masks were elongated in z, the centre of the mask stayed at the same s position.
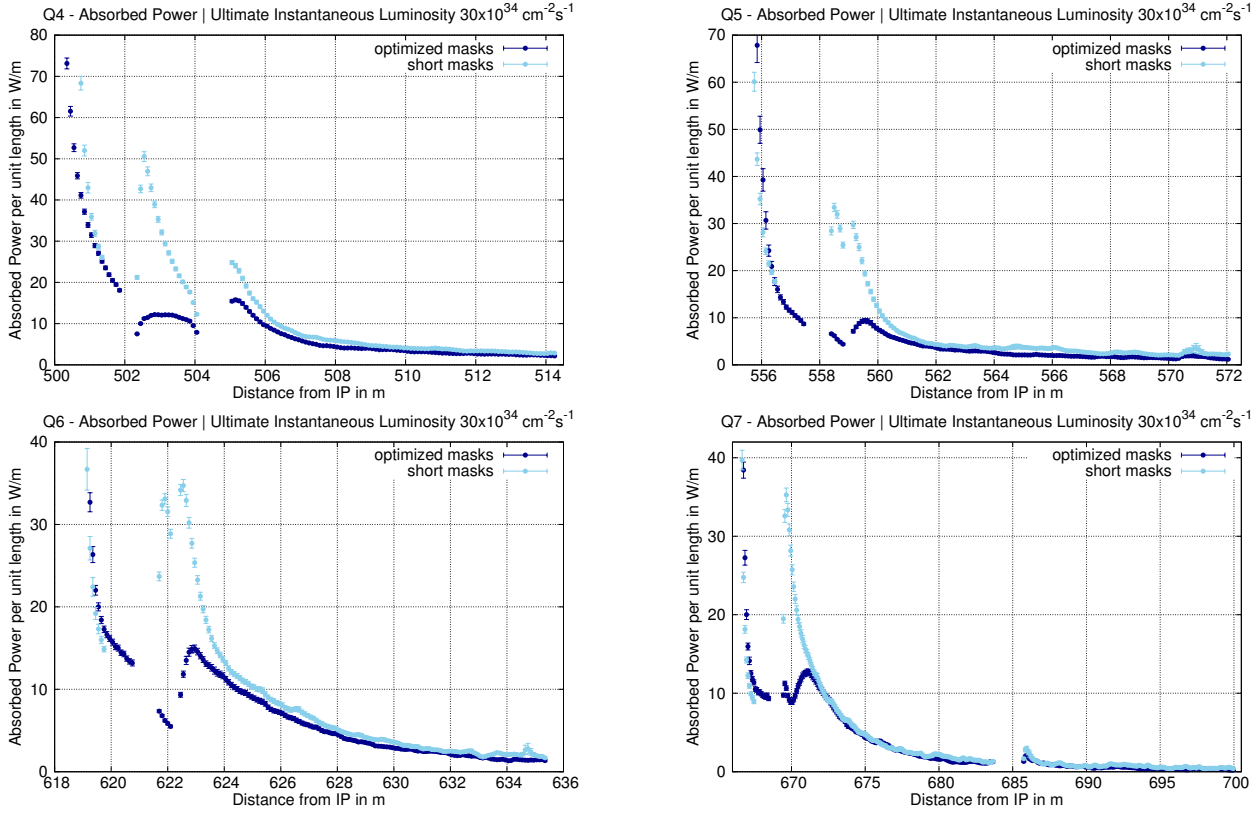

Figure 5.2.1: Absorbed power per metre for different the mask designs in horizontal crossing at an ultimate instantaneous luminosity of $30 \cdot 10^{34}\,\mathrm{cm^{-2}s^{-1}}$.

The improved mask design reduces the absorbed power in the correctors MQT_45, MCBCH and MCBCV. Depending on the corrector, the absorbed power is lower by a factor 3 to 5 compared to the short mask. The absorbed power in the front face of the quadrupoles is reduced significantly. In Fig. 5.2.1 a reduction of absorbed power by at least a factor three can be seen in Q5, Q6 and Q7a. For the body of the magnets there are no significant changes, as expected. Since the situation improved significantly with the optimised masks, the further sections are discussed for the set-up with the long masks.

5.2.2 Energy Deposition Studies

Absorbed Power per Metre

The most impacted elements in the final simulations in terms of absorbed power per metre are the collimators, absorbing 1 kW-2 kW, and the masks, absorbing 0.06 kW-0.1 kW (Tab. 5.2.2). Both types of elements are warm, so these amounts of power is manageable to absor, comparing to the results in the triplet. The cold quadrupoles absorb up to 75 W. In total, 2 kW more power is absorbed in the horizontal case, mostly absorbed in the collimators. This is caused by the position of the jaws, that set 'boundaries' in the horizontal plane but are open in the vertical one. Therefore more debris is caught in the horizontal crossing angle scheme. Otherwise no big differences between vertical and horizontal crossing could be observed.

In kW	Horizontal		Vertical	
Element	CM	BID	CM	BID
TCL.4	-	4.62 ($\pm$0.9%)	-	2.89 ($\pm$1.0%)
Mask Q4	-	0.15 ($\pm$1.4%)	-	0.15 ($\pm$1.5%)
MQT45	0.02 ($\pm$0.8%)	-	0.019 ($\pm$0.7%)	-
Q4	0.045 ($\pm$0.7%)	-	0.057 ($\pm$0.8%)	-
TCL.5	-	1.10 ($\pm$2.0%)	-	1.02 ($\pm$1.7%)
Mask Q5	-	1.11 ($\pm$2.5%)	-	1.16 ($\pm$1.8%)
MCBCH	0.002 ($\pm$1.6%)	-	0.002 ($\pm$1.3%)	-
Q5	0.038 ($\pm$1.2%)	-	0.035 ($\pm$0.9%)	-
TCL.6	-	2.20 ($\pm$1.5%)	-	1.89 ($\pm$1.2%)
Mask Q6	-	0.07 ($\pm$1.8%)	-	0.087 ($\pm$2.3%)
MCBCV	0.003 ($\pm$1.3%)	-	0.003 ($\pm$1.0%)	-
Q6	0.067 ($\pm$0.9%)	-	0.064 ($\pm$0.7%)	-
TCL.7	-	1.33 ($\pm$1.9%)	-	1.17 ($\pm$1.7%)
Mask Q7	-	0.05 ($\pm$2.2%)	-	0.062 ($\pm$2.5%)
Q7a	0.069 ($\pm$1.2%)	-	0.063 ($\pm$1.1%)	-
Q7b	0.008 ($\pm$2.9%)	-	0.007 ($\pm$2.4%)	-

Table 5.2.2: Absorbed power per metre: CM...Cold Mass, BID...Beam Interception Device; Total power deposition: 10 kW (Horizontal), 8 kW (Vertical).

The highest impact on the quadrupoles is on the front face of the magnets (see Fig. 5.2.2). Using the most recent version of the masks, the absorbed power on the correctors reduced drastically.

Peak Power Density

For the peak power density the values are mostly below the design limit of $5 \frac{\text{mW}}{\text{cm}^3}$, except for Q7a where it reaches $8 \frac{\text{mW}}{\text{cm}^3}$, as it can be seen in Fig. 5.2.3. Calculating the peak power for the fine mesh with a radial binning of 3 mm instead of the cable thickness (see chapter 2.5), this leads to values below the limit of $20 \frac{\text{mW}}{\text{cm}^3}$ [68].
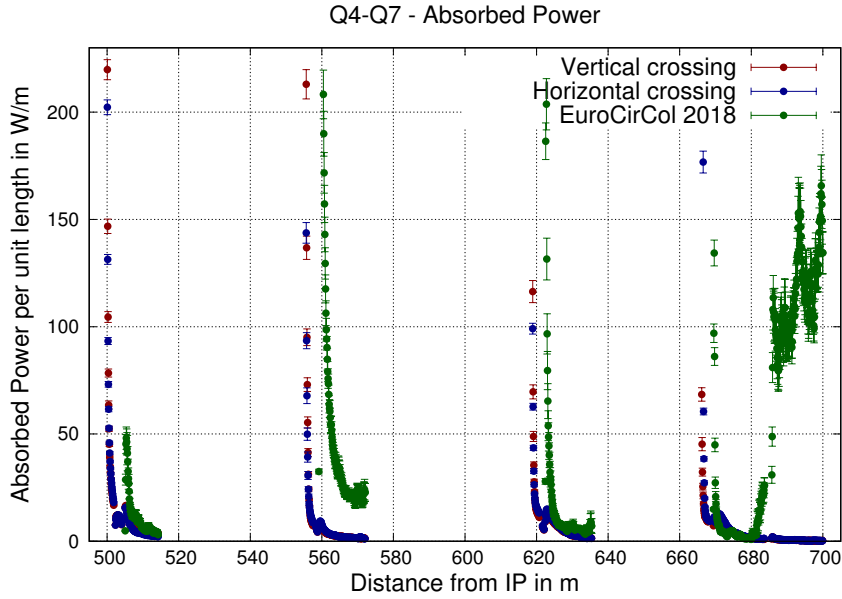
Figure 5.2.2: Absorbed power per metre in the matching section at an ultimate instantaneous luminosity of $30 \cdot 10^{34}\,\mathrm{cm}^{-2}\mathrm{s}^{-1}$. Comparison between horizontal and vertical crossing scheme. As a reference to the situation before protection elements were added, the results presented at the EuroCirCol2018 [53] are added as well.
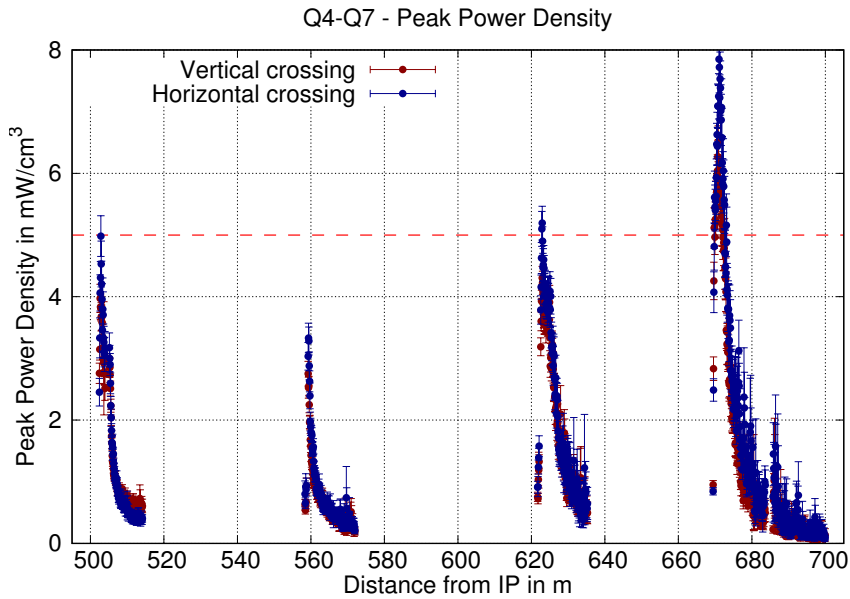

Figure 5.2.3: Peak power density in the matching section at an ultimate instantaneous luminosity of $30 \cdot 10^{34}\,\mathrm{cm}^{-2}\mathrm{s}^{-1}$. Comparison between horizontal and vertical crossing scheme.

Integrated Dose

The values of the integrated dose remain challenging. For each quadrupole the design limit of $30\,\mathrm{MGy}$ is exceeded, as well as for the corrector in front of Q4, MQT_45.

61

Assuming, that the design limit is set really tight and it would rise to around 100 MGy in future, the situation for Q4 to Q6 would not be critical anymore. In general, the values remain below 100 MGy (see Fig. 5.2.4), apart from some crucial locations, the front face of Q6 and Q7. If the dose limit will be increased to 100 MGy as expected, the values in all of Q4, Q5 and most of Q6 and Q7b would be acceptable.

For Q7a the integrated dose reaches a level of 180 MGy, unacceptable even with a 100 MGy limit. It was found that this high dose is caused by a shower that is produced in the collimator when high energetic particles hit the jaw. So far the half gap equals 30σ or 1.3 mm.

With already several steps set-up optimisation, including introducing the collimators and masks, the improvement the design of the masks and including the correctors from the TWISS file, a different approach, like opening the jaw of the TCL in front of Q7, has to be taken. It is assumed that high energetic particles of the collision debris interact with the material of the jaw and produce a shower there. This shower deposits energy then in Q7a. Therefore the idea is to open the half gap, so particles pass without any interaction and no shower is produced.
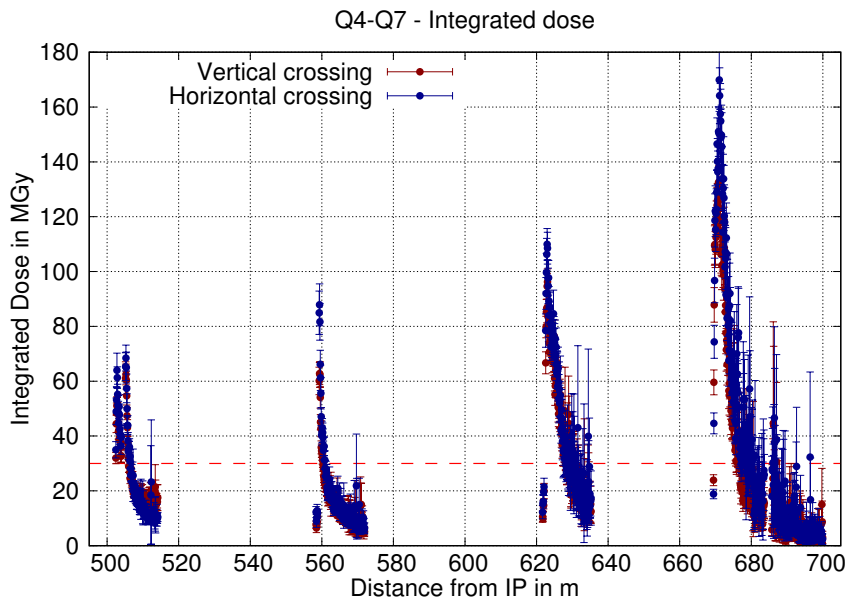

Figure 5.2.4: Integrated dose in the matching section at am ultimate integrated luminosity 30 ab^{-1}.

With the jaws opened at 1 cm the absorbed power in Q7a changes (Fig. 5.2.5). The absorbed power increases from 7 W/m to above 15 W/m at the front face of Q7a. While it then further increases with the collimator closed, the absorbed power is immediately lowered if the half gap is open at 1 cm. In total, the quadrupole magnet Q7a absorbs less power if the collimator in front of it has a larger half gap.
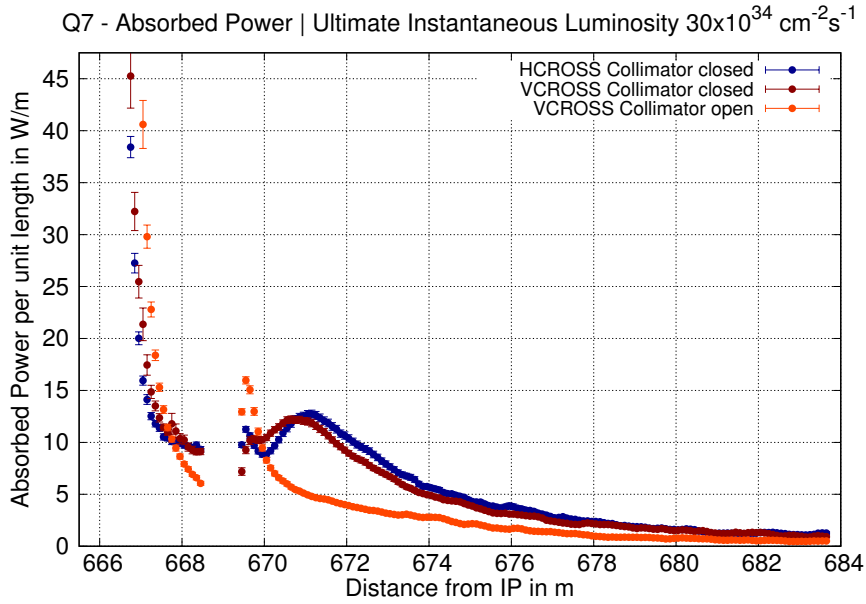
Figure 5.2.5: Opening of the half gap in Q7: Absorbed Power

Opening the half gap to 1 cm reduces the dose in Q7 significantly as well (Fig. 5.2.6). While the values on the first bins of the magnets stay the same at around 120 MGy, it is immediately reduced to 40 MGy in the case of the opening of the jaw while for the old case the dose then increased further to 140 Mgy and then reduces much later in the collimator. With opening the jaw, all the simulation results for peak power density are below the limit of $5\,\mathrm{mW/cm^3}$ (Fig. 5.2.6).
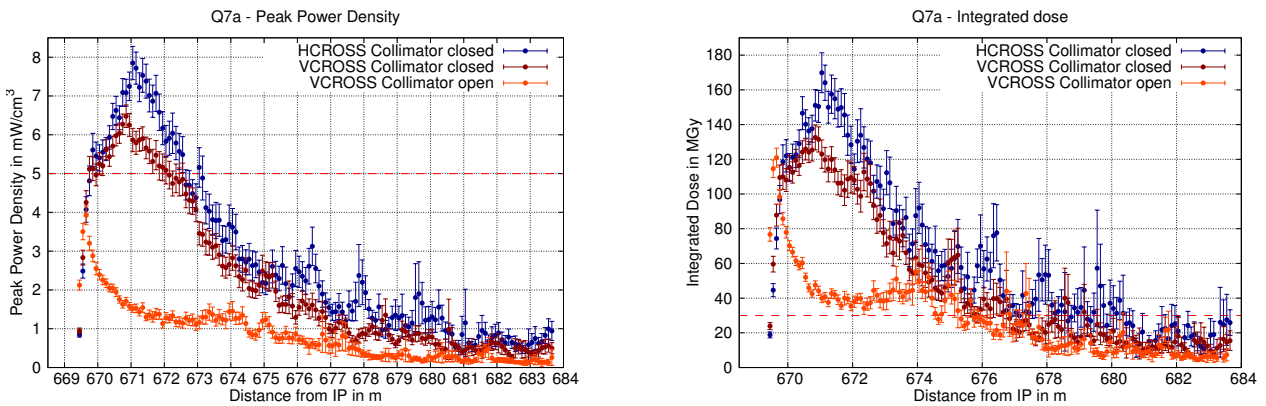
Figure 5.2.6: Opening of the half gap in Q7: peak power density and integrated dose at an ultimate instantaneous luminosity of $30 \cdot 10^{34}\,\mathrm{cm^{-2}s^{-1}}$ and an ultimate integrated luminosity of $30\,\mathrm{ab^{-1}}$.

Additionally, the effect of changing the collimator position can be studied. It should be investigated if those particles, not caught in the collimator, then would cause problems downstream in the DS. Up to now there is no shielding included in the matching section. It would be an option to introduce shielding in Q7 to protect the coils and insulator material. However, the highest dose is mainly focused at the front of Q7a and then quickly decreases. Therefore, a shielding in this magnet would not be too effective.

While changing of the crossing angle plane was an effective measurement to reduce the dose in the triplet, this would not improve the situation substantially here, since the dose is already well distributed over the whole face of Q7a [55].

The simulations were done for the ultimate integrate luminosity of $30\,\text{ab}^{-1}$. If it was possible to change Q7a once during the lifetime, the integrated dose would be reduced to maximum $90\,\text{MGy}$. This is really expensive though and should be avoided if possible.

Chapter 6

Conclusion

Energy deposition studies are crucial for the development of new machines like FCC-hh. The centre-of-mass energy of 100 TeV in the interaction point leads to very energetic collision debris that then impacts the elements of the accelerator. This leads to damages of the magnets and machine failures and therefore should be avoided. The investigated quantities were absorbed power, peak power density, DPA and integrated dose. These are related to the heat load in the element, quenching of the superconducting magnets and deterioration of superconducting and organic materials like insulators.

In the triplet, energy deposition has been studied in terms of absorbed power to assess the load on the cryogenics system, of peak power density to evaluate the risk of quenching and of accumulated dose and DPA to estimate the long term damage to insulating and superconducting materials. Both crossing schemes have been considered. The absorbed power on the quadrupole Q1b is 12.3 kW, too high for the cryogenics system. The integrated dose going up to 80 MGy exceeds the limit by 50 MGy. Therefore mitigation strategies were implemented, including the splitting of Q1b into two magnets of the same length, opening its aperture and adding more shielding. Additionally the crossing schemes were combined. With those measures, the values for absorbed power, peak power density, DPA and integrated dose are now below the critical values for each element of the triplet. By splitting Q1b the absorbed power on the cold mass of Q1b was reduced now to 0.7 kW on Q1b and 0.6 kW on Q1c to compared 2.0 kW on Q1b before. The maximum in peak power density now can be found in Q1a with $3\,\mathrm{mW/cm^3}$. With the help of combining the crossing schemes and splitting Q1b, the maximum of the integrated dose can be found in Q1a at around 40 MGy. Assuming that the limit rises to 100 MGy, this is a safe value. These mitigation strategies also led to a reduction of the DPA to a maximum of around $38 \cdot 10^{-4}$ DPA per $30\,\mathrm{ab^{-1}}$

In order to evaluate the energy deposition in the matching section, a two-step simulation was developed. This method has led to a reduction of the CPU time per primary by two orders of magnitude and given quantitative estimates for the matching section magnets. The source term of the second step has been characterised, in terms of particle types, energies and positions. The most abundant particles are protons and photons. The majority of the protons have an energy close to 50 TeV and will impact in the DS. The energy of the photons is lower and they are absorbed in the elements of the matching section.

The initial simulations for the matching section show that the energy deposited in the superconducting magnets was too high. Therefore, masks and collimators were included for protection measures and to reduce the energy deposition below the critical values for absorbed power and peak power density. Assuming an increase of the limit from 30 MGy to about 60 MGy to 100 MGy means that all the quadrupoles apart from Q7a are also safe in

terms of integrated dose. For Q7a other mitigation strategies like shielding in the magnet should still be implemented. Comparing the crossing schemes, no significant differences are visible.

In conclusion, a complete study of energy deposition in the entire EIR has been performed with FLUKA. Different mitigation strategies have been conceived and combined together and they have proven to be highly effective. So far no fatal problems were identified. As the next step, these studies should be extended to the DS region, downstream from the matching section.

Appendix A

Normalisation of the Simulations

The simulation results in FLUKA are not given in SI units [42][43]. For an easier understanding, they should be converted to SI units and the normalisation factors are given here. The conversion between the different units is relatively similar for all three properties, so the used relations are discussed first. To move from electronvolt to Joule the conversion is $1\,\mathrm{eV} = 1.602 \cdot 10^{-19}\,\mathrm{J}$. The cross section of an inelastic proton-proton collision σ_{pp} at $100\,\mathrm{TeV}$ centre of mass energy is assumed to be $108 \cdot 10^{-3}$ barn. In terms of luminosity the ultimate values are used, hence $30\,\mathrm{ab}^{-1}$ for the ultimate integrated luminosity and $30 \cdot 10^{34}\,\mathrm{cm}^{-2}\mathrm{s}^{-1}$ for the ultimate instantaneous luminosity [6]. Furthermore the following relationship should be remembered:

$$
\begin{aligned}
\dot{N}_{inst} &= L_{inst} \cdot \sigma_{pp} \\
&= 30 \cdot 10^{34}\,\mathrm{cm}^{-2}\mathrm{s}^{-1} \cdot 108 \cdot 10^{-27}\,\mathrm{cm}^2 \\
&= 324 \cdot 10^8\,\mathrm{s}^{-1}
\end{aligned}
\tag{A.0.1}
$$

In FLUKA simulations the results are obtained per primary (pp). In case of peak power density, $\frac{\mathrm{GeV}}{\mathrm{cm}^3}\mathrm{pp}$ has to be converted to $\frac{\mathrm{mW}}{\mathrm{cm}^3}$ by multiplying the result obtained from FLUKA by $\dot{N}_{inst}$ (see Eq. A.0.1). Using this relationship, the conversion is achieved with

$$
5184\,\frac{\mathrm{GeV}}{\mathrm{cm}^3}\mathrm{pp} = 1\,\frac{\mathrm{mW}}{\mathrm{cm}^3}.
\tag{A.0.2}
$$

For absorbed power per metre, the conversion has to lead to $\frac{\mathrm{W}}{\mathrm{m}}$. Starting again from $\frac{\mathrm{GeV}}{\mathrm{cm}^3}\mathrm{pp}$ the same steps as for peak power density are applied. Furthermore, since the denominator should change to m, one has to multiply as well with the area A in cm^2 of the element. Therefore the normalisation factor changes for every element of a different size and has to be calculated several times. Additionally a conversion from cm to m has to be applied. It can be noted as:

$$
518.4 \cdot A\frac{\mathrm{GeV}}{\mathrm{cm}^3}\mathrm{pp} = 1\,\frac{\mathrm{W}}{\mathrm{m}}.
\tag{A.0.3}
$$

The dose is given as $\frac{\mathrm{GeV}}{\mathrm{g}}\mathrm{pp}$ by FLUKA. In SI units Gray are defined as J/kg, so just a dimensionless factor has to be applied to change the FLUKA results to MGy. Since the

Appendix A Normalisation of the Simulations

integrated dose is investigated, now the ultimate integrated luminosity of $30\,\mathrm{ab}^{-1}$ is used. Similar to before, the conversion works with N:

$$
\begin{aligned}
N_{int} &= L_{int} \cdot \sigma_{pp} \\
&= 30 \cdot 10^{42}\,\mathrm{cm}^{-2} \cdot 108 \cdot 10^{-27}\,\mathrm{cm}^2 \\
&= 324 \cdot 10^{16}
\end{aligned}
\tag{A.0.4}
$$

Applying this factor on the simulation data received from FLUKA, the following conversion is obtained:

$$
518\,400\,\frac{\mathrm{GeV}}{\mathrm{g}}\mathrm{pp} = 1\,\mathrm{MGy}
\tag{A.0.5}
$$

Appendix B

List of Particle IDs in FLUKA

Particle ID	Common Name	Particle ID	Common Name
-6	Alpha	29	—
-5	Helium-3	30	—
-4	Triton	31	Antisigma-Minus
-3	Deuteron	32	Antisigma-Zero
-2	Generic HI with Z>2	33	Antisigma-Plus
-1	Optical Photon	34	Xi-Zero
0	Pseudoparticle	35	Antixi-Zero
1	Proton	36	Negative-Xi
2	Antiproton	37	Positive-Xi
3	Electron	38	Omega-Minus
4	Positron	39	Antiomega
5	Electron Neutrino	40	—
6	Electron Antineutrino	41	Positive Tau
7	Photon	42	Negative Tau
8	Neutron	43	Tau Neutrino
9	Antineutron	44	Tau Antineutrino
10	Positive Muon	45	D-Plus
11	Negative Muon	46	D-Minus
12	Kaon-zero long	47	D-Zero
13	Positive Pion	48	AntiD-Zero
14	Negative Pion	49	D_s-Plus
15	Positive Kaon	50	D_s-Minus
16	Negative Kaon	51	Lambda_c-Plus
17	Lambda	52	Xi_c-Plus
18	Antilambda	53	Xi_c-Zero
19	Kaon Zero Short	54	Xi'_c-Plus
20	Negative Sigma	55	Xi'_c-Zero
21	Positive Sigma	56	Omega_c-Zero
22	Sigma-Zero	57	Antilambda_c-Minus
23	Pion-Zero	58	AntiXi_c-Plus
24	Kaon-Zero	59	AntiXi_c-Zero
25	Antikaon-Zero	60	AntiXi'_c-Plus
26	—	61	AntiXi'_c-Zero
27	Muon Neutrino	62	AntiOmega_c-Zero
28	Muon Antineutrino		

Acronyms

ATLAS A Toroidal LHC Apparatus

CERN Conseil européen pour la recherche nucléaire

CLT Central Limit Theorem

CMS Compact Muon Solenoid

DPA Displacement Per Atom

DS Dispersion Surpressor

EIR Experimental Insertion Region

EMFCUT Electromagnetic Field Cut

FCC Future Circular Collider

FCC-ee FCC Lepton Collider

FCC-eh FCC Hadron Lepton Collider

FCC-hh FCC Hadron Collider

FEDB FLUKA Element Database

FLAIR FLUKA Advanced Interface

FLUKA Fluktuierende Kaskade

HL-LHC High Luminosity LHC

IP Interaction Point

IR Insertion Region

LEP Large Electron-Positron Collider

LHC Large Hadron Collider

LPB Leading Particle Bias

LSS Long Straight Section

NIEL Non-Ionising Energy Loss

PART-THR Particle Threshold

PDF Probability Density Function

RMS Root Mean Square

SPS Super Proton Synchrotron

Acronyms

TAN Target Absorber Neutrals

TAS Target Absorber Secondaries

TCL Target Collimator Long

Bibliography

[1] UA1 Collaboration. "Experimental observation of isolated large transverse energy electrons with associated missing energy at s=540 GeV". In: *Physics Letters B* 122.1 (1983), pp. 103 –116. DOI: `https://doi.org/10.1016/0370-2693(83)91177-2`.

[2] CMS Collaboration. "Observation of a New Boson at a Mass of 125 GeV with the CMS Experiment at the LHC". In: *Phys. Lett.* B716 (2012), pp. 30–61. DOI: `10.1016/j.physletb.2012.08.021`.

[3] ATLAS Collaboration. "Observation of a new particle in the search for the Standard Model Higgs boson with the ATLAS detector at the LHC". In: *Physics Letters B* 716.1 (2012), pp. 1 –29. DOI: `https://doi.org/10.1016/j.physletb.2012.08.020`.

[4] M. Mangano et al. *Future Circular Collider Study. Volume 1: Physics Opportunities. Conceptual Design Report.* accelerator reports CERN-ACC-2018-0056. Published in Eur. Phys. J. ST. Geneva: CERN, 2018.

[5] M. Benedikt et al. *Future Circular Collider Study.* accessed 02/12/2019. URL: `https://fcc.web.cern.ch/`.

[6] M. Benedikt et al. *Future Circular Collider Study. Volume 3: The Hadron Collider (FCC-hh) Conceptual Design Report.* accelerator reports CERN-ACC-2018-0058. Published in Eur. Phys. J. ST. Geneva: CERN, 2018.

[7] A. Dainese et al. "Heavy ions at the Future Circular Collider". In: *CERN Yellow Rep.* 3 (2017), pp. 635–692. DOI: `10.23731/CYRM-2017-003.635`. arXiv: `1605.01389` `[hep-ph]`.

[8] A. Chancé et al. "Updates on the Optics of the Future Hadron-Hadron Collider FCC-hh". In: *Proc. of International Particle Accelerator Conference (IPAC'17), Copenhagen, Denmark, 14-19 May, 2017.* (Copenhagen, Denmark). International Particle Accelerator Conference 8. Geneva, Switzerland: JACoW, 2017, pp. 2023–2026. DOI: `https://doi.org/10.18429/JACoW-IPAC2017-TUPVA002`.

[9] M. Mangano. *FCC physics reach: a brief overview.* presented at the FCC Academic Training Lectures Febr 2 2016. accessed 10/12/2019. 2016. URL: `https://indico.cern.ch/event/472105/attachments/1221263/1785721/Mangano-FCC_AT16_nobuilds.pdf`.

[10] M. Benedikt et al. *Future Circular Collider Study. Volume 2: The Lepton Collider (FCC-ee) Conceptual Design Report.* accelerator reports CERN-ACC-2018-0057. Published in Eur. Phys. J. ST. Geneva: CERN, 2018.

[11] V. Kain. "Beam Dynamics and Beam Losses - Circular Machines". In: *Proceedings of the 2014 Joint International Accelerator School: Beam Loss and Accelerator Protection.* 2014, pp. 21–39. DOI: `http://dx.doi.org/10.5170/CERN-2016-002`.

[12] H. Wiedemann. *Particle accelerator physics; 3rd ed.* Berlin: Springer, 2007. DOI: `10.1007/978-3-540-49045-6`.

Bibliography

[13]   F. Schwabl. *Statistische Mechanik.* Springer-Lehrbuch. Springer, 2000. ISBN: 9783540671589.

[14]   E. Renner. "Machine Protection of the Future Circular Hadron Collider FCC-hh: Injection and Extraction". Technical University Vienna, 2018. URL: `https://cds.cern.ch/record/2648770`.

[15]   J.R. Hunt. "Beam Quality Characterisation and the Optimisation of Next Generation Antimatter Facilities". PhD thesis. University of Liverpool, Jan. 2019.

[16]   M. Tanabashi et al. "Review of Particle Physics". In: *Phys. Rev. D* 98 (3 2018), p. 030001. DOI: `10.1103/PhysRevD.98.030001`.

[17]   N.V. Mokhov and F. Cerutti. "Beam-Material Interactions". In: *Proceedings of the 2014 Joint International Accelerator School: Beam Loss and Accelerator Protection.* 2014, pp. 83–111. DOI: `http://dx.doi.org/10.5170/CERN-2016-002`.

[18]   A. Lechner. "Particle interactions with matter". In: *CERN Yellow Reports: School Proceedings* 5.0 (2018), p. 47. DOI: `10.23730/CYRSP-2018-005.47`.

[19]   A. Ferrari. *Interaction of Particles with Matter.* accessed 10/12/2019. URL: `https://cas.web.cern.ch/sites/cas.web.cern.ch/files/lectures/v\%C3\%B6sendorf-2015/ferrari.pdf`.

[20]   *The Antiproton Decelerator.* accessed 05/12/2019. URL: `https://home.cern/science/accelerators/antiproton-decelerator`.

[21]   N. V. Mokhov et al. "Protecting LHC IP1/IP5 components against radiation resulting from colliding beam interactions". In: (2003).

[22]   R. Bruce et al. "Sources of machine-induced background in the ATLAS and CMS detectors at the CERN Large Hadron Collider". In: *Nuclear Instruments and Methods in Physics Research Section A: Accelerators, Spectrometers, Detectors and Associated Equipment* 729 (2013), pp. 825 –840. DOI: `https://doi.org/10.1016/j.nima.2013.08.058`.

[23]   F. Zimmermann et al. "Trapped macroparticles in electron storage rings". In: *Proceedings Particle Accelerator Conference.* Vol. 1. 1995, 517–519 vol.1. DOI: `10.1109/PAC.1995.504705`.

[24]   H. Vincke et al. "Induced radioactivity in and around high-energy particle accelerators". In: *Radiation Protection Dosimetry* 146.4 (June 2011), pp. 434–439. DOI: `10.1093/rpd/ncr245`.

[25]   S. Danzeca et al. "R2E". In: (2017), 199–204. 6 p. URL: `https://cds.cern.ch/record/2293533`.

[26]   O.S. Brüning et al. *LHC Design Report.* CERN Yellow Reports: Monographs. Geneva: CERN, 2004. DOI: `10.5170/CERN-2004-003-V-1`.

[27]   N.V. Mokhov. "Beam–Materials Interactions". In: *Reviews of Accelerator Science and Technology* 06 (2013), pp. 275–290. DOI: `10.1142/S1793626813300132`.

[28]   R. Flükiger. *Effects of high energy irradiation on the properties of the Nb3Sn superconducting magnets in the accelerators HiLumi LHC and FCC.* presented at the AT & T Seminar, CERN, 6.12.2018. accessed 06/12/2019. 2018. URL: `https://indico.cern.ch/event/760904/`.

[29]   R. Flükiger et al. "Impact of the Number of dpa on the Superconducting Properties in HiLumi-LHC and FCC Accelerators". In: *IEEE Transactions on Applied Superconductivity* 28.4 (2018), pp. 1–5. DOI: `10.1109/TASC.2018.2810215`.

[30] J. Frenkel. "Über die Wärmebewegung in festen und flüssigen Körpern". In: *Zeitschrift für Physik* 35.8 (1926), pp. 652–669. DOI: `10.1007/BF01379812`.

[31] G. Fasching. *Werkstoffe Für Die Elektrotechnik*. Springer Vienna, 2005. ISBN: 9783211271872.

[32] A. Fasso et al. "FLUKA Realistic Modeling of Radiation Induced Damage". In: *Progress in NUCLEAR SCIENCE and TECHNOLOGY* 2 (Oct. 2011), pp. 769–775. DOI: `10.15669/pnst.2.769`.

[33] F. Cerutti. *Beam Induced Radioactivity and Radiation Hardness*. presented at the CERN Accelerator School: Vacuum for Particle Accelerators. accessed 03/12/2019. 2017. URL: `https://indico.cern.ch/event/565314/contributions/2285844/`.

[34] C. Patrignani et al. "Review of Particle Physics". In: *Chin. Phys.* C40.10 (2016), p. 100001. DOI: `10.1088/1674-1137/40/10/100001`.

[35] H. Bethe and W. Heitler. "On the Stopping of fast particles and on the creation of positive electrons". In: *Proc. Roy. Soc. Lond.* A146 (1934), pp. 83–112. DOI: `10.1098/rspa.1934.0140`.

[36] C. Amsler et al. "Review of Particle Physics". In: *Physics Letters B* 667.1 (2008). Review of Particle Physics, pp. 1 –6. ISSN: 0370-2693. DOI: `https://doi.org/10.1016/j.physletb.2008.07.018`.

[37] U. Amaldi and G. Kraft. "Radiotherapy with beams of carbon ions". In: *Reports on Progress in Physics* 68.8 (2005), pp. 1861–1882. DOI: `10.1088/0034-4885/68/8/r04`.

[38] N. Metropolis and S. Ulam. "The Monte Carlo Method". In: *Journal of the American Statistical Association* 44.247 (1949), pp. 335–341. ISSN: 01621459.

[39] N. Metropolis. "The Beginning of the Monte Carlo Method". In: *Los Alamos science. Special Issue dedicated to Stanislaw Ulam.* 1987, pp. 125–130.

[40] M.C. Cantone and C. Hoeschen. *Radiation Physics for Nuclear Medicine*. Springer Berlin Heidelberg, 2011. ISBN: 9783642113277.

[41] W.L. Dunn and J.K. Shultis. *Exploring Monte Carlo Methods*. Elsevier Science & Technology, 2011. ISBN: 9780444558640.

[42] T.T. Böhlen et al. *The FLUKA Code: Developments and Challenges for High Energy and Medical Applications*. Nuclear Data Sheets 120 211-214. Published in Eur. Phys. J. ST. CERN, 2014.

[43] A. Ferrari et al. *FLUKA: a multi-particle transport code*. Tech. rep. CERN-2005-10 (2005), INFN/TC_05/11, SLAC-R-773. Published in Eur. Phys. J. ST. 2014.

[44] S. Agostinelli et al. "Geant4—a simulation toolkit". In: *Nuclear Instruments and Methods in Physics Research Section A: Accelerators, Spectrometers, Detectors and Associated Equipment* 506.3 (2003), pp. 250 –303. DOI: `https://doi.org/10.1016/S0168-9002(03)01368-8`.

[45] C.J. Werner et al. *MCNP6.2 Release Notes*. Tech. rep. LA-UR-18-20808. Los Alamos National Laboratory. 2018.

[46] S. Roesler, R. Engel, and J. Ranft. "The Monte Carlo Event Generator DPMJET-III". In: *Advanced Monte Carlo for Radiation Physics, Particle Transport Simulation and Applications* (2001), 1033–1038. DOI: `10.1007/978-3-642-18211-2_166`.

[47] *FLUKA: Combinatorial Geometry*. presented at the 7th FLUKA Course, NEA Paris. accessed 05/12/2019. 2008. URL: `http://www.fluka.org/content/course/NEA/lectures/Geometry.pdf`.

[48] V. Vlachoudis et al. *FLUKA Advanced Interface*. accessed 20/08/2019. URL: `http://www.fluka.org/flair/`.

[49] A. Mereghetti and L. S. Esposito. *The Fluka Line Builder*. accessed 20/08/2019. URL: `https://twiki.cern.ch/twiki/bin/view/FlukaTeam/FlukaLineBuilder`.

[50] CERN BE/ABP Accelerator Beam Physics Group. *MAD - Methodical Accelerator Design*. accessed 02/12/2019. URL: `http://http://mad.web.cern.ch/mad/`.

[51] A. Ferrari et al. *FLUKA Manual*. accessed 10/12/2019. URL: `http://www.fluka.org/content/manuals/online/INDEX-fluka2011.html`.

[52] G. Apollinari et al. *High-Luminosity Large Hadron Collider (HL-LHC): Technical Design Report V. 0.1*. CERN Yellow Reports: Monographs. Geneva: CERN, 2017. DOI: `10.23731/CYRM-2017-004`. URL: `https://cds.cern.ch/record/2284929`.

[53] A. Infantino et al. *Energy deposition from collision debris in FCC-hhEIR*. presented at the EuroCircol 2018 Meeting, Karlsruhe. accessed 20/08/2019. URL: `https://indico.cern.ch/event/733292/contributions/3147544`.

[54] R. Martin. "Interaction Region Design for a 100 TeV Proton-Proton Collider". Presented 23 Nov 2017. 2017. URL: `https://cds.cern.ch/record/2648627`.

[55] B. Humann. *Energy Deposition Studies in FLUKA*. Tech. rep. Projektarbeit. CERN/TU Vienna, 2019.

[56] M. I. Besana et al. "Evaluation of the radiation field in the future circular collider detector". In: *Phys. Rev. Accel. Beams* 19.11 (2016), p. 111004. DOI: `10.1103/PhysRevAccelBeams.19.111004`.

[57] M.I. Besana et al. "Assessment and Mitigation of the Proton-Proton Collision Debris Impact on the FCC Triplet". In: *Proc. of International Particle Accelerator Conference (IPAC'16), Busan, Korea, May 8-13, 2016*. (Busan, Korea). International Particle Accelerator Conference 7. Geneva, Switzerland: JACoW, 2016, pp. 1410–1413. DOI: `doi:10.18429/JACoW-IPAC2016-TUPMW004`.

[58] C. Kotnig et al. *Development of a Cryogenic System for the FCC-hh Inner Triplets Cold Mass Cooling*. presented at the FCC Week 2019. accessed 04/12/2019. 2019. URL: `https://indico.cern.ch/event/727555/contributions/3427601/`.

[59] D. Tommasini. *Radiation limits of normal- and superconducting magnets*. presented at the FCC other Magnet Design Meeting #1. accessed 05/12/2019. 2017. URL: `https://indico.cern.ch/event/647002/contributions/2628503/`.

[60] M.I. Besana et al. *Overview and status of the radiation load studies focused on magnets*. presented at the 2nd FCC-hh Magnet-Beam Dynamics Coordination Meeting. accessed 03/12/2019. 2017. URL: `https://indico.cern.ch/event/629956/contributions/2571804/`.

[61] M.I. Besana. private communication, October. 2019.

[62] S. Fartoukh et al. *LHC triplet lifetime versus operational scenario in ATLAS and CMS*. presented at the 225th LHC Machine Committee. accessed 02/12/2019. 2015. URL: `{https://indico.cern.ch/event/406858/contributions/966580/}`.

[63]   R. Martin et al. "Interaction region design driven by energy deposition". In: *Phys. Rev. Accel. Beams* 20.8 (2017), p. 081005. DOI: 10.1103/PhysRevAccelBeams.20.081005.

[64]   R. Martin. *Optics*. presented at the FCC Week 2019. accessed 04/12/2019. 2019. URL: https://indico.cern.ch/event/727555/contributions/3452769/.

[65]   J. Barranco García et al. "Beam-Beam Studies for FCC-hh". In: *Proc. of International Particle Accelerator Conference (IPAC'17), Copenhagen, Denmark, 14-19 May, 2017*. (Copenhagen, Denmark). International Particle Accelerator Conference 8. Geneva, Switzerland: JACoW, 2017, pp. 2109–2112. DOI: https://doi.org/10.18429/JACoW-IPAC2017-TUPVA026.

[66]   T. Pieloni et al. *Beam-Beam Studies for FCC-hh*. presented at FCC Week 2017. accessed 02/12/2019. 2017. URL: https://indico.cern.ch/event/556692/contributions/2484262/.

[67]   M.I. Besana. private communication, January. 2019.

[68]   F. Cerutti. private communication, June. 2019.

List of Figures

LIST OF FIGURES

List of Tables